JAMES | Journal of Advances in Modeling Earth Systems®

RESEARCH ARTICLE
10.1029/2025MS005394

An Energetically and Observationally Constrained Mesoscale Parameterization for Ocean Climate Models

Romain Torres[1], Robin Waldman[1], Gurvan Madec[2], Casimir de Lavergne[2], Roland Séférian[1], and Julian Mak[3,4]

[1]CNRM, UMR 3589, Météo-France, CNRS, Université de Toulouse, Toulouse, France, [2]LOCEAN Laboratory, Sorbonne Université/CNRS/IRD/MNHN, Paris, France, [3]Department of Ocean Science, Hong Kong University of Science and Technology, Hong Kong, Hong Kong, [4]National Oceanography Centre, Southampton, UK

Key Points:

- An energy-based parameterization for mesoscale transports in ocean models is presented and calibrated against eddy kinetic energy (EKE) observations
- A realistic subgrid EKE distribution constrains both the Gent-McWilliams coefficient and the neutral tracer diffusivity
- In hindcast simulations, energy constraints accelerate the Southern Ocean and North Atlantic circulations while cooling the ocean interior

Correspondence to:

R. Torres,
romain.torres@meteo.fr

Citation:

Torres, R., Waldman, R., Madec, G., de Lavergne, C., Séférian, R., & Mak, J. (2025). An energetically and observationally constrained mesoscale parameterization for ocean climate models. *Journal of Advances in Modeling Earth Systems*, *17*, e2025MS005394. https://doi.org/10.1029/2025MS005394

Received 30 JUL 2025
Accepted 13 NOV 2025

Abstract An extension of the GEOMETRIC parameterization (Mak, Marshall, et al., 2022, https://doi.org/10.1029/2022ms003223) for the mesoscale eddy transport is proposed and tested in a one-degree resolution global ocean model. It consists in solving a prognostic two-dimensional equation for the eddy kinetic energy (EKE). The parameterized EKE budget is calibrated from an observation-based estimate of the EKE reservoir, allowing an unprecedented realism of the subgrid EKE field within a global eddy-parameterizing ocean configuration. The predicted EKE map is then used to specify temporal and spatial variability of both the Gent-McWilliams coefficient (κ_{gm}) and the neutral diffusivity of tracers (κ_n), which display strong horizontal variations and a general decrease in polar regions. Using a suite of hindcast ocean simulations, we assess the respective effects of the novel distributions of κ_{gm} and κ_n. Changes in κ_{gm} impact strongly the simulated global ocean circulation: they increase the eastward volume transport through Drake Passage by 21 Sv (10^6 m^3 s^{-1}), and the Atlantic Meridional Overturning Circulation strength at 26°N by 2.6 Sv, reducing biases. Changes in κ_n can substantially modify the transfer of surface water properties into the ocean interior: we find a strong influence on sea surface temperatures and ocean heat storage. The results highlight the need to physically constrain mesoscale transport in ocean climate models. By linking the two eddy coefficients to the same subgrid EKE, itself constrained from indirect observations of EKE, our developments represent a significant advancement toward unified and energy-consistent mesoscale parameterizations.

Plain Language Summary Ocean mesoscale eddies are large vortices with horizontal scales ranging from 10 to 100 km, which are ubiquitous in the World Ocean. They are capable of efficiently transporting water masses, thereby influencing the distribution of properties such as heat, salt, carbon, and nutrients across the ocean. In order to predict the evolution of these properties, numerical models of the ocean are run on high-performance computers. However, because of limited computing resources, the simulation of ocean currents often misses mesoscale eddies. Consequently, many global ocean models mimic the effect of mesoscale eddies by employing approximate mathematical formulations, called "parameterizations." Two effects are typically parameterized: mass transport and mixing of water properties along surfaces of constant density. In this study, we propose to represent these effects via an estimation of the kinetic energy of mesoscale eddies within the ocean model, which we validate against observations. Using several model simulations, we then disentangle the impacts of the two effects on global ocean circulation and heat content. Given the potential of both mechanisms to influence property distributions and major circulation features, our developments mark a step forward in the consistent representation of mesoscale transports within ocean climate models.

1. Introduction

Mesoscale eddies are energetic dynamical structures that efficiently transport heat, salt, and biogeochemical substances in the ocean. Despite their relatively small diameter, typically between 10 to a few hundreds of kilometers, mesoscale eddies contain most of the ocean kinetic energy (Ferrari & Wunsch, 2009). They are crucial for the climate system, influencing both the ocean mean state (Abernathey et al., 2022; Melet et al., 2022) and its variability (Busecke & Abernathey, 2019). The effects of mesoscale ocean eddies must therefore be correctly represented in conceptual and numerical models of the Earth system. Due to their relatively coarse grids, current ocean models used for climate simulations do not often explicitly resolve the mesoscale, but instead utilize some parameterizations to account for their effects (Hewitt et al., 2020). Two separate effects are commonly represented. First, stirring along density surfaces is usually parameterized with down-gradient diffusion of tracers

rotated in the local neutral (i.e., isopycnal) direction (Redi, 1982). Second, eddy-induced mass transports are parameterized as down-gradient diffusion of isopycnal layer thickness (Gent and McWilliams (1990), hereafter GM), expressed as an extra advection of tracers. The mean effect of the GM scheme is to flatten the isopycnal slopes, thereby extracting available potential energy (APE) from the large-scale ocean stratification as expected from baroclinic instabilities (Gent et al., 1995).

However, coarse ocean models employing such parameterizations are often sensitive to the choice of the eddy diffusivities (Fox-Kemper et al., 2019). Consequently, specification of these coefficients has become an important area of research. Regarding the eddy-driven circulation governed by the GM coefficient (κ_{gm}), models typically employ a time- and space-variable eddy coefficient computed from the large-scale density field (Bryan et al., 1999; Treguier et al., 1997; Visbeck et al., 1997). Such formulations are derived from linear instability analysis and scale the GM coefficient as the growth rate of an Eady wave (Eady, 1949) times a squared eddy length scale. It is noteworthy that some models also define κ_{gm} with the local squared buoyancy frequency (Danabasoglu & Marshall, 2007; Ferreira et al., 2005), thereby allowing for three-dimensional variations. On the other hand, the neutral diffusivity (κ_n) driving the isopycnal tracer mixing in ocean models is often assumed to be constant or spatially decreasing from the equator to higher latitudes, following the grid cell size, without being physically constrained (Holmes et al., 2022). In order to improve upon this approach and provide horizontal structures for neutral diffusion, some ocean models set $\kappa_n = \kappa_{gm}$. However, theoretical work has shown that the two diffusivities should differ (Smith & Marshall, 2009). These ad hoc representations are problematic given the documented impacts of neutral diffusivity on the simulated climate (Chouksey et al., 2022; Hieronymus & Nycander, 2013; Pradal & Gnanadesikan, 2014) and marine biogeochemical cycles (Gnanadesikan et al., 2015; Lévy et al., 2024). For further examples on the specification of mesoscale parameterizations, the reader is referred to Appendix A, which details the mesoscale parameterizations employed within the Ocean Model Intercomparison Project 2 (OMIP2; Tsujino et al., 2020) exercise.

Another issue arises from the fact that the specifications of κ_{gm} and κ_n are poorly constrained by theories and observations, preventing the establishment of a clear relationship between the two despite shared physics. This inconsistency results in a large degree of freedom and uncertainty between ocean and climate models. Theories and diagnostics based on linear stability analysis have been able to relate different eddy diffusivities within the quasi-geostrophic framework (Smith & Marshall, 2009), enabling the construction of global maps of mesoscale diffusivities from observational hydrographic climatology (Kusters et al., 2025; Vollmer & Eden, 2013). However, to date, no practical relationship has been derived between the eddy-induced advection and the isopycnal mixing to be implemented in ocean models. As the GM scheme is directly linked to an energy conversion flux, several parameterizations have been proposed to relate κ_{gm} to the eddy energy (Cessi, 2008; Eden & Greatbatch, 2008; Jansen, Adcroft, et al., 2015; Jansen et al., 2019; Mak et al., 2018; D. P. Marshall et al., 2012; Mak, Marshall, et al., 2022). Those parameterizations often involve solving a prognostic equation for the subgrid eddy energy. Recently, Groeskamp et al. (2020) have combined mixing length and suppression theories to construct a three-dimensional map of κ_n from observations of temperature, salinity and sea surface height. In their estimation, the neutral diffusivity is related to the EKE and the ocean stratification. To our knowledge, only Holmes et al. (2022) have tested this parameterization of κ_n in a coarse resolution ocean model. Their study used the static map of Groeskamp et al. (2020), and thus did not allow feedbacks nor spatial consistency between the simulated circulation and the parameterized isopycnal mixing. Our aim is to build upon their approach to specify an interactive and self-consistent map of κ_n within our ocean model.

In this study, we use existing energy-based formulations of the eddy coefficients to relate both eddy coefficients and propose a unified, energy-constrained mesoscale eddy transport parameterization to be used in climate models. Within the new parameterization, the two eddy coefficients (κ_n and κ_{gm}) are functions of the same EKE field. The subgrid energy field is determined by a prognostic two-dimensional eddy energy budget, similar to the one employed in the GEOMETRIC parameterization (Mak et al., 2018; Mak, Marshall, et al., 2022). However, our parameterization differs from that of GEOMETRIC in that we use the EKE instead of the total eddy energy, leading to different modeling choices. Another key element of this work is that the prognostic eddy energy budget has been empirically calibrated using a global configuration with realistic bathymetry and atmospheric forcing. This yields close alignment with an observation-based estimate of the EKE reservoir, thereby constraining the parameterized mesoscale transport from indirect observations.

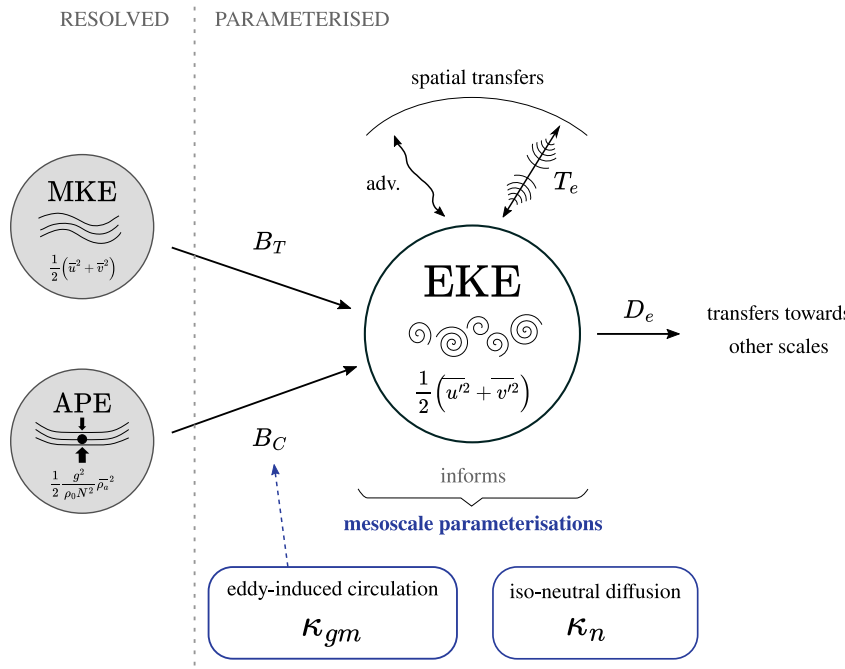

Figure 1. Summary of energy transfers parameterized in the prognostic eddy kinetic energy (EKE) equation. Terms of the budget are represented by black arrows. Sources from different instabilities are computed from the resolved mechanical energy reservoirs while spatial transfers are processes which redistribute the energy across the ocean. Sinks D_e represent all the mechanisms able to remove EKE. The resulting parameterized reservoir is then used to constrain existing mesoscale parameterizations (in blue). The blue dotted line shows direct feedback between the parameterized EKE and κ_{gm}, which modulates the baroclinic energy flux. In the available potential energy definition, ρ_a refers to the density anomalies from a reference state.

The document is organized as follows. Section 2 describes the proposed mesoscale parameterization and provides a description of the ocean general circulation model used for the implementation. Numerical experiments conducted to calibrate the eddy energy budget and to assess the effects of the novel parameterization on the ocean state are also introduced. In Section 3, we analyze a set of four hindcast simulations to assess the scheme's performance in predicting the EKE in the World Ocean and to evaluate the impact on the specified eddy diffusivities. In Section 4, we explore the sensitivity of some large-scale ocean circulation metrics to the new coefficient specifications in the same hindcast simulations. Section 5 summarizes the results and discusses some prospects of this work.

2. Methods

2.1. Constraining Mesoscale Transport Parameterizations

2.1.1. The Parameterized Eddy Kinetic Energy Budget

In this study, we introduce a new parameterized budget for the depth-integrated EKE. It consists in an extra two-dimensional prognostic equation representing the physical and dynamical processes able to add, remove or transport EKE across the ocean. The GEOMETRIC parameterization (Mak et al., 2018; Mak, Marshall, et al., 2022) has been adapted by replacing the total (potential plus kinetic) eddy energy (E) with the EKE. Furthermore, the application is generalized to neutral diffusivity in order to predict both κ_{gm} and κ_n. The parameterization and associated energy transfers are synthesized in Figure 1.

In GEOMETRIC, the implementation of a two-dimensional prognostic equation for the depth-integrated total eddy energy E is preferred mostly for practical reasons. Specifically, this avoids division by zero in the formulation of κ_{gm} (see Equation 6) at depths where isopycnals are flat. In this work, we have decided to maintain the aforementioned two-dimensional approach (but our prognostic variable is the EKE) since it offers the advantages of simplicity and cost-effectiveness. Our parameterized budget is then obtained from vertically

integrating the three-dimensional EKE equation and using modeling closures to express each term of the resulting budget as a function of resolved quantities (see Appendix B for details about the complete derivation and the different assumptions):

$$\frac{\partial}{\partial t}\int \mathrm{EKE}\, dz + \int \nabla_h \cdot (\mathbf{u}_h\, \mathrm{EKE})\, dz = B_C + B_T - D_e + T_e, \tag{1}$$

where the left-hand side represents the total change (time rate plus integrated transport by the resolved horizontal velocity $\mathbf{u}_h$) of the depth-integrated EKE. The right-hand side includes baroclinic (B_C) and barotropic (B_T) production, as well as dissipation (D_e) and subgrid-scale transport (T_e).

On the right-hand side of Equation 1, terms representing EKE trends are:

- The baroclinic energy conversion B_C between APE and EKE. Traditionally, this baroclinic energy pathway is decomposed into two distinct energy fluxes: an energy conversion between APE and eddy potential energy (EPE) and the conversion between EPE and EKE. At the global scale, these terms have been shown to be very similar in the ocean (von Storch et al., 2012) and the atmosphere (L. Li et al., 2007; Lorenz, 1955; Ma et al., 2021). We assume equality between the two and use a parameterization of the APE to EPE flux for the baroclinic energy sources (see Appendix B):

$$B_C = \int \kappa_{gm} \frac{M^4}{N^2}\, dz, \tag{2}$$

  where $M^2 = (g/\rho_0)|\nabla_h \rho|$ and $N^2 = -(g/\rho_0)\partial_z \rho$ are the horizontal and vertical buoyancy stratification, respectively, g the gravitational acceleration, ρ the in situ density of seawater and ρ_0 a reference density. Following the implementation in Mak, Marshall, et al. (2022), the ratio M^4/N^2 is calculated from the isoneutral slopes $s = M^2/N^2$, already computed by the model (described in Section 2.2) at each time step. Note that slopes are bounded by a maximum value of 1/100 and are gradually reduced to zero at the surface within the mixed layer. As B_C is related to the eddy buoyancy fluxes, the diffusivity is taken to be the Gent-McWilliams coefficient κ_{gm} (Mak et al., 2018; D. P. Marshall et al., 2012).
- The barotropic energy conversion B_T between mean kinetic energy (MKE) and EKE. It represents energy exchange due to interactions between mesoscale eddies and the mean flow. It is parameterized following a flux-gradient closure relation as:

$$B_T = \int \kappa_u |\nabla_h \mathbf{u}_h|^2 dz, \tag{3}$$

  where $\kappa_u = 1{,}500\ \mathrm{m^2\ s^{-1}}$ is an eddy diffusivity for the horizontal momentum. Since κ_u is positive here, the term B_T is only a source in the EKE budget. While this is true at the global scale, studies have shown it may be either positive or negative locally (von Storch et al., 2012; Tedesco et al., 2019). Based on quasi-geostrophic potential vorticity mixing argument, Eden and Greatbatch (2008) used a more complete formulation for the momentum shear production term (their Equation 22) but at the cost of introducing more eddy coefficients. It should be noted here that subsequent modeling work has used a negative Laplacian viscosity to parameterize the kinetic energy transfer toward the resolved reservoir (Bachman, 2019; Jansen & Held, 2014; Jansen, Held, et al., 2015). This method, known as kinetic energy backscatter, has been shown to be instrumental in raising energy levels in eddy-permitting ocean models (Juricke et al., 2020). However, as our study focuses on coarser-resolution (eddy-parameterizing) models, backscatter has not been included. Recently, Grooms et al. (2025) have implemented stochastic velocity increments in a coarse ocean model, which represent the divergence of stresses due to subgrid mesoscale currents. A potential future improvement could be to connect their stochastic forcing term in the horizontal momentum equations to our EKE budget through B_T.
- The dissipation rate D_e of depth-integrated EKE. While many processes are able to remove EKE, via down-scale or up-scale energy transfers, D_e represents here the total energy flux flowing out of the mesoscale reservoir. It is parameterized from dimensional arguments as expressed by Kolmogorov (1941b) for three-dimensional turbulence:

$$D_e = \frac{C_\varepsilon}{R_d} \int \mathrm{EKE}^{3/2}\, dz, \tag{4}$$

where $C_\varepsilon = 0.022$ is a dimensionless dissipation coefficient and R_d the local Rossby radius of deformation. This term is set to zero if the EKE becomes negative, ensuring that this situation does not persist and that the eddy energy field remains positive.

This closure is based on the inertial range theory of three-dimensional turbulence (Kolmogorov, 1941b), which assumes the existence of a range of scales separating the large forcing scale and the small dissipation scale. In order for the kinetic energy spectrum to achieve a steady state, the rate of energy input at the forcing scale must be equal to the energy flux cascading to smaller scales through the inertial range. This energy flux is also equal to the dissipation rate ϵ, which is entirely determined from the energy-containing range (Kolmogorov, 1941a). Equation 4 arises from dimensional analysis and is the only combination of velocity and length scales that yields the dimension of an energy flux. This theory provides a prediction for the kinetic energy spectra, which is proportional to $\epsilon^{2/3}k^{-5/3}$, where k is the wavenumber.

In two-dimensional (quasi-geostrophic) turbulence, kinetic energy is thought to be transferred primarily upscale, from the forcing scale to larger scales (Fjørtoft, 1953), rather than downscale. Observational studies (Steinberg et al., 2022) and global ocean simulations (Sérazin et al., 2018) indeed point to the inverse cascade as a major kinetic energy flux at the mesoscale. However, the dimensional argument used to derive Equation 4 can still be applied provided the inertial range exists. Existence of this energy inertial range is supported by idealized simulations of two-dimensional and incompressible flows (Maltrud & Vallis, 1991). As the energy is injected at scales close to the Rossby radius of deformation before cascading toward larger scales, the characteristic length is proportional to R_d in our EKE budget. Note that the formulation of Equation 4 differs from the linear dissipation term of GEOMETRIC. As the linear relationship between dissipation and depth-integrated eddy energy seems essential for achieving zonal transport independent of wind stress (Maddison et al., 2025; D. P. Marshall et al., 2017), it is uncertain whether the proposed parameterization will retain the eddy saturation property as documented by Mak et al. (2017).

- The small-scale horizontal EKE transport T_e redistributing the energy spatially. It includes the effect of the eddy pressure work as well as the transport due to eddy velocities. Assuming the latter is of leading order and using a flux-gradient relation leads to an isotropic eddy diffusion of the EKE:

$$T_e = \kappa_E \int \left(\nabla_h^2 \cdot \mathrm{EKE}\right) dz, \tag{5}$$

where κ_E is the EKE eddy diffusion coefficient set to 500 $\mathrm{m}^2\ \mathrm{s}^{-1}$ following Mak et al. (2018).

It is important to note that Equation 1 is a prognostic equation for the depth-integrated energy $\int \mathrm{EKE}\, dz$. However, the equation requires the computation of vertical integrals containing the three-dimensional EKE, for dissipation and transport terms. The three-dimensional EKE is given using a structure function $\phi(z)$, which assumes separability of horizontal and vertical dimensions of the mesoscale eddy velocities, such that $(u', v')(z) = \phi(z)(u'_0, v'_0)$, with u', v' the eddy velocities and subscript 0 representing the surface variables.

The surface EKE_0 is computed beforehand using the vertical structure function which leads to $\mathrm{EKE}_0 = \int \mathrm{EKE}\, dz / \iint \phi(z)^2\, dz$. The structure function $\phi(z)$ can be either set to unity in which case the energy is uniformly distributed in the vertical, or read from a static three-dimensional map. In the latter case, we used the surface modes (de La Lama et al., 2016; LaCasce, 2017) computed following the method of Groeskamp et al. (2020) applied to the World Ocean Atlas 2018 hydrographic climatology (Garcia et al., 2019). This approach leads to some inconsistency between the climatology used to compute $\phi(z)$ and the model world. However it represents a first step before the implementation of an interactive computation of $\phi(z)$ within the general circulation model.

Our prognostic EKE budget of Equation 1 has been implemented in the Nucleus for European Modeling of the Ocean (NEMO) version 3.6 (Madec et al., 2017). The developments build upon the implementation of GEOMETRIC in NEMO already described in Mak, Marshall, et al. (2022). New developments from this work are detailed in Appendix D.

2.1.2. Specification of Eddy Coefficients

The Gent-McWilliams coefficient used to compute the eddy-induced velocities is defined following the formulation of D. P. Marshall et al. (2012). They proposed a scaling for κ_{gm} where the coefficient is proportional to the total (potential plus kinetic) eddy energy (E). Here, their framework is adapted by using the EKE only. Furthermore, we employ a two-dimensional approach (Mak et al., 2018) to avoid division by zero at depths where isopycnals are flat:

$$\kappa_{gm} = \alpha \frac{\int \mathrm{EKE}\, dz}{\int M^2/N\, dz}, \tag{6}$$

where $\alpha = 0.04$ and $\int M^2/N\, dz$ is lower-bounded to 10^{-10}. The non-dimensional constant α represents the eddy efficiency to convert mean APE into mesoscale kinetic energy. Since Equation 6 substitutes E with the EKE, the parameter α differs from the one introduced by D. P. Marshall et al. (2012) and, in particular, is no longer bounded by unity. However, Bachman et al. (2017) have tested this scaling using the three types of energy (E, EKE, or EPE) and found little difference in the domain-averaged GM coefficient when changing the type of energy (see their Figure 5), aside from the need to re-scale the value of α. Although their analysis has not been conducted in more realistic configurations, it suggests that uncertainties in Equation 6 lie primarily in the value chosen for the efficiency coefficient α.

Based on mixing length theory (Prandtl, 1925), the neutral tracer diffusivity is related to an eddy length scale and a velocity scale (taken as the square root of EKE):

$$\kappa_n(z) = \Gamma L_{\mathrm{mix}}\, \phi(z)\sqrt{2\mathrm{EKE}_0}, \tag{7}$$

where the non-dimensional parameter Γ is an eddy mixing efficiency, L_{mix} the eddy length scale associated to mixing processes and $\phi(z)\sqrt{2\mathrm{EKE}_0}$ represents the eddy velocity scale. Following Groeskamp et al. (2020), the mixing efficiency parameter is set to $\Gamma = 0.35$ while the mixing length L_{mix} is defined as the local Rossby radius R_d but capped at 40 km to avoid singularity and large values near the equator. As a result of the structure function $\phi(z)$ in Equation 7, the neutral diffusivity can either be constant or vary in the vertical. Finally, no suppression of mesoscale mixing by mean flows (Ferrari & Nikurashin, 2010; Klocker et al., 2012) or topography (Naveira Garabato et al., 2011) has been implemented here; such suppression effects could constitute a future extension of this parameterization.

2.2. The Ocean-Sea Ice Model

In this study, we use the ocean and sea-ice components of the CNRM-CM6-1 climate model (Voldoire et al., 2019) employed for the generation of the Ocean Model Intercomparison Project 2 (OMIP2; Tsujino et al., 2020) outputs (Voldoire, 2020) within Phase 6 of the Coupled Model Intercomparison Project (CMIP6, Eyring et al., 2016). The codebase is NEMO version 3.6 (Madec et al., 2017) for ocean physics and GELATO (Global Experimental Leads and sea ice for Atmosphere and Ocean) version 6 for sea ice physics (Salas Mélia, 2002). The model approximates the ocean circulation using primitive equations, namely the Reynolds-Averaged Navier-Stokes equations on a rotating sphere under the hydrostatic and Boussinesq hypotheses. Furthermore, the TEOS-10 equation of state is used with the polynomial approximation from Roquet et al. (2015).

The model employs the eORCA1 grid defined from the tripolar curvilinear ORCA system, with a nominal horizontal resolution of 1° and a refinement of latitudinal resolution to 1/3° in the tropics. This horizontal resolution is insufficient for explicitly resolving mesoscale eddies (Hallberg, 2013), which are therefore parameterized. In CNRM-CM6-1, the lateral viscosity is parameterized by a horizontal Laplacian operator as described for the NOCS-ORCA1 configuration in Danabasoglu et al. (2014). The eddy viscosity coefficient, unmodified in this study, is set to 20,000 $\mathrm{m^2\ s^{-1}}$, except for a reduction to 1,000 $\mathrm{m^2\ s^{-1}}$ confined to equatorial upper ocean waters away from western boundaries.

In the following, the global ocean and sea-ice model is first used to calibrate our EKE budget. We then set up a suite of simulations to assess the impact of modifying κ_n and κ_{gm} according to the proposed energy constraints.

2.3. Numerical Experiments

2.3.1. Calibrating the Eddy Kinetic Energy Budget

Because both κ_n and κ_{gm} depend on EKE, and because the surface EKE is a relatively well observed quantity, we have decided to focus the calibration on parameters of the EKE budget (Equation 1). The EKE budget includes four parameters: the eddy momentum diffusivity κ_u, the dissipation coefficient C_ϵ, the eddy diffusion coefficient κ_E and the eddy baroclinic efficiency α in the formulation of κ_{gm}.

The objective of our calibration is to obtain a subgrid depth-integrated EKE that best matches the observational estimate of Torres et al. (2023). The sensitivity of the parameterized EKE to the four parameters is assessed by running the global ocean and sea-ice model for 15 years, from 1958 to 1973. The model is forced at the surface with the Japanese 55-year atmospheric reanalysis for driving ocean models (JRA55-do v1.5.0; Tsujino et al., 2018). The choice of using a short period of 15 years is justified because the simulated EKE reservoir equilibrates within a few years (see Figure E1). The period considered should not affect the calibration results. We test a total of 80 different sets of parameters, which sample plausible parameter ranges documented in the literature (see Table E1). The chosen set of parameters is the one that best reproduces both the global EKE reservoir and its spatial distribution. We explore the parameter space in an empirical rather than systematic fashion such that our calibration does not ensure that the optimal fit with the observational estimate is obtained. However, this methodology allowed us to highlight the most important parameters and to achieve an accurate EKE prediction (see Section 3).

Within this calibration exercise, we performed 15-year simulations to compare our dissipation term D_e, based on dimensional analysis arguments, with the linear damping formulation employed in GEOMETRIC (Mak, Marshall, et al., 2022). Although both formulations can be tuned to obtain the right amount of domain-integrated eddy energy, we find that the choice of formulation strongly impacts on the spatial distribution of EKE. Stronger spatial correlation to the observation-based reference is obtained when using the non-linear dissipation term of Equation 4 (see Figure E6). In particular, this term generates larger depth-integrated EKE in subtropical gyres, aligning more closely with the observation-based estimate. Furthermore, the 1.5 power law in the dissipation term results in a smoother eddy energy field along strong western boundary currents (WBCs) and the Antarctic Circumpolar Current (ACC), also improving agreement with our reference.

2.3.2. Hindcast Simulations With an OMIP-Like Protocol

Table 1 summarizes the experiments carried out to study the impacts of our parameterization. It also indicates characteristic values of the eddy coefficients κ_{gm} and κ_n in each experiment. In total, four long global ocean simulations are performed. Their design is now described in detail.

Our DEFAULT simulation follows the choices made for the ocean and sea-ice model components of CNRM-CM6-1 (Voldoire et al., 2019). The neutral diffusivity κ_n is equal to 1,000 $m^2\ s^{-1}$ at the equator and varies with latitude only, in proportion to the zonal length of grid cells (see Figure 5). κ_{gm} is independent of depth, but varies horizontally and over time in response to the simulated ocean density field. It is calculated by multiplying the squared local Rossby radius R_d and a timescale interpreted as the Eady growth rate. The latter is calculated using equation 50 of Treguier et al. (1997). Note that the coefficient is limited by a maximum value of 1,000 $m^2\ s^{-1}$.

The DEFAULT configuration is then compared to three other experiments, all including the parameterized EKE budget. The EKE-GM configuration redefines κ_{gm} using Equation 6 while keeping the neutral diffusivity unchanged. In comparison to DEFAULT, κ_{gm} is overall reduced, with a global mean of 345 $m^2\ s^{-1}$ (vs. 386 $m^2\ s^{-1}$). However, the upper bound value of 1,000 $m^2\ s^{-1}$ set in DEFAULT is relaxed allowing κ_{gm} to grow up to 12,700 $m^2\ s^{-1}$ locally. This increases the eddy coefficient in regions of high EKE, for example, in the core of WBCs.

The third configuration, EKE-GM+N specifies both κ_{gm} and κ_n using the prognostic EKE. In contrast to κ_{gm}, the use of the novel specification of κ_n (Equation 7) increases the global mean value of the neutral diffusivity, which is 1,466 $m^2\ s^{-1}$ in EKE-GM+N, twice as large as in DEFAULT and EKE-GM. Since the equilibrated EKE is similar to the one obtained in the experiment EKE-GM, values for κ_{gm} remain almost unchanged. Note that EKE-GM and EKE-GM+N share the same values for the parameters involved in our EKE budget.

Table 1
Specifications of the Different OMIP2 Experiments

	Specification of κ_{gm}				Specification of κ_n			
Experiments	Type	min-max	Vol. mean	$\phi(z)$	Type	min-max	Vol. mean	$\phi(z)$
DEFAULT	Growth	0–1,000	386	No	Grid	214–1,000	833	No
EKE-GM	EKE	10–12,716	345	No	Grid	214–1,000	833	No
EKE-GM+N	EKE	10–12,522	345	No	EKE	10–5,291	1,466	No
EKE-GM+N3D	EKE	10–12,522	310	No	EKE	10–10,604	944	Yes

Note. The eddy coefficients are given in units of $m^2\ s^{-1}$. They can follow a formulation based on the Eady growth rate (Growth) as proposed by Treguier et al. (1997), or can be proportional to the grid cell size (Grid) as described in Madec et al. (2017), or can be energetically constrained (EKE) with Equations 6 and 7 as in this study. The range (min-max) as well as the volume mean of both coefficients are computed from the time-averaged variables over 1995–2017 of the last forcing cycle. In all experiments, the structure function $\phi(z)$ is set to unity except in EKE-GM+N3D which uses surface modes computed by Torres et al. (2023) for the specification of κ_n. Note that $\phi(z)$ is used not only in Equation 7 but also in the energy budget (Equation 1); the equilibrated depth-integrated EKE is thus modified by the structure function, and so is κ_{gm} via Equation 6.

Finally, the EKE-GM+N3D experiment is employed to assess the influence of the structure function $\phi(z)$ in both the definition of κ_n (Equation 7) and the EKE budget (Equation 1). To do so, the structure function is set to surface modes (de La Lama et al., 2016; LaCasce, 2017) applied to a global observational climatology of density as computed in the study of Torres et al. (2023). In the global ocean, this results in a lower volume mean κ_n, despite increased values in the upper ocean. However, reading the surface modes for the structure function in EKE-GM+N3D significantly reduces the final equilibrated EKE. Indeed, the expected surface-intensified EKE and the power law in Equation 4 contribute to an increase of the dissipation. Consequently, we diminish the value of C_ϵ to 0.013 to counteract this effect and reach similar levels of EKE as in the other experiments. This was necessary to obtain a similar global average κ_{gm} across the three sensitivity experiments. Note that the use of the surface modes to provide a vertical structure for κ_{gm} has been tested, but results in very weak EKE levels (see Figure D4). Therefore, this option was not considered further.

All four experiments are set up following the 61-year (1,958–2018) cycle defined by the OMIP-2 protocol (Tsujino et al., 2020). They are forced at the top ocean interface by the JRA55-do v1.5.0 reanalysis (Tsujino et al., 2018), using bulk formulae. In order to prevent model drifts, the sea surface salinity (SSS) is restored to a monthly climatology of salinity provided in the JRA55-do data set. It is computed as the upper 10 m average from the World Ocean Atlas 2013 version 2 (WOA13v2) (Zweng et al., 2013). A five-cycle spin-up is first run with the DEFAULT configuration. From this branch point, each of the four experiments is then run for four extra cycles, the last cycle being extended until 2022.

3. Evaluation of the Mesoscale Parameterization

3.1. Eddy Kinetic Energy

Our reference energy field is the three-dimensional observation-based EKE map of Torres et al. (2023). This map combines surface EKE computed from altimetry and baroclinic surface modes (de La Lama et al., 2016; LaCasce, 2017) obtained from World Ocean Atlas 2018 hydrographic data sets (Garcia et al., 2019). Here we employ the vertically integrated EKE field of Torres et al. (2023) to evaluate our parameterized EKE budget (Equation 1).

In our NEMO experiments, the EKE budget stabilizes within a few years, producing a global EKE reservoir comparable to those derived from observation-based data sets. Averaged over the 1995–2017 period of the last forcing cycle, the global domain-integrated EKE reaches 4.45 EJ (EJ = 10^{18}J) in EKE-GM, 4.44 EJ in EKE-GM+N and 4.41 EJ in EKE-GM+N3D. These results are very close to the targeted value of 4.42 EJ obtained by Torres et al. (2023) for the same time period. For comparison with studies using higher resolution simulations, von Storch et al. (2012) have found a reduced but comparable EKE reservoir of 3.55 EJ from a 1/10° global ocean model.

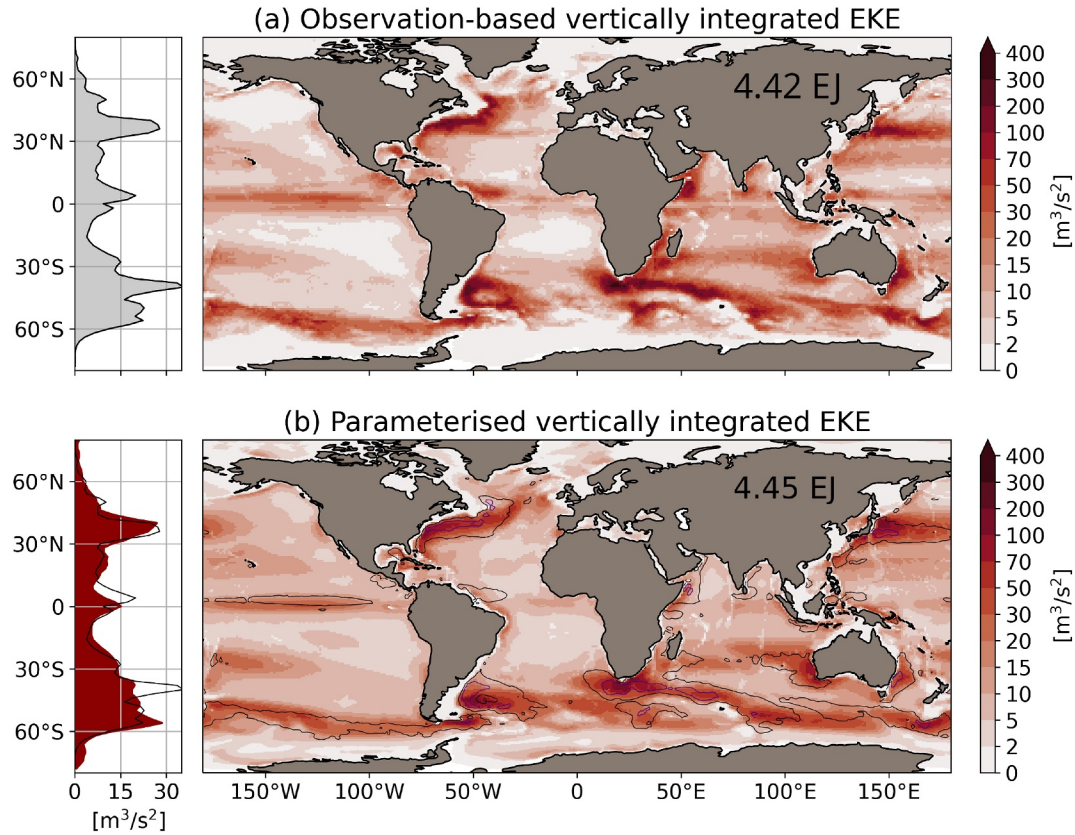

Figure 2. Vertically integrated eddy kinetic energy (EKE) ($m^3\ s^{-2}$) diagnosed from (a) the combination of altimetry data and a hydrographic climatology (Torres et al., 2023), and (b) the EKE-GM+N experiment, which solves the prognostic Equation 1. Note that the color-scale is non-linear. In panel (b) the EKE is averaged over the 1995–2017 period of the last forcing cycle. Contour lines in (b) represent the values of 20 $m^3\ s^{-2}$ and 100 $m^3\ s^{-2}$ from (a). Zonal averages of the same variables are plotted on the left-hand-side panels, with the observation-based reference (black curve) shown in both panels.

All three experiments possess very similar EKE fields. For conciseness, in the remainder of this section, we thus focus on the evaluation of EKE-GM+N, which defines both κ_{gm} and κ_n as function of EKE. The prognostic depth-integrated EKE obtained in EKE-GM+N shows general agreement with the estimation of Torres et al. (2023) (Figure 2). The parameterization is indeed able to reproduce both the patterns and the amplitude of the observation-based EKE. In the northern hemisphere, the mesoscale variability observed in the Gulf Stream and the Kuroshio is well captured, as evidenced by zonal mean views which show both the parameterized and observation-based EKE peak around 40°N. However, we found differences in the North Atlantic with high eddy energy penetrating farther east than in the observation-based estimate. This illustrates the difficulty of representing the Gulf Stream and its extension in coarse ocean models, yet it also illustrates that the mesoscale parameterization remains consistent with the resolved currents. In the southern hemisphere, the Southern Ocean EKE is very well predicted with hotspots in the correct locations, mostly along the northern flank of the Antarctic Circumpolar Current (ACC). The major boundary currents also have clear signatures and stand out as hotspots of mesoscale kinetic energy. At southern mid-latitudes, the parameterization performs well and the predicted depth-integrated EKE is very close to the one obtained from the reference. This is particularly evident in the Pacific where the mesoscale signature within subtropical gyres is well reproduced. However, the zonally averaged EKE exhibits a low bias around 40°S, likely due to an underestimation of the mesoscale activity in the Brazil-Malvinas and Agulhas systems, where the mean flow at low resolution is substantially biased. Finally, moderate to intense vertically integrated EKE is predicted at low latitudes, mainly due to equatorial jets leading to EKE production through the barotropic term B_T (Equation 3). We also note a weaker parameterized eddy energy in the North Brazil and Somali boundary currents than expected from the observation-based reference.

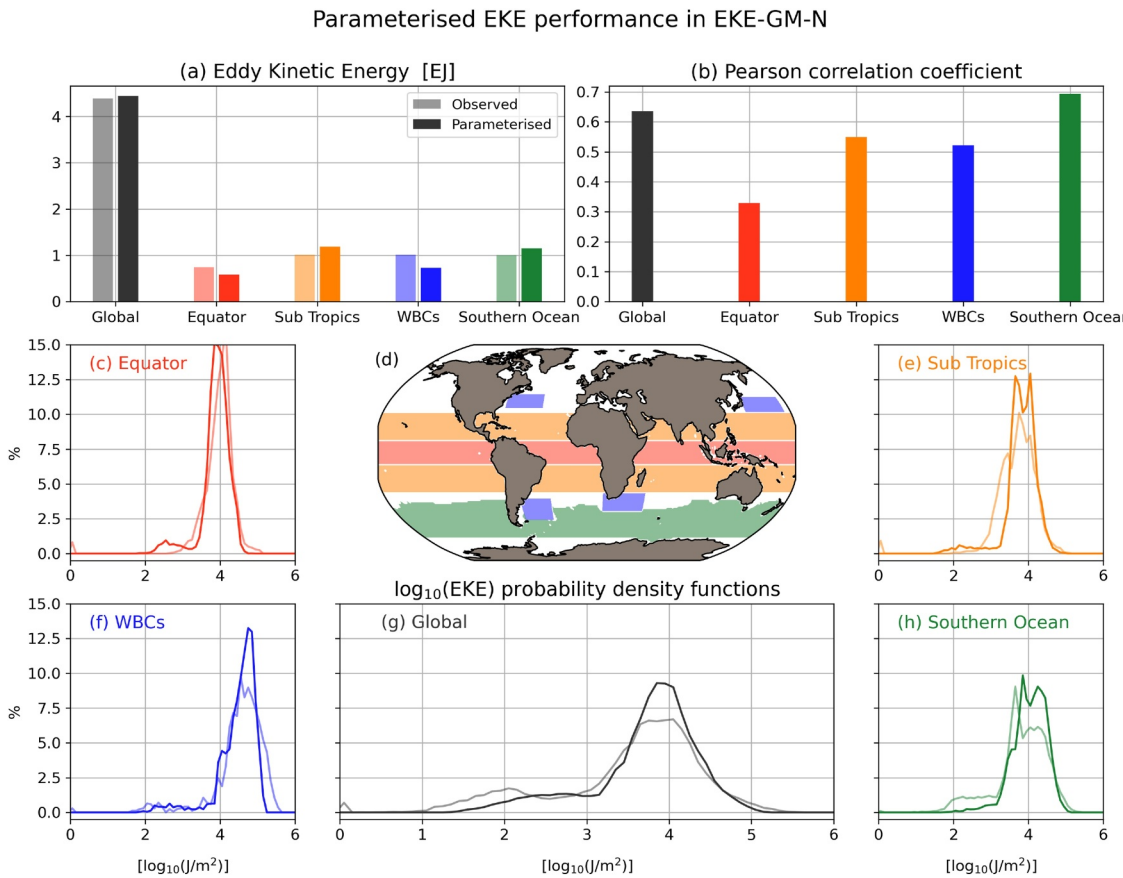

Figure 3. Domain-integrated eddy kinetic energy (EKE) and spatial correlation between parameterized and observation-based mesoscale eddy energy in different ocean domains: Global ocean (black), equatorial band (red), subtropics (orange), the four main western boundary currents (WBCs) (blue) and the Southern Ocean (green). Values from the observation-based reference are plotted in light colors. (a) EKE energy reservoirs (in EJ). (b) Spatial correlation coefficient by comparison with the observation-based estimate of the EKE. (c) Probability density function in the equatorial band. (d) Definition of the ocean basins. Panels (e–h) same as (c) but for the subtropics, the WBCs, the global and the Southern Oceans.

It is important to note that the observed variability in the equatorial band (Figure 2a) likely stems from dynamical processes other than mesoscale eddies, such as tropical instability waves. Some of these processes may be explicitly resolved at the resolution of our eORCA1 grid (Holmes et al., 2022). It is for these reasons that both eddy coefficients are numerically tapered around the equator (see Section 3.2). Consequently, an accurate prediction of EKE generation processes near the equator has less impact on the eddy transport parameterization and our hindcast simulations.

The performance of the presented parameterization to reproduce the EKE budget at coarse resolution is evaluated across multiple dynamical regions in Figure 3. Overall, the levels of domain-integrated eddy energy align with those estimated from indirect observations (Figure 3a). However, the model predicts a smaller domain-integrated EKE within the four primary WBCs selected due to lack of predicted mesoscale activity in the Brazil-Malvinas and Agulhas systems, as shown previously. The maps presented in Figure 2 are statistically analyzed to evaluate the spatial correlation between the predicted and observation-based EKE field (Figure 3b). Globally, the patterns show a correlation coefficient of 0.64. This degree of agreement is encouraging given that there is inherent bias in the circulation simulated by a coarse global ocean model. Over the different dynamical regions the correlation coefficient remains above 0.5, with the Southern Ocean exhibiting a stronger linear correlation with the observation-based reference approaching 0.7. The parameterization performs more poorly in the equatorial band, but this has only a minor impact on the values of κ_n and κ_{gm} in the region due to numerical tapering. Finally, the probability density function of EKE is analyzed in Figures 3c–3h. In all ocean regions analyzed, a quasi-lognormal distribution of vertically integrated EKE is observed. This feature is correctly reproduced by our parameterization. According to both the model and observations, the eddy energy peaks around 10^4 J m^{-2} in all

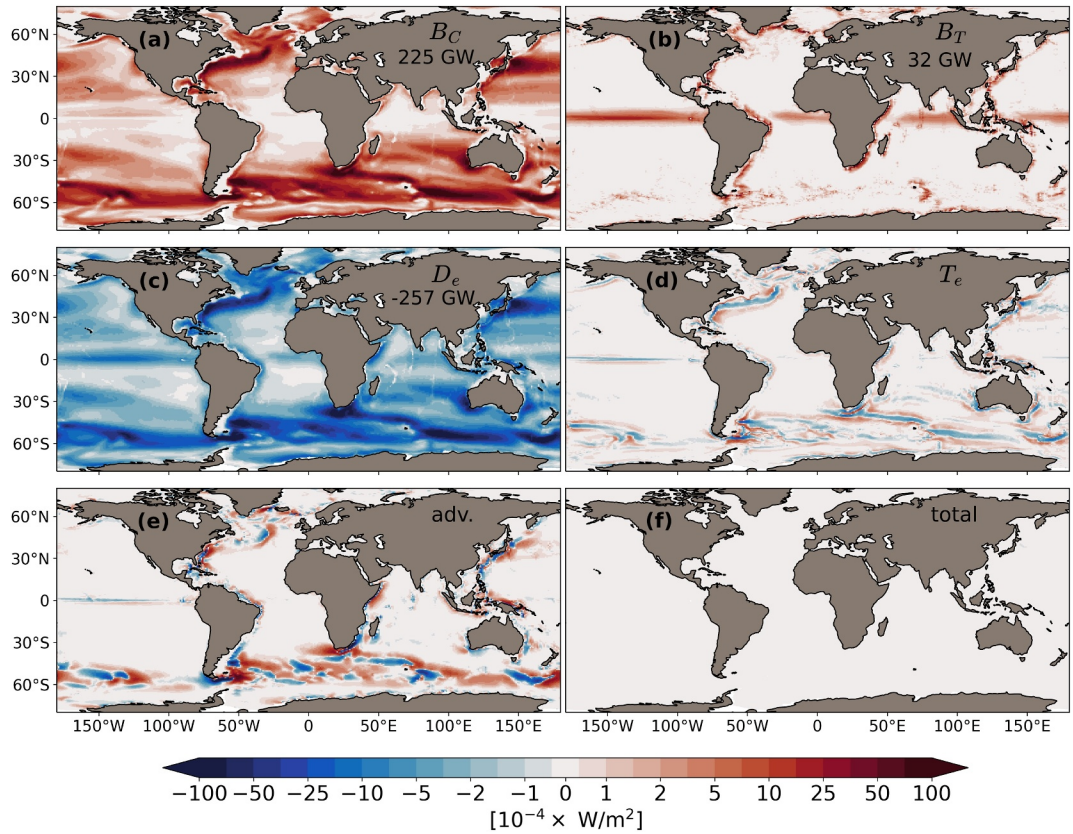

Figure 4. Depth-integrated energy transfers diagnosed from the parameterized eddy kinetic energy (EKE) budget averaged over the 1995–2017 period of the last forcing cycle, in the experiment EKE-GM+N. (a) Baroclinic source B_C, (b) barotropic source B_T, (c) dissipation D_e, (d) depth-integrated transport T_e, (e) advection by the resolved flow and (f) the time-rate of change. Global integrated value (in GW) is also indicated when significant.

regions but WBCs, where the peak is closer to 10^5 J m^{-2}. Regarding the distribution itself, the standard deviation is well captured for all selected regions. Interestingly, the mean value and the standard deviation of the observed quasi-lognormal distribution can be captured if the dissipation term of Equation 4 is used (see Figure E7 for a comparison of distributions obtained with a linear dissipation). This result is consistent with two-dimensional turbulence theory and simulations of the global ocean (Pearson & Fox-Kemper, 2018).

A climatological mean of the individual terms involved in our parameterized EKE budget (Equation 1) is presented in Figure 4. The eddy energy source term B_C dominates the production of EKE globally and is most intense in regions known to be prone to baroclinic instability, such as the Southern Ocean and major WBCs. To a lesser extent the subtropical gyres also exhibit widespread baroclinic production of EKE. The barotropic source term B_T shows the production of EKE due to intense shear found along equatorial currents as well as along WBCs in the vicinity of the coast. It is also active locally in the Southern Ocean, although it is of second order compared to its baroclinic counterpart. Integrated over the global ocean domain, these two fluxes provide an energy input of 225 and 32 GW for B_C and B_T, respectively. These values are of the same order of magnitude (although about three times smaller) as the equivalent fluxes computed by von Storch et al. (2012) from a high-resolution model. The dissipation flux D_e integrates to −257 GW, thus balancing the input of energy from the two above-mentioned instability terms. Indeed, the time-averaged change rate of EKE is negligible (Figure 4f), which confirms the budget equilibration.

The transport term T_e and the mean advection term only redistribute the eddy energy regionally, hence they display negative/positive dipoles focused in region of intense EKE levels (Figures 4d and 4e). The T_e term clearly smooths the EKE field, spreading EKE around the core of major fronts and currents, such as in the Gulf Stream and Agulhas retroflection regions. The advective term shows more complex structures, but its main effect is to

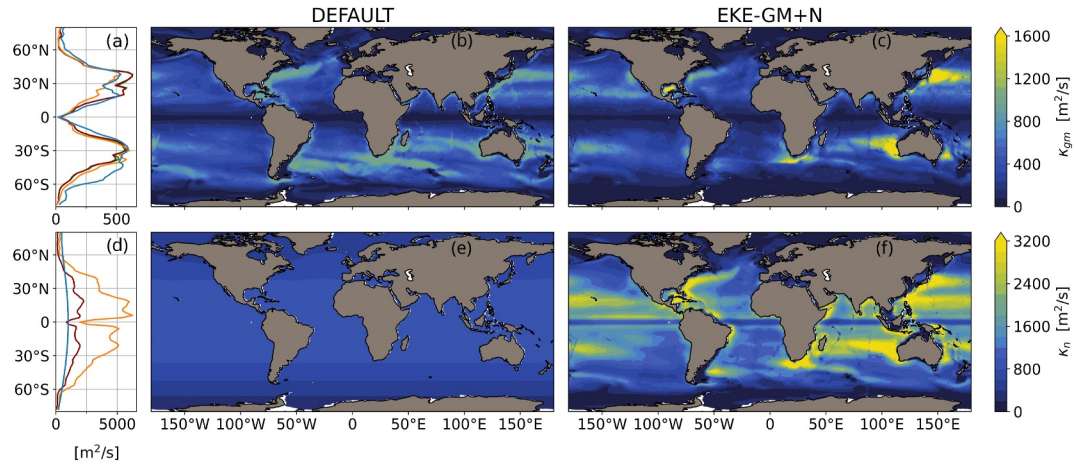

Figure 5. Spatial distributions of (b, c) κ_{gm} and (e, f) κ_n at the surface in the DEFAULT and EKE-GM+N simulations. Zonal mean of the surface eddy coefficients are plotted on the left panel (a, d) for the DEFAULT (blue), EKE-GM (green), EKE-GM+N (dark red), and EKE-GM+N3D (orange) experiment. Variables are averaged over 1995–2017 of the last forcing cycle.

spread EKE along the main ocean currents. Its effect is particularly important in the Southern Ocean, where the circumpolar current advects the energy produced by baroclinic instability (B_C) eastward, as evidenced by blue-red dipoles in the zonal direction.

As discussed in Section 2.3, the formulation of the dissipation term (Equation 4) has been instrumental in improving the energy distribution (see also results from the calibration in Appendix E). In the ocean, several processes are known to dissipate or extract kinetic energy from the mesoscale reservoir (Klymak, 2018; Molemaker et al., 2010; Polzin, 2010; Rai et al., 2021; Sen et al., 2008) yet there is no consensus on whether this energy flux is primarily downscale (Barkan et al., 2015; Evans et al., 2022) or upscale (Sérazin et al., 2018). Our results suggest that this energy flux is well approximated by a form based on dimensional analysis, which is often justified by the assumption of an inverse turbulent energy cascade (Eden & Greatbatch, 2008). Although it is not possible to draw definitive conclusions, this lends support to the notion that the inverse energy cascade is an important energy flux to parameterize in coarse-resolution ocean models. However, it is not the aim of this study to reinject the mesoscale EKE loss into the resolved flow, as was previously undertaken by Bachman (2019) and Jansen et al. (2019), for example. Instead, our aim is to simulate a realistic subgrid EKE field to specify energetically and observationally constrained κ_{gm} and κ_n coefficients.

3.2. Eddy Coefficients

The horizontal distributions of κ_{gm} and κ_n for the DEFAULT and EKE-GM+N experiments are shown in Figure 5, which also includes zonal averages for all simulations.

In DEFAULT the effect of the mean flow shear on κ_{gm} can be seen with the strongest values obtained in the boundary currents and their extensions (Figure 5b). It is worth noting that the coefficient is typically saturated in those regions due to the 1,000 $m^2\ s^{-1}$ upper limit. When using the EKE formulation of Equation 6 in experiments EKE-GM, EKE-GM+N and EKE-GM+N3D, the values of κ_{gm} remain enhanced nearby boundary currents, although they progressively weaken in their extension (Figure 5c). Compared to DEFAULT, the gyre signatures are also more pronounced in the Pacific and Indian Oceans with increased κ_{gm} in the Kuroshio, the East Australian Current and in the core of the Agulhas current. This results in larger zonally averaged values between 20°N and 40°N, even if it is reduced at higher latitudes, in the North Atlantic Current and subpolar gyre. The Southern Ocean exhibits the strongest difference between the simulations using the EKE formulation and DEFAULT: the former produces much lower κ_{gm} poleward of 40°S (Figures 5b and 5c). This is primarily attributable to the expected large horizontal density gradient caused by the ACC and the inverse dependence of κ_{gm} to M^2 in Equation 6. Another reason is attributable to the use of a small eddy efficiency α of 0.04. While this value is selected to optimize the fit with the observational-based EKE map (Figure 2a), it should be noted that larger alpha

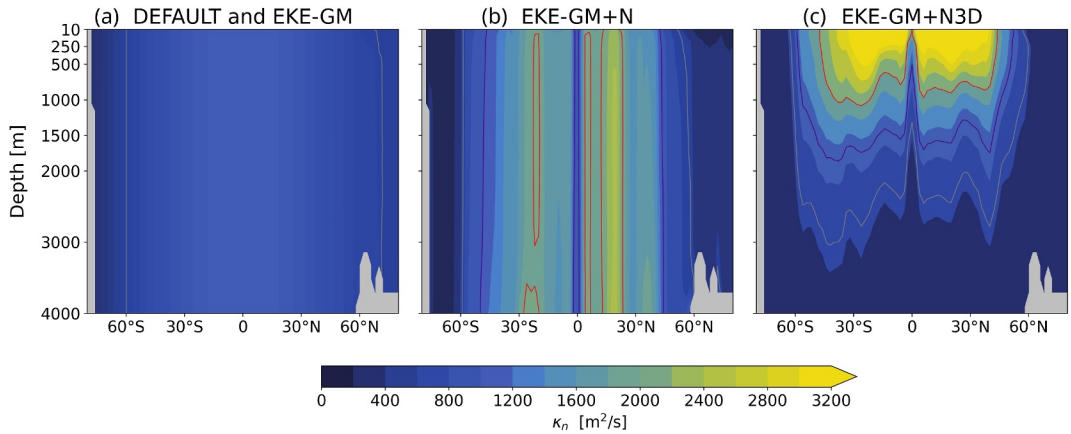

Figure 6. Zonal mean of the neutral diffusivity κ_n in DEFAULT and EKE-GM (a), EKE-GM+N (b), and EKE-GM+N3D (c) showing surface-intensified mixing when adding the vertical structure function following surface modes. The gray, purple, and red contours represent the isolines 500, 1,000, and 2,000 m^2 s^{-1}, respectively. Note that due to the bathymetry, the zonal-averaged κ_n is not exactly constant with depth in (a) and (b).

could also result in satisfactory parameterized EKE levels (see Figure E5 and associated text in Appendix E). However, we note that our parameterized GM coefficient in the Southern Ocean remains comparable to the one recently derived from observational data by Kusters et al. (2025). Finally, in all our experiments, the values of κ_{gm} are tapered between 20°N and 20°S to reach zero at the equator (Madec et al., 2017).

Use of the mixing length formulation for κ_n generates a complex spatial distribution of the eddy diffusivity (Figure 5f) which contrasts with the simple latitude dependence in the DEFAULT and EKE-GM configurations (Figure 5e). At low to middle latitudes the diffusivity is overall increased, and in particular WBCs and subtropical gyres show strong signatures including the highest predicted values of the neutral diffusivity. Similarly to κ_{gm}, the diffusivity is tapered near the equator to account for the resolved mesoscale variability. Values of κ_n in EKE-GM+N also decline at high latitudes mainly due to the linear dependence with the local Rossby radius in Equation 7. Poleward of 45°N and 60°S the neutral diffusivity becomes lower than that of DEFAULT in the zonal average (Figure 5d). Low levels of simulated EKE (Figure 2b) and short Rossby radii together lead to muted mesoscale mixing in subpolar and polar seas.

Experiment EKE-GM+N3D uses pre-computed vertical modes for the structure function $\phi(z)$ in Equation 7 which in turn reduces κ_n with depth (Figure 6). As a consequence of keeping the depth-integrated EKE to levels comparable to the other simulations, the surface value of EKE (EKE$_0$ in Equation 7) is much higher in EKE-GM+N3D. Therefore, κ_n is strongly increased in the upper ocean above 1,000 m depth (Figure 6c). However, the structure function does not significantly change the horizontal patterns of κ_n which remain comparable to the one presented in Figure 5. It must be emphasized that the strong isopycnal gradients of temperature and salinity typically observed at latitudes between 40° and 60° and from surface to intermediate depths can lead to substantial diffusive isopycnal transport in these regions. One can thus expect the vertical distribution of κ_n in EKE-GM+N3D to increase isopycnal tracer transports compared to the other experiments.

4. Impacts on the Ocean State

This section presents a comparison of the results obtained from our hindcast experiments. The aim is to demonstrate the impact of novel distributions of the eddy diffusivities on ocean circulation, with a particular focus on large-scale circulation and heat storage. These features ultimately affect both the mean state and the variability of climate.

As we have shown, the new parameterization results in a reduction in the magnitude of κ_{gm} in subpolar and polar regions. The largest differences compared to DEFAULT can thus be expected to unfold at high latitudes. This is particularly the case in the Southern Ocean, where κ_{gm} is known to affect the residual overturning circulation and density stratification (Farneti et al., 2010). In order to assess the sensitivity of the ocean circulation to the value of κ_{gm} in high latitudes, two additional sensitivity tests with reduced κ_{gm} were conducted and are presented in

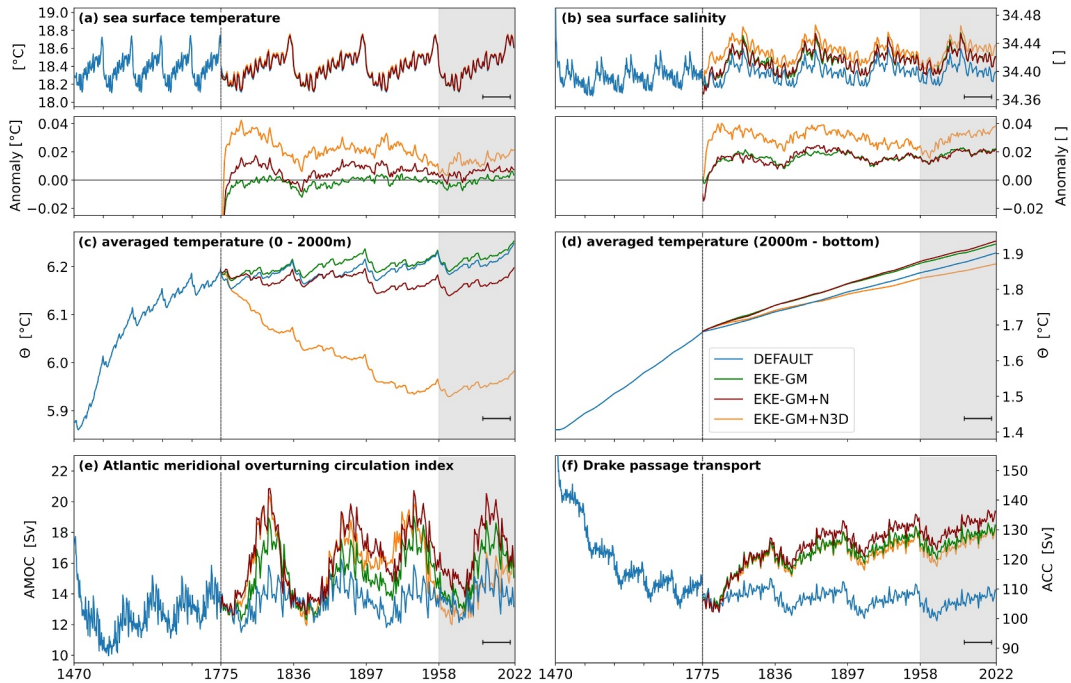

Figure 7. Time series of annual mean ocean metrics: (a) global sea surface temperature, (b) global sea surface salinity, (c) volume averaged potential temperature from 0 to 2,000 m depth, (d) volume averaged potential temperature from 2,000 to 6,000 m depth, (e) Atlantic Meridional Overturning Circulation transport at 26°N calculated as the maximum of the Atlantic overturning streamfunction at this latitude and (f) Antarctic Circumpolar Current transport calculated as the eastward volume transport through Drake Passage. In panels (a, b), anomalies with respect to the DEFAULT run are also plotted. The simulations were spun-up for five OMIP2 cycles using the DEFAULT configuration and then run during four other cycles with modified mesoscale transports. The shaded zone represents the last cycle while the horizontal black line shows the 1995–2017 period used to compare the simulations. Note the *x*-axis range for the spin-up is compressed in order to focus on the comparison.

Appendix C. On the other hand, κ_n can only indirectly alter the density field, so the impact of its new formulation on circulation will likely be less clear. Isopycnal tracer mixing can affect the density field through the non-linearity of the equation of state (Iudicone et al., 2008; Klocker & McDougall, 2010) and through modified sea surface temperatures (SST) and air-sea exchanges (Chouksey et al., 2022; Guilyardi et al., 2001; Holmes et al., 2022; Pradal & Gnanadesikan, 2014). In addition, in our NEMO ocean model, isoneutral slopes are bounded by 1/100 and progressively reduced from the calculated value at the base of the mixed layer to zero at the surface (Madec et al., 2017). This implies that neutral mixing transitions to horizontal (diapycnal) mixing in the surface mixed layer. Since κ_n is intensified near the surface and at intermediate depths in EKE-GM+N3D, all the aforementioned effects should be more pronounced in EKE-GM+N3D. Besides, as pointed out in Table 1, the use of the vertical function in EKE-GM+N3D can slightly alter the distribution of κ_{gm} through the EKE field.

We start by comparing the adjustment of integrated ocean metrics to the mesoscale parameterization in the four experiments (Figure 7). The global average of SST shows sensitivity to κ_n and insensitivity to κ_{gm}, with warmer surface waters observed in EKE-GM+N and EKE-GM+N3D but not in EKE-GM (Figure 7a). This result is in line with the findings of Pradal and Gnanadesikan (2014), which indicate that global mean SST increases with κ_n. However, as noticed by Holmes et al. (2022), this SST change could be temporary and longer simulations are needed to confirm the long-term response. By contrast, the global mean sea surface salinity (SSS) seems more impacted by the changes in κ_{gm} than the new horizontal distribution of κ_n: the same increase of 0.02 psu of the global mean SSS is simulated in EKE-GM and EKE-GM+N (Figure 7b). Nonetheless, adding the vertical structure to κ_n has an important effect, increasing the global mean SSS by an extra +0.015 psu (Figure 7b), suggesting that κ_n can also influence the SSS.

Figures 7c and 7d display the volume-averaged temperature for two depth ranges: 0–2,000 and 2,000–6,000 m. In all experiments, upper-ocean temperatures vary strongly with the cycling forcings, whereas abyssal temperatures display a quasi linear upward drift throughout the simulation length. This abyssal temperature drift is shared by

other global ocean models evaluated using the OMIP protocol (Tsujino et al., 2020), and it is only slightly affected by differences in parameterized mesoscale transports (Figure 7d). In the 0–2,000 m layer, anomalies in ocean heat content across experiments (Figure 7c) show a hierarchy opposite to SST (Figure 7a): a warmer (or colder) surface is associated with a cooling (or warming) of intermediate waters. We infer that the positive temperature anomalies at the surface in EKE-GM+N are the result of heat extraction from relatively warm and salty intermediate waters (Guilyardi et al., 2001; Holmes et al., 2022). In this experiment, κ_n is indeed increased in latitudes between 40° and 60° coinciding with regions where isopycnals are the steepest. This result confirms that neutral mixing can drive large tracer exchanges between surface and intermediate depths, a process even more pronounced in EKE-GM+N3D due to the intensified values of κ_n near the surface (Figure 6). On the other hand, κ_{gm} seems to have a smaller impact on the 0–2,000 m heat content. However, the global average view can be misleading and may hide regional disparities.

By changing tracer distributions, the new parameterization can also affect the large-scale ocean circulation. We now examine two major circulation metrics: the strength of the Atlantic Meridional Overturning Circulation (AMOC) at 26°N and the ACC strength at Drake Passage. Both metrics respond quickly to changes in the eddy coefficients (Figures 7e and 7f). The new parameterization generates a marked intensification of the AMOC. This increase stems primarily from the modified κ_{gm} (green curve in Figure 7e), though changes in κ_n as per EKE-GM+ N also contribute (red curve in Figure 7e). The multidecadal AMOC variability remains in phase across all simulations, with a peak reached at the same period of each repeated cycle, illustrating that it is paced by the surface forcing. However, the amplitude of this variability is increased in the experiments with energy-based mesoscale transports. In the three experiments EKE-GM, EKE-GM+N and EKE-GM+N3D, the ACC speeds up quickly during the first common cycle (1775–1836). At the end of the last cycle, the transport averaged over the 1995–2017 period reaches 128.6 Sv (10^6 m^3 s^{-1}) in EKE-GM, 133.1 Sv in EKE-GM+N and 127.5 Sv in EKE-GM+N3D while a lower value of 107.2 Sv is found for the DEFAULT experiment. The reduction in κ_{gm} values south of 40°S is the main cause: it leads to meridional steepening of isopycnals and zonal flow acceleration through thermal wind adjustment (see also Section 4.2).

In the following, we analyze in more detail three main large-scale features impacted by the parameterization: (a) ocean meridional heat transport (MHT) and global heat storage, (b) Southern Ocean circulation and (c) North Atlantic circulation.

4.1. Meridional Heat Transport and Global Heat Storage

In all experiments, the mesoscale parameterization influences the ocean meridional heat transport (MHT) both directly since κ_{gm} and κ_n are involved in the tracer equations, and indirectly by induced changes of the mean circulation. Figure 8 shows meridional heat transports in all simulations. In the northern hemisphere, the transport due to the Eulerian-mean circulation is increased when the new parameterization is active (Figure 8a). This result is consistent with the previously discussed AMOC strengthening. This strengthening of the Atlantic upper overturning cell also explains the global reduction of the southward Eulerian heat transport in the southern hemisphere, north of 35°S, although a decrease in the MHT in the Indian-Pacific sector (not shown) is also a contributing factor. In the Southern Ocean, the parameterization tends to decrease the Eulerian mean northward transport which results from both a southward shift of subtropical gyres and a reduction of the overturning component (not shown). This effect is due to changes in κ_{gm}, and it is partly counteracted by the modified κ_n in EKE-GM+N and EKE-GM+N3D. In all three experiments including energy-constrained mesoscale transports, the peak of the Eulerian mean MHT at 45°S is shifted to the north, likely due to a southward shift of subpolar gyres and of the ACC fronts. Changes in the Southern Ocean circulation are analyzed in further detail in Section 4.2.

Figure 8b shows the contribution of the parameterized eddy-induced circulation. It is most active in latitudinal bands comprised between 30° and 50° (60° in the southern hemisphere) and consists in a poleward heat transport that peaks around 0.2 PW, in line with previous MHT decompositions. For instance, Yang et al. (2014) found a peak of −0.3 PW and +0.1 PW for the GM eddy-induced MHT in the southern and northern hemispheres, respectively. In the Southern Ocean, the new energy-constrained parameterization employed in EKE-GM, EKE-GM+N, and EKE-GM+N3D reduces this poleward heat transport, in accord with reduced κ_{gm}. In the northern hemisphere, a slight increase in the heat transport results from higher κ_{gm} in the Pacific subtropical gyre. We also note lower differences in the three-dimensional case EKE-GM+N3D caused by potential changes in the EKE distribution when using the vertical structure. As expected, the MHT due to the neutral diffusion (Figure 8c) is

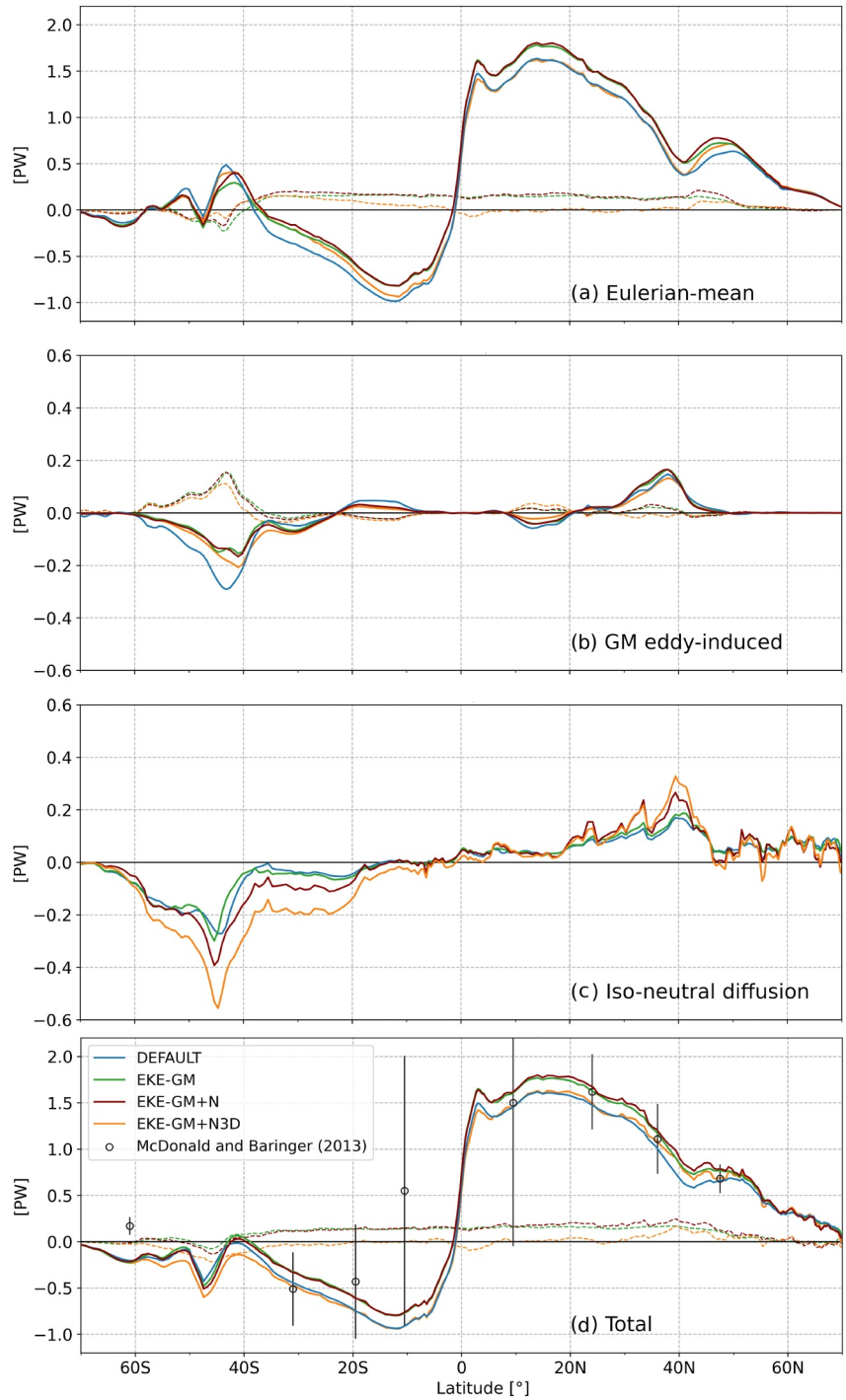

Figure 8. Global meridional heat transport diagnosed in the four experiments for different contribution: (a) the Eulerian-mean transport, (b) the parameterized eddy-induced circulation, (c) the transport due to the isoneutral diffusion and (d) the total transport. Solid lines show the meridional transport for a given latitude while dotted lines are anomalies with respect to DEFAULT. In panel (c), anomalies are not shown for clarity. In panel (d), observational estimates from Macdonald and Baringer (2013) are shown as circles with uncertainties depicted by vertical bars.

almost unaffected by κ_{gm} apart from a slight southward shift of the maximum transport, probably also caused by the position of the ACC. However, the global effect of the modified κ_n in EKE-GM+N and EKE-GM+N3D is easily interpretable. Apart from high latitudes, the neutral diffusivity κ_n is overall increased, which in turn boosts

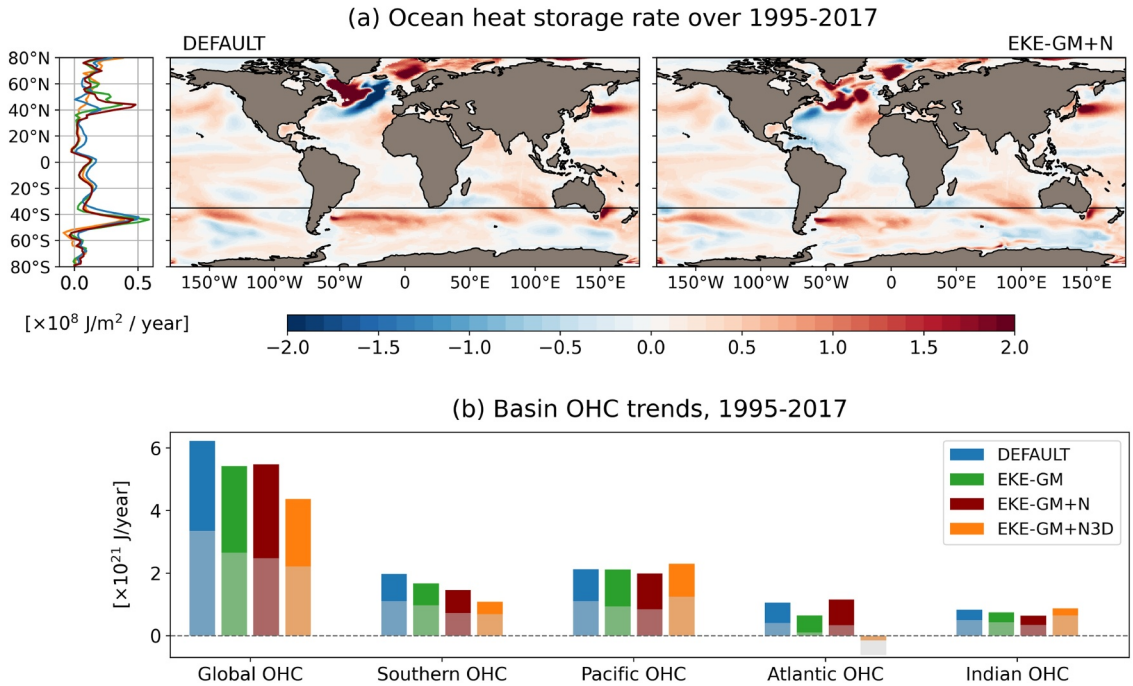

Figure 9. Spatial distribution of the simulated ocean heat storage. (a) Heat storage rate computed as the linear trend of the ocean heat content in DEFAULT (middle) and EKE-GM+N (right) over 1995–2017. The zonal means of the heat storage, weighted by area cells, are also plotted for all the experiments (left). (b) Ocean heat content trends computed in different ocean basins shown as a histogram. Lighter shading represents trends in the 0–2,000 m layer only. The Southern Ocean is defined by the 35°S line plotted on the maps in (a).

its contribution to the MHT. Changes in the total MHT (Figure 8d) are dominated by the Eulerian anomaly almost everywhere. In the Southern Ocean however, the poleward transport is increased south of 45°S through a combination of (a) a reduced northward mean transport, (b) a reduced poleward eddy-induced advection and (c) an increased isoneutral diffusion. The latter is even of leading order in EKE-GM+N3D and explains the increase of the southward heat transports poleward of 20°S.

By changing the ocean heat transport, the mesoscale parameterization also affects the ocean heat storage distribution (Figure 9). Computed over the 1995–2017 period, the ocean heat content has a linear trend of 6.2 YJ/year in DEFAULT. This trend reduces to 5.5 YJ/year in EKE-GM and EKE-GM+N and 4.5 YJ/year in EKE-GM+N3D. This reduced heat storage occurs primarily in the subsurface and intermediate layers (0–2,000 m), even if the three-dimensional κ_n case also slows down the continuous abyssal warming (Figures 7c and 7d). The Atlantic shows the most significant patterns with high ocean warming located in the western subpolar gyre and Nordic Seas. In DEFAULT, the subpolar region shows a west-east dipole characterized by warming in the interior of the subpolar gyre and cooling further east. This dipole still exists in the other simulations but is shifted to the south with a net cooling of the Gulf Stream area (Figure 9a). A cooling in the low latitudes of the Atlantic is also apparent. Changes in the northern Atlantic likely result from adjustments of the North Atlantic Current, the large-scale meridional circulation and the surface heat fluxes. In EKE-GM and EKE-GM+N, due to the reduced poleward heat transport at 35°S, the Southern Ocean warming is reduced compared to DEFAULT. In EKE-GM+N3D, the Southern Ocean warming reduction is not related to the MHT but rather to a globally reduced heat uptake caused by increased isopycnal diffusive heat flux from the subsurface to the surface (Figures 7a, 7c, and 7d). In the Indian and Pacific basins, all simulations show similar trends in ocean heat content, suggesting that most of the model sensitivity comes from altered large-scale circulation in the Southern and Atlantic Oceans. However, we note that EKE-GM+N3D has a different behavior with a slight warming acceleration of the Pacific and Indian Oceans, a process that occurs in the 0–2,000 m layer.

4.2. Southern Ocean

The ACC is governed by complex dynamics including not only mesoscale and submesoscale turbulence, but also surface fluxes of momentum and buoyancy, bottom topography and long baroclinic Rossby waves (Olbers et al., 2004). Recent observations from Drake Passage indicate a volume transport of 173.3±10.7 Sv (Donohue et al., 2016). In eddy-parameterized ocean models, this zonal transport is sensitive to the mesoscale eddy coefficients (Kuhlbrodt et al., 2012). In particular, reducing the value of κ_{gm} increases the isopycnal slopes in the ACC, thus increasing the meridional density gradient and, via thermal wind, the eastward flow. As previously pointed out in Figure 7f, the new parameterization increases the ACC transport by more than 20 Sv, as expected due to the κ_{gm} decrease south to 40°S (Figure 5).

Borowski et al. (2002) showed that the zonal transport in the Southern Ocean can be approximated by the meridional gradient of the baroclinic potential energy $\chi = g/\rho_0 \int_{-h}^{0} \rho' z \, dz$, with g the gravitational acceleration, ρ' the density anomaly with respect to the horizontal mean density profile $<\rho>$ and z the vertical coordinate. The baroclinic potential energy χ reflects the ocean mass distribution in the water column and its horizontal gradient is tied to depth-integrated geostrophic transports. Offline calculation of the barotropic streamfunction ψ_b and a reconstruction of ψ from the baroclinic potential energy are shown in Figures 10a and 10c for DEFAULT. Both metrics exhibit similar patterns with an overall meridional gradient. When activating the new parameterization, the meridional gradient intensifies in all three experiments (Figures 10b and 10d), in line with the diagnosed ACC acceleration at the Drake Passage (Figure 7f). The similarity between the anomaly of ψ_b and its reconstruction demonstrates that changes in the density distribution are the main factors driving the increase in ACC transport. Furthermore, we find a southward shift of the ACC relative to DEFAULT, likely attributable to a shift of the southern subtropical gyres.

By changing the meridional transport, the mesoscale parameterization also affects Southern Ocean tracer distributions. Figures 11c–11f show the zonal mean temperature bias in the Southern Ocean in the four experiments. Overall, the parameterization reduces the temperature bias poleward of 37.5°S. In particular, the root mean square error computed from the top to the first 2,000 m depth is 0.28°C in DEFAULT, 0.23°C in EKE-GM, 0.21°C in EKE-GM+N and 0.22°C in EKE-GM+N3D. In EKE-GM, the impact of κ_{gm} is clear with dense colder waters found poleward of 55°S in accord with the increase of baroclinic potential energy at those latitudes (Figure 10). This significantly reduces the temperature bias below 100 m depth. Interestingly, it also affects subsurface waters north of 60°S. Indeed, the cold and warm biases found around 55°S and 40°S respectively are penetrating deeper due to the changes in isopycnal surfaces. In contrast, κ_n has a minimal impact on the density field here but impacts the isopycnal transport of tracers. In EKE-GM+N, the reduction of subsurface temperature is due to increased diffusion of cold surface temperatures to depth through the increase in κ_n, in addition to isopycnal slope changes via κ_{gm}. This mechanism is consistent with the increased poleward heat transport shown in Figure 8c. It explains the warm and saline surface anomalies (Figures 7a and 7b) and the relative cooling of the ocean in the 0–2,000 m layer (Figure 7c). In EKE-GM+N3D, the impact of κ_n is enhanced and leads to a net reduction of the Southern Ocean warming. However, we note that the cold bias located at intermediate depths is increased, suggesting κ_n values may be excessive. Implementation of mixing suppression by mean flows in Equation 7 (Ferrari & Nikurashin, 2010; Groeskamp et al., 2020) could potentially improve the model performance, especially in the Southern Ocean where the strong circumpolar zonal current can substantially diminish the ability of mesoscale eddies to mix across the current.

4.3. North Atlantic

As previously commented on the AMOC strength timeseries (Figure 7e), κ_{gm} and κ_n influence the meridional overturning circulation. In all EKE-GM, EKE-GM+N and EKE-GM+N3D, a stronger AMOC is simulated, suggesting changes in κ_{gm} are of leading importance. When using the energy to constrain κ_{gm} the upper overturning cell of the Atlantic is substantially increased, the circulation strength being closer to the observational estimate from the RAPID array (Moat et al., 2023), which measures the meridional circulation at 26°N (Figure 12a). At this latitude the mean (1995–2017) meridional streamfunction peaks at 16.9 Sv in EKE-GM, 18.3 Sv in EKE-GM+N and 15.1 Sv in EKE-GM+N3D, against 14.3 Sv in DEFAULT. In all the experiments, the peak value of the AMOC is reached between 700 and 800 m depth, whereas observational data from RAPID indicate a deeper streamfunction maximum near 1,200 m depth. The meridional shape of the AMOC also remains essentially unchanged across experiments (Figures 12b and 12c). Holmes et al. (2022) have hypothesized that

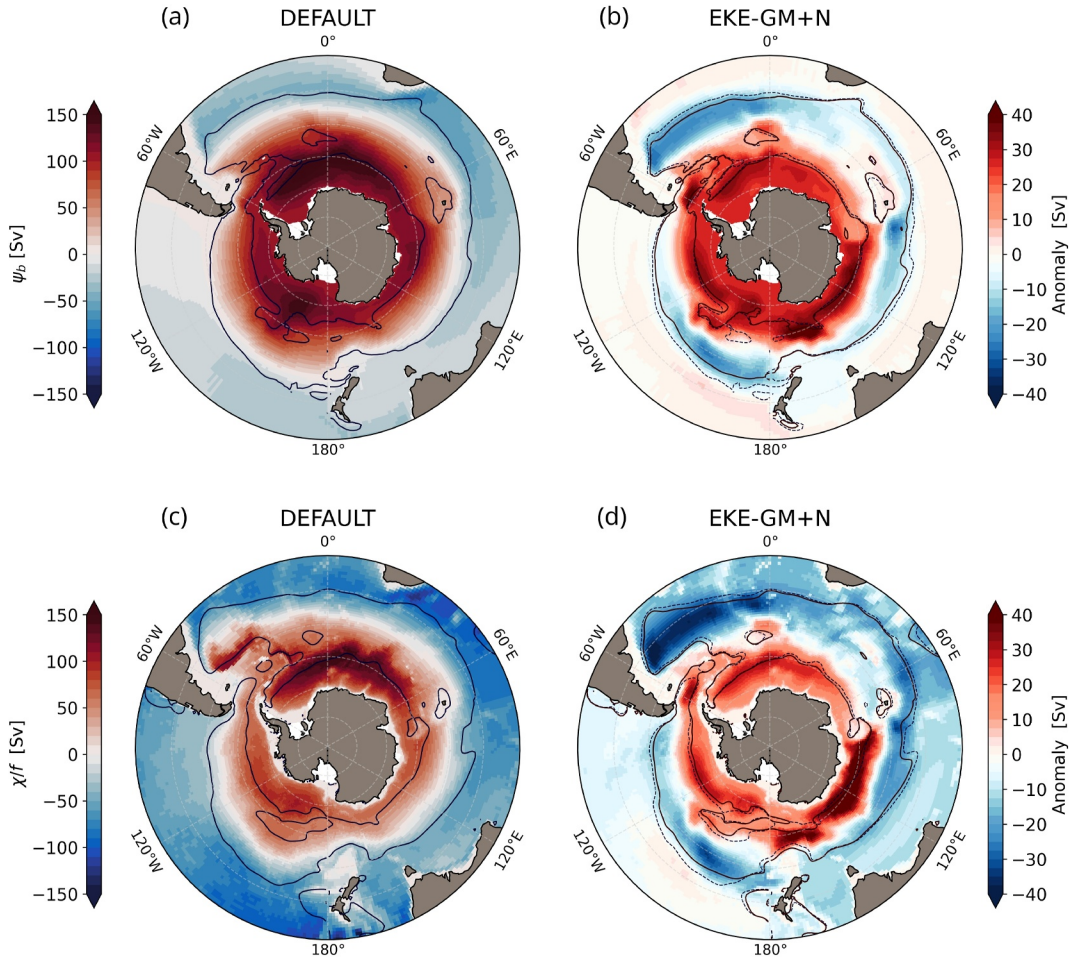

Figure 10. (top) Barotropic streamfunction averaged over the 1995–2017 period in (a) DEFAULT and (b) the anomalies in EKE-GM+N with respect to DEFAULT. (bottom) Reconstruction of the streamfunction from the baroclinic potential energy $\chi = g/\rho_0 \int_{-h}^{0} \rho' z\, dz$ in (c) DEFAULT and (d) the anomalies in EKE-GM+N with respect to DEFAULT. Solid lines show the 40 $m^2\ s^{-1}$ zonal transport line and represent the Antarctic Circumpolar Current contour. The contours in DEFAULT are superimposed in dashed.

changes in κ_n in the Southern Ocean can alter the temperature and salinity gradients along steep isopycnals around 40–50°S, which can exert an influence on the AMOC. They found that smaller eddy diffusivities lead to a stronger overturning circulation. This mechanism could explain the weaker AMOC diagnosed in EKE-GM+N3D since κ_n is largely intensified in the upper 1,500 m compared to EKE-GM+N. However, we found a stronger AMOC in EKE-GM+N than EKE-GM despite the fact that κ_{gm} is almost unchanged and κ_n is globally increased north of 60°S. This different response could be related to the enhanced poleward salt transport induced by changes in κ_n, which contributes to invigorate deep water formation in the North Atlantic.

The AMOC has long been assumed to be linked to winter deep convection and the formation of North Atlantic Deep Water (NADW) (Lozier, 2012). In DEFAULT, the main simulated convection sites are located in the Nordic Seas as shown by the annual maxima of mixed layer depth (MLD) (Figure 13), and secondary convection sites are found in the subpolar gyre including in the Labrador and Irminger Seas. However, the specification of κ_{gm} can have a significant impact on the simulated wintertime deep convection. In EKE-GM, zonally averaged values of κ_{gm} are reduced north of 50°N compared to DEFAULT (Figure 5), which tends to reduce the stratification at these latitudes, particularly in the North Atlantic subpolar gyre (J. Marshall & Schott, 1999). In turn, this enhances convection events and increases NADW formation in line with the conclusions of Ruan et al. (2023). In EKE-GM maxima of MLD are consequently increased almost everywhere inside the subpolar gyre, with the Labrador Sea being the most noticeable change. In EKE-GM+N, the new specification of κ_n alters the MLD maximum in a

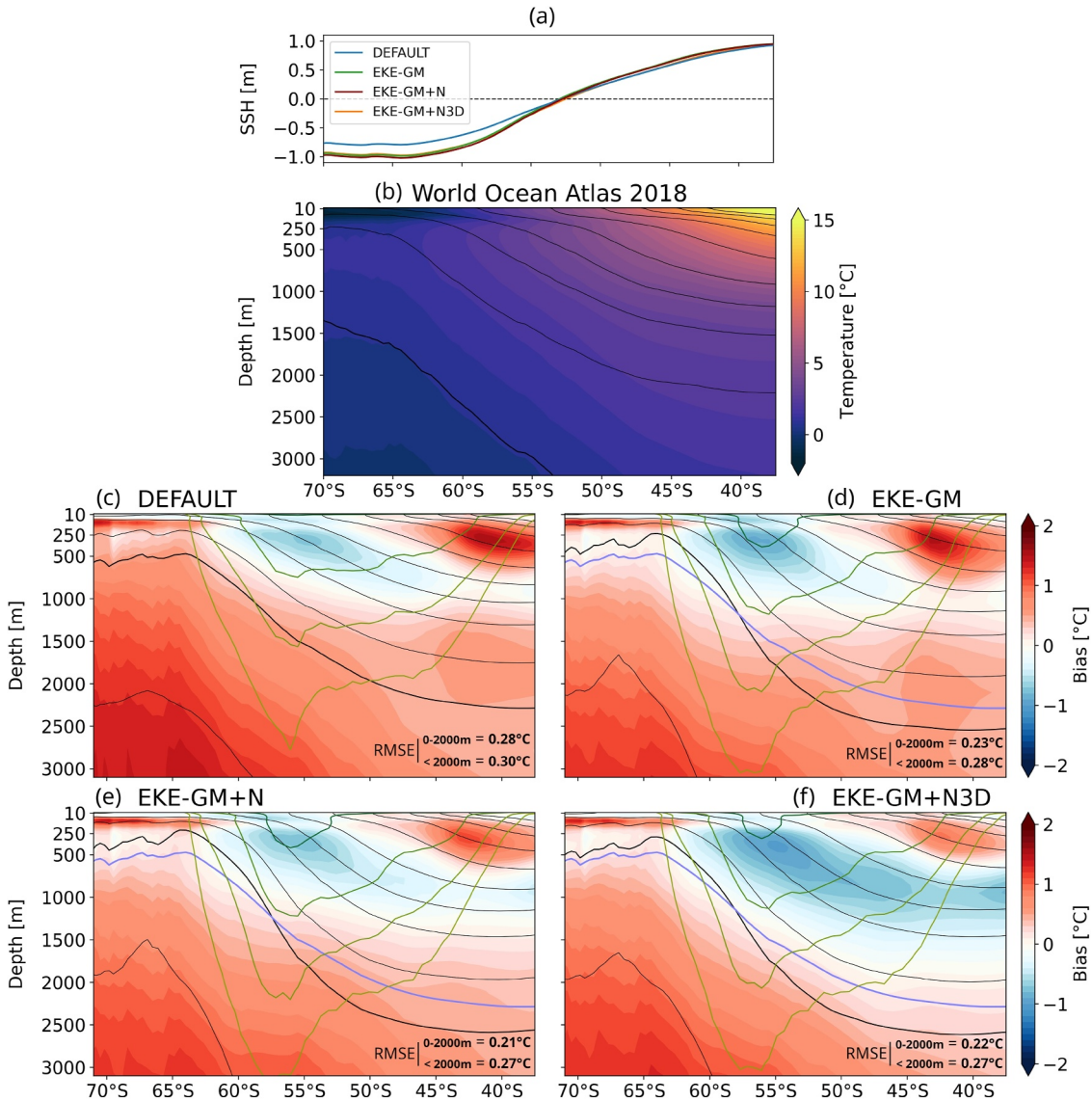

Figure 11. (a) Meridional profile of the sea surface height diagnosed in the Southern Ocean for each experiment; (b) zonal mean of the potential temperature obtained from the World Ocean Atlas 2018 (Garcia et al., 2019) and (c–f) bias from the numerical simulations. Thin black lines refer to mean potential density σ_0 at 0.2 kg m^{-3} intervals. The thick lines show $\sigma_0 = 27.7$ kg m^{-3} for each run (in black) and DEFAULT (in blue). Green lines represent the contours of simulated zonal velocities of 1, 2, 4, and 8 cm s^{-1}.

subtle way. Indeed, while an overall increase is observed in the subpolar gyre, the maximum of MLD has decreased by up to 500 m (about 20%) in the two main convection sites of the Nordic and Labrador Seas. In the latter case, this is accompanied by an increase of the MLD along the western boundary. In EKE-GM+N3D, the parameterization tends to homogenize the annual maximum MLD within both the Labrador and the Nordic Seas. These results show that κ_n can also influence convection events.

Modeling studies have long emphasized the importance of changes in Labrador Sea deep convection and Labrador Sea deep density anomalies in the low-frequency AMOC (Buckley & Marshall, 2016; Waldman et al., 2021; Yeager et al., 2021; R. Zhang et al., 2019). Furthermore, it is the region where the MLD is most affected by our parameterization. We therefore diagnose the mean density profiles in two areas of the Labrador Sea (Figure 14). The first one incorporates the main convection sites diagnosed in EKE-GM and is defined by the inner red contours in Figure 13. The area is then extended to include the western boundary deep convection sites as viewed by the black outer box. In EKE-GM and EKE-GM+N, waters are remarkably dense compared to

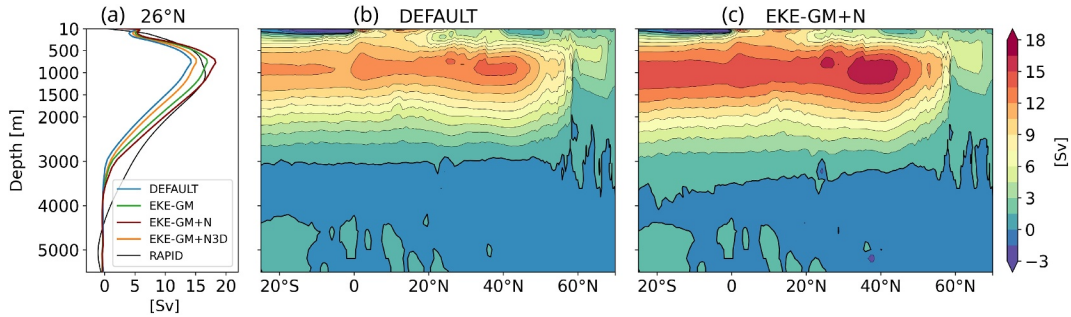

Figure 12. (a) Profile of the Atlantic meridional overturning streamfunction at 26°N in all four experiments, as well as the observational estimate from the RAPID monitoring database. Overturning streamfunction averaged over 1995–2017 in (b) the DEFAULT and (c) EKE-GM+N experiments.

DEFAULT. These anomalies in the density field hold from the surface to 1,000 m depth and are consistent with the increased NADW formation. Water-mass characteristics show an opposite effect of warmer and saltier waters in the Labrador Sea, with salinity dominating the impact on density. In the smaller and inner area, EKE-GM density anomalies are larger than in EKE-GM+N. However, the hierarchy changes when the density profiles are analyzed in larger areas. In the outer area, EKE-GM+N shows higher densities than EKE-GM down to 1,000 m depth. The western boundary density increase is consistent with the AMOC strengthening (Buckley & Marshall, 2016). In addition, the maximum depth of these positive density anomalies is consistent with maximum MLD patterns (Figure 13), EKE-GM+N having the deepest convection followed by EKE-GM and EKE-GM+N3D. In the latter experiment, positive density anomalies with respect to DEFAULT are also diagnosed. However, these anomalies were relatively smaller, which explains the weaker increase of the AMOC (Figure 7e).

Despite the long-established view of a strong link between convection in the Labrador Sea and the AMOC, observational studies based on the recent Overturning in the Subpolar North Atlantic Program (OSNAP) (Lozier et al., 2019) have shown that overturning in the Labrador Sea is less significant than that occurring further east. In

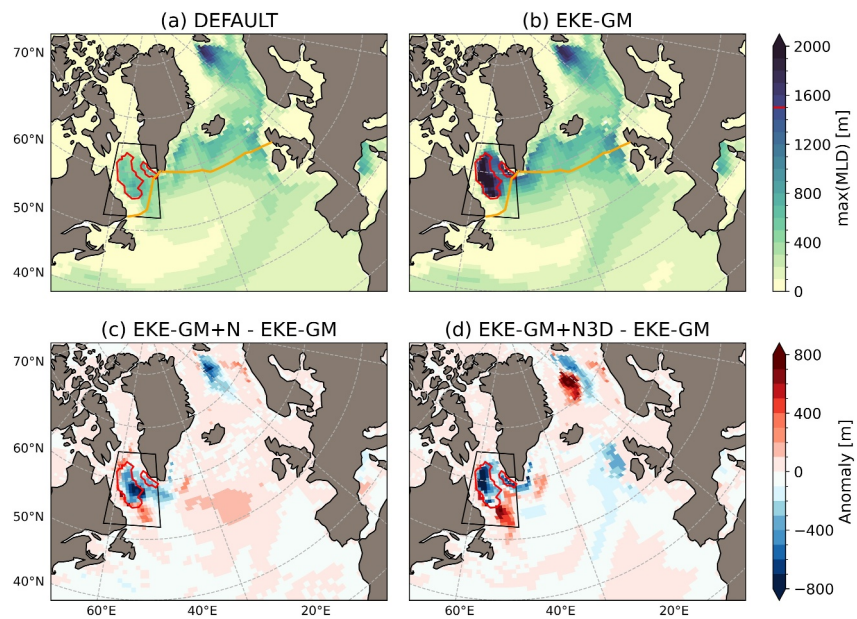

Figure 13. Maximum of the mixed layer depth (MLD) diagnosed for each year and averaged during the 1995–2017 period in (a) DEFAULT and (b) EKE-GM. The bottom panels show the anomaly with respect to EKE-GM for (c) EKE-GM+N and (d) EKE-GM+N3D. The red contours show the inner domain of the Labrador Sea where the annual maximum MLD is 1,500 m in EKE-GM, whereas the black box is referred to the outer domain and is defined by (62–46°W, 52–65°N). Orange lines in (a, b) indicates the Overturning in the Subpolar North Atlantic Program sections in which the overturning in the subpolar gyre is analyzed in Figure 15.

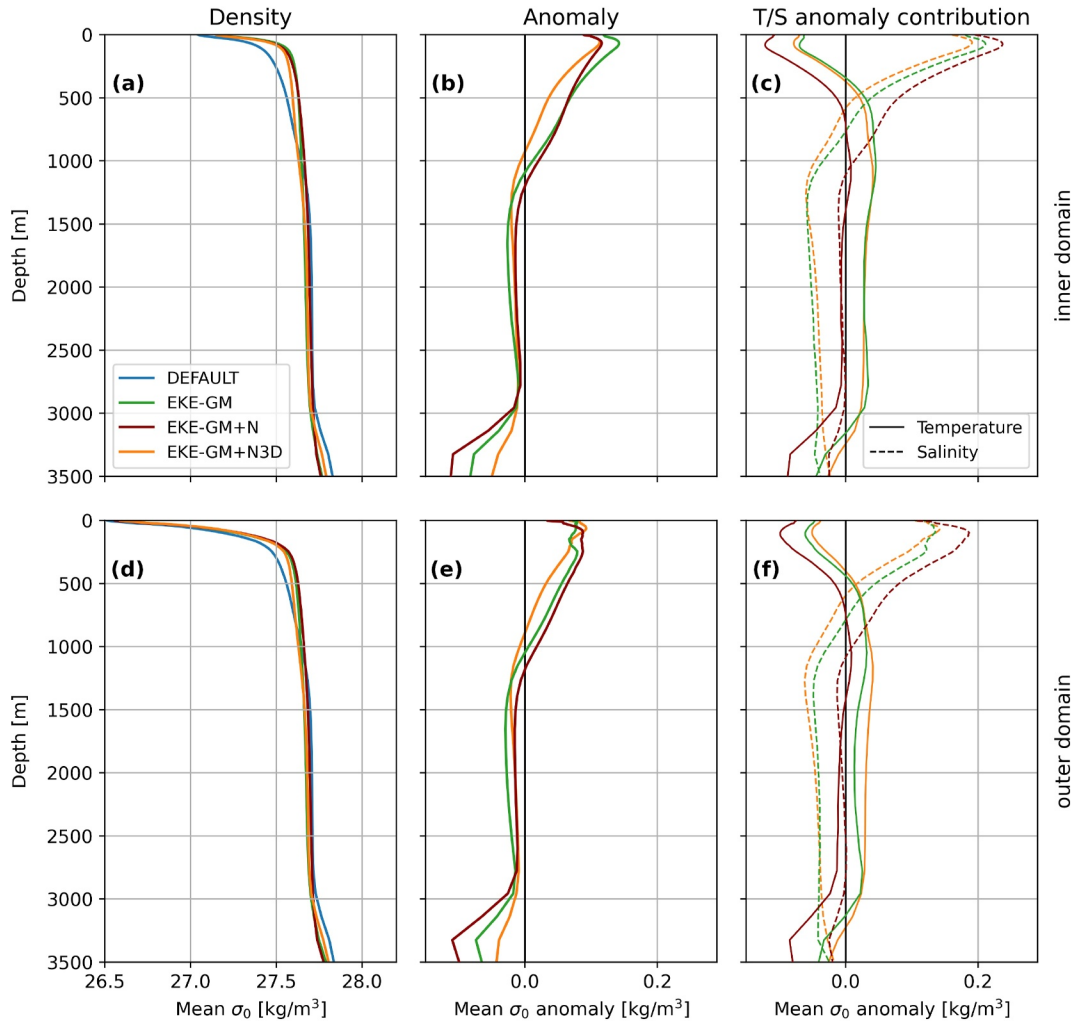

Figure 14. Averaged (a, d) density profiles in the Labrador Sea for all the experiments, (b, e) anomaly with respect to DEFAULT and (c, f) temperature and salt contributions to the computed density anomalies. Thermal and saline contributions are decomposed using the DEFAULT salinity and temperature, respectively. Profiles are time-averaged over the 1995–2017 period and are spatially averaged in (a–c) the inner or (d–f) outer domains defined in Figure 13.

order to verify the relative contribution to the AMOC of the western and eastern part of the North Atlantic subpolar gyre within our global ocean model, we compute the overturning stream function (in density space) through the two OSNAP sections (Figure 15). In all simulations, the overturning is dominated by the eastern subpolar gyre (across OSNAP-E) rather than the Labrador Sea (across OSNAP-W). These results closely align with the overturning derived from observations and climate models reported by Menary et al. (2020), as illustrated in their Figure 2. However, the overturning and transformations occur at lighter water masses in our model than in the observations. The energy-based parameterization does not alter the hierarchy between OSNAP-E and OSNAP-W, but it does increase the overturning across the two sections. The maximum of the mean (1995–2017) stream function in density space at OSNAP-E increases from 11.5 Sv in DEFAULT to 15.9 (+4.4) Sv, 16.4 (+4.9) Sv, and 14.3 (+2.8) Sv in EKE-GM, EKE-GM+N, and EKE-GM+N3D, respectively. The maximum of the stream function is found at higher density classes in EKE-GM and EKE-GM+N, likely due to an increase of surface buoyancy loss north to the OSNAP-E section. Perhaps the most noticeable change induced by the parameterization is found on the OSNAP-W section, where northward flowing waters are significantly denser up to 1,027.49 kg m^{-3} in EKE-GM and EKE-GM+N against 1,027.39 kg m^{-3} in DEFAULT. In addition to increasing the density of water masses, the parameterization also strengthens the overturning in the western part of the subpolar gyre. In EKE-GM, the maximum of the stream function is increased by +2 Sv, reaching 3.6 Sv, in comparison to 1.6 Sv in DEFAULT. This is most marked in EKE-GM+N (+3.1 Sv) and EKE-GM+N3D

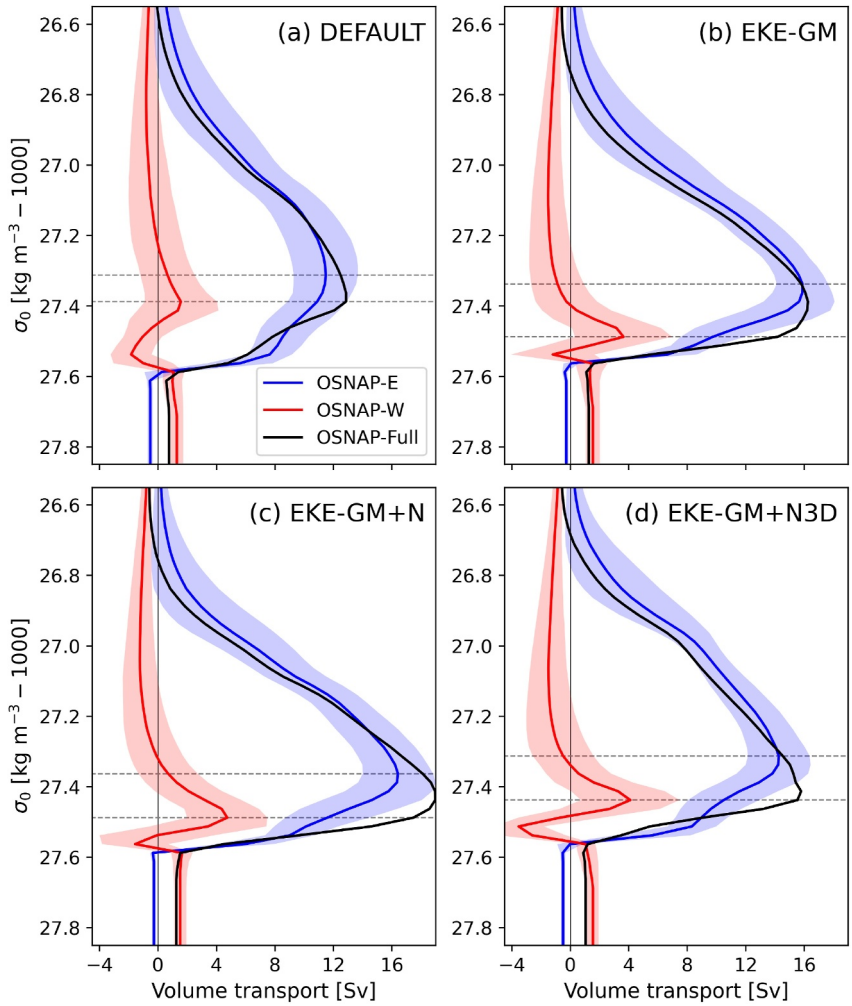

Figure 15. Overturning stream function in density space across the Overturning in the Subpolar North Atlantic Program sections in (a) DEFAULT, (b) EKE-GM, (c) EKE-GM+N, and (d) EKE-GM+N3D: blue is OSNAP-East, red is OSNAP-West, and black is the total. Solid lines are the time-mean (1995–2017) stream function, while light shading represents the monthly standard deviation computed over the same period. Horizontal dashed lines shows the densities where the maximum of the mean stream function is found for each simulation at OSNAP-E and OSNAP-W. The location of the OSNAP-E and OSNAP-W sections is given on the maps of Figure 13.

(+2.5 Sv), suggesting that κ_n can have a significant impact on the water mass transformations occurring in the Labrador Sea. Our findings therefore indicate that the energy-constrained mesoscale parameterizations alter the overturning in both the eastern and western parts of the North Atlantic, although their dynamics are likely connected.

Our results suggest changes in the North Atlantic subpolar dynamics, which in turn can alter the tracer distributions. Maps of currents averaged over the upper 500 m (Figure 16) clearly show how the parameterization influences the circulation. In DEFAULT, the North Atlantic Current avoids the Newfoundland Basin and flows continuously in the north-east direction. When comparing with the climatology of hydrographic observations, this leads to a large cold and fresh bias in the Newfoundland basin, a well-known feature of many coarse resolution ocean models (Tsujino et al., 2020). More generally, the bias is shared in most of the subpolar gyre, with the exception being the East Greenland Current where biases are relatively low due to warm and salty subtropical waters carried there. In addition, there is also a warm bias of approximately 1–2°C offshore of the North Atlantic Current, resulting in warmer waters in the eastern part of the North Atlantic. Activation of our parameterization for both κ_{gm} and κ_n significantly changes the behavior described above. In EKE-GM+N, after crossing the basin the North Atlantic Current is partially retroflected to the northwest, hence providing a shortcut through the

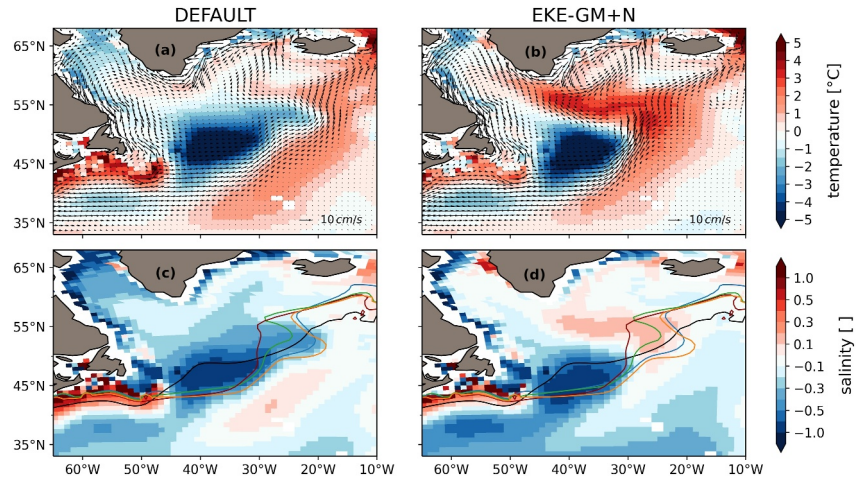

Figure 16. Temperature and salinity biases averaged over 0–500 m depth and over the 1995–2017 period in (a, c) DEFAULT and (b, d) EKE-GM+N. Observational references are from the World Ocean Atlas 2018 climatology (Garcia et al., 2019). In panels (a, b), arrows represent depth (0–500 m) averaged currents. In panels (c, d), contour lines show the depth-averaged 10°C line and help to visualize the North Atlantic Current front position in (blue) DEFAULT, (green) EKE-GM, (red) EKE-GM+N, (orange) EKE-GM+N3D, and (black) the climatology.

subpolar gyre which brings warm and salty waters to the Labrador and Irminger Seas. Though this change in the North Atlantic Current position does not fully reflect the region's dynamics, it leads to a significant reduction of salinity biases, especially in the Labrador Sea where saltier waters result in better agreement with the observations. In addition, the cold and fresh anomaly spot of the Newfoundland basin is reduced in size, without being eliminated since the North Atlantic Current is mostly unchanged west of 30°W. This leads to a positive temperature and salinity anomaly at the core of the subpolar gyre. Since the salinity contribution tends to dominate the density anomaly, this contributes to the overall increase of wintertime deep convection (as evidenced by the increase in maximum of MLD). We also note an intensification of the Irminger gyre which becomes closer to results obtained from higher resolution models (Deshayes & Frankignoul, 2008). Finally, comparing the experiments with each other clearly suggests the intensity of the AMOC is linked to the North Atlantic Current position east of the Newfoundland basin, with an earlier northward drift of the current meaning an intensified AMOC. We found that the increased overturning variability induced by the new energy-constrained mesoscale parameterizations, apparent in the AMOC timeseries (Figure 7e), is also correlated to time-varying shifts of the North Atlantic Current (not shown).

5. Summary and Conclusion

In this study, we present an energetically and observationally constrained mesoscale eddy parameterization, which defines the eddy coefficients involved in the tracer equation of coarse-resolution ocean models (typically 1° resolution). The parameterization employs a prognostic EKE budget in order to estimate the kinetic energy of the unresolved mesoscale variability. The present work extends the implementation of GEOMETRIC (Mak, Marshall, et al., 2022) by adapting the framework to the EKE (instead of the total eddy energy), while complementing the parameterization of the eddy energy budget. The subgrid EKE is then used to specify both the neutral diffusivity κ_n and the Gent and McWilliams (1990) coefficient κ_{gm}. Compared to previous parameterized EKE budgets, the proposed prognostic equation includes two sources of mesoscale kinetic energy representing energy fluxes from baroclinic and barotropic instability mechanisms. The sink of EKE is given by a single term following dimensional arguments inspired by the quasi-geostrophic turbulence and the Kolmogorov (1941a) energy cascade. This term shows good skills in reproducing the observed spatial patterns of EKE. The EKE budget has been calibrated within a global ocean model configuration to match an observation-based estimate of the EKE reservoir. Consequently, the method outlined in this work is able to constrain both mesoscale diffusivities indirectly by using a global observational EKE reconstruction. Furthermore, the present work provides valuable information on the sensitivity of the subgrid EKE field to the various parameters involved in its equation.

This could inform future calibration efforts using more systematic and automated methods (Hourdin et al., 2023; Williamson et al., 2017).

The impact of the new energetically constrained eddy coefficients has been evaluated using four hindcast simulations of the global ocean. The initial configuration, designated DEFAULT, is derived from the ocean and sea-ice components of the CNRM-CM6-1 climate model (Voldoire et al., 2019). Three sensitivity experiments were conducted, in which energetic and physical constraints were successively introduced to κ_{gm} and κ_n, with the objective of investigating the individual impact of the new ingredients. Our findings can be summarized as follows:

1. The energy-constrained κ_{gm} alters the ocean stratification in key regions of the Southern Ocean and the North Atlantic, which in turn produces important changes in large-scale circulation. These changes are predominantly caused by a reduction of κ_{gm} in these high latitude regions where the predicted EKE levels are low. Consequences include an intensification of the ACC of +21 Sv (or +20%) and an increase of 2.6 Sv (or +18%) of the AMOC at 26°N, relative to DEFAULT. The MHT is impacted mostly via changes in the large-scale circulation, with the exception of the Southern Ocean where the reduced eddy-induced overturning tends to dampen the anomalous heat transport.
2. The energy-constrained neutral diffusivity κ_n exerts a significant influence on SST and ocean heat content. The parameterization results in an increase of the diffusivity across the entire ocean, the exceptions being the highest latitudes. Consequently, the enhanced neutral diffusion along steep isopycnals effectively releases heat from intermediate waters, thereby contributing to a relative subsurface cooling and surface warming of the ocean. Furthermore, our findings indicate that κ_n exerts a moderate influence on the large-scale circulation. The changes in κ_n tend to accentuate the primary consequences of κ_{gm}. For instance, we diagnosed an increase of the AMOC index of +1.4 Sv from κ_n, relative to DEFAULT, in addition to +2.6 Sv induced by changes of κ_{gm}.
3. The use of the surface modes (LaCasce, 2017) as a vertical structure in our parameterization can alter the diffusivities in two ways. First, by modifying the equilibrated EKE field and second, by adding a vertical dependence to κ_n (κ_{gm} is held constant with depth in this study). In this work, the choice has been made to maintain the global equilibrated EKE constant across all experiments, with the objective of focusing on the role of the structure function assigned to κ_n. The vertical structure in κ_n essentially increases the isoneutral mixing in the top 1,000 m depth, thereby exacerbating the sea surface anomalies as well as the cooling in the ocean interior. As hypothesized by Holmes et al. (2022), increase in neutral diffusion in the Southern Ocean may also reduce the upper overturning cell, thus providing an explanation for the AMOC slowdown diagnosed when activating the vertical structure in EKE-GM+N3D compared to EKE-GM+N.

Our study also reveals an intense AMOC variability induced by the OMIP2 (Tsujino et al., 2018) protocol and its 61-year (1958–2018) repeated cycles. Similar to other ocean models, the meridional overturning circulation simulated in our numerical experiments increases continuously during the forcing period and peaks between 1995 and 2004 before slowing down to a value close to the initial state. Interestingly, the amplitude of this variability appears to be sensitive to our mesoscale parameterization. Our results show that this amplitude is related to the position of the North Atlantic Current between 45 and 55°N (Figure 16) and may be a contributing factor to the associated changes of ocean heat storage in the North Atlantic (Figure 9).

Given the computational limitations of integrating higher-resolution ocean models over time scales relevant for climate applications, the present methodology offers an effective solution for representing ocean mesoscale eddies and their underlying transport in climate and Earth system models. Indeed, the additional computational cost to solve the prognostic EKE budget is only about 1%. Yet the model captures with high fidelity the targeted EKE field derived from readily available observations. In particular, the observation-based vertically-integrated EKE exhibits a log-normal distribution across the majority of the ocean, a characteristic that our parameterization replicates. This log-normal distribution is also found for the dissipation of EKE, a feature expected from higher resolution studies (Pearson & Fox-Kemper, 2018). It should be noted, however, that the statistical description of the turbulence used in our approach is designed for representing the mean effect of the eddies, rather than the (interannual to decadal) variability of the eddy field.

Nevertheless, it should be acknowledged that the current implementation of the parameterization is not yet optimal and is open to further enhancement. First, the vertical structure of κ_{gm} and κ_n remains poorly constrained,

while it is known to exhibit variations with depth (Smith & Marshall, 2009; Groeskamp et al., 2020; Stanley et al., 2020; W. Zhang & Wolfe, 2022; Meunier et al., 2023). While no vertical structure has been implemented for the former, a static vertical structure can be set to κ_n. In this work, we have used the surface modes derived from observations (Torres et al., 2023). This approach has the disadvantage of preventing model-interactive feedbacks, resulting in inconsistency between the injected map and the simulated ocean stratification. Perhaps the most poorly constrained term in our parameterized EKE budget is the barotropic source term. This term is used to represent shear instability mechanisms and eddy-mean flow interactions. These interactions are indeed able to redistribute kinetic energy across scales, thereby accelerating and decelerating mean currents. Due to the inherent complexity of these interactions (Chen et al., 2014; Kang & Curchitser, 2015; Zanna et al., 2017), a simple positive-only parameterization based on a turbulent flux-gradient relation is selected. This choice indicates coherent energy fluxes, with a significant portion of the EKE being added to the Equatorial Current system and near WBCs (Figure 4b). However, this simple representation is not yet complete and may be refined at a later stage.

Finally, we emphasize that many ocean models still define κ_{gm} and κ_n separately or set $\kappa_{gm} = \kappa_n$, although it is known that they are related but in a non-trivial way (Smith & Marshall, 2009). In this work, we have related the two eddy coefficients through the same dynamical field allowing a physically constrained and consistent representation of unresolved mesoscale transports. However, it should be noted that such a representation could have significant implications when used in fully coupled ocean-atmosphere or Earth system models. Indeed, the new energy-constrained parameterization alters the sea surface temperature, which has the potential to produce significant changes in ocean surface fluxes and the meridional overturning circulation (Holmes et al., 2022). In turn, this could have consequences for sea ice, winds and clouds (Vogt et al., 2025). Additionally, the parameterization has notable impacts on stratification in the Southern Ocean and the North Atlantic subpolar gyre. Since these regions and their dynamics have an outsize role in anthropogenic carbon uptake, the parameterization could affect the global carbon budget as simulated by Earth system models. Last but not least, we deliberately focused on the averaged response of the ocean large-scale circulation and heat storage to changes in the mesoscale eddy diffusivities. However, further investigation is required to fully understand the temporal variability of the mesoscale transports induced by our interactive parameterization. Since the mesoscale kinetic energy is expected to vary on climatological timescales (Beech et al., 2022; Martinez-Moreno et al., 2020), this parameterization provides a means of evolving parameterized mesoscale transports with the changing ocean state.

Appendix A: Specifications of Mesoscale Diffusivities for Ocean Models Contributing to the OMIP2 Evaluation

This appendix provides a summary of the most common choices made when specifying the coefficients used to represent subgrid-scale transports of mesoscale eddies in the tracer equation of ocean climate models. In this section, we will be focusing on 11 model configurations (see Table A1) that participated in the Ocean Model Intercomparison Project 2 (OMIP2; Tsujino et al., 2020).

With the exception of GFDL-MOM (Adcroft et al., 2019), ocean grids have a horizontal resolution coarser than 0.5° and therefore employ parameterizations for the unresolved mesoscale transports of tracers. Specifically, they incorporate the effects of mesoscale eddies using the (Gent & McWilliams, 1990) eddy-induced circulation scheme and a laplacian diffusion operator rotated to act along isopycnals (Redi, 1982). Please note that implementation can either include both schemes independently or use the skew-flux formulation (Griffies, 1998). With regard to the GM coefficient, a frequently adopted approach is to use a stratification-dependent coefficient which varies in space and time following the buoyancy frequency (N^2). This approach was proposed by Ferreira et al. (2005) and allows for three-dimensional variations. NEMO-based ocean models typically scale the GM coefficient with the growth rate of an Eady wave (Eady, 1949) times a squared eddy length scale. This approach is guided by baroclinic instability theory and has been proposed by various authors, including Visbeck et al. (1997) and Treguier et al. (1997). The specification of the neutral diffusivity is generally set in a somewhat ad hoc manner. It is typically set equal to the GM coefficient, or to a constant, or else it follows the grid cell size.

Table A1
Details of the Mesoscale Parameterizations Employed in 11 Models Participating in the OMIP2 Intercomparison Exercise (Tsujino et al., 2020)

Model name	Ocean model	Res. (hor.; levels)	Eddy-induced adv.	Neutral dif.	$\kappa_n = \kappa_{gm}$	References
AWI-FESOM	FESOM v1.4	1°; 46(z)	Strat.; V(3D); <1,500	Strat.; V(3D); <1,500	True	Wang et al. (2014)
CAS-LICOM3	LICOM3	1°; 30(η)	Strat.; V(3D); 300–2,000	Const.; F; 300	False	Lin et al. (2020)
CESM-POP	POP2	1°; 60(z)	Strat.; V(3D); 300–3,000	Strat.; V(3D); 300–3,000	True	Danabasoglu et al. (2012)
CMCC-NEMO	NEMO v3.6	1°; 50(z)	Growth; V(2D); no info	Grid; V(2D); no info	False	Cherchi et al. (2019)
EC-Earth3	NEMO v3.6 (r9466)	1°; 75(z)	Growth; V(2D); <200	Grid; V(2D); <2,000	False	Tsujino et al. (2020), Madec et al. (2017)
FSU-HYCOM	HYCOM	0.72°; 41(*)	Const.; F; 1,000	Const.; F; 2,000	False	Chassignet et al. (2003)
GFDL-MOM	MOM6	0.25°; 75(*)	None	None	/	Adcroft et al. (2019), Held et al. (2019)
Kiel-NEMO	NEMO v3.6	0.5°; 46(z)	Growth; V(2D); <1,000	Growth; V(2D); 100–1,500	True	Tsujin et al. (2020), https://git.geomar.de/cmip6-omip/ (visited 28/02/2025)
MIROC-COCO	COCO v4.9	1°; 62(*)	Const.; F; 300	Const.; F; 1,000	False	Watanabe et al. (2010), Tatebe et al. (2019)
MRI-ESM2	MRI.COM v4	1°; 60(z)	Strat.; V(3D); 300–1,500	Const.; F; 1,500	False	Tsujino et al. (2020), Danabasoglu and Marshall (2007)
NorESM-BLOM	BLOM (MICOM)	1°; 51(ρ)	EKE; V(3D); no info	EKE; V(3D); no info	True	Seland et al. (2020)

Note. The ocean resolution indicates the nominal horizontal resolution, while most models use zonal grid refinement, specifically near the equator. Vertical levels and the corresponding coordinate system (z, η, ρ) or hybrid vertical coordinates (*) are also provided. With the exception of one model, all models parameterize the effects of mesoscale on tracers using an eddy-induced circulation (Eddy-induced adv.) and a lateral diffusion rotated along neutral surfaces (Neutral dif.). There are a number of options when it comes to specifying the eddy coefficients. They can be defined with the local stratification (Strat.) as outlined by Ferreira et al. (2005) or use a formulation based on the Eady growth rate (Growth) as proposed by Visbeck et al. (1997) and Treguier et al. (1997). Alternatively, they can be set to follow the horizontal grid size (Grid) or fixed to a constant (Const.). Finally, one model has energetically constrained coefficients (EKE) using the prognostic equation of Eden and Greatbatch (2008). V and F indicate if the coefficient is time and space variable or fixed, and when available ranges of the coefficients (in $m^2\ s^{-1}$) are given.

Appendix B: Derivation of the Parameterized Eddy Energy Budget

This appendix section details the derivation of the eddy kinetic energy (EKE) equation from the momentum equations applied to the ocean. Assumptions and turbulent closures leading to the final parameterized budget are also presented.

B1. Statistical Derivation of the Eddy Kinetic Energy Equation

The ocean dynamics is well approximated by the Navier-Stokes equations under the hydrostatic and Boussinesq hypotheses. In this primitive system, the horizontal momentum balance and the hydrostatic equilibrium equations are:

$$\frac{\partial \mathbf{u}_h}{\partial t} + (\mathbf{u}\cdot\nabla)\,\mathbf{u}_h = -f\mathbf{k}\times\mathbf{u}_h - \frac{1}{\rho_0}\nabla_h p + \nu\nabla^2\mathbf{u}_h + \mathbf{F}^u, \tag{B1}$$

$$\frac{\partial p}{\partial z} = -\rho g, \tag{B2}$$

where t is the time, $\mathbf{u}$ the velocity vector, p the pressure, ρ the sea water density, ρ_0 a constant reference density, ν the sea water kinematic viscosity, z the vertical coordinate in the direction of the upward unity vector (noted $\mathbf{k}$), g the gravitational acceleration and f the Coriolis parameter. In these equations, the index $_h$ refers to the horizontal component of any vector so that $\mathbf{u} = (\mathbf{u}_h, w)$ and $\nabla = \left(\nabla_h, \frac{\partial}{\partial z}\right)$. Here, the vector $\mathbf{F}^u$ represents some external momentum forcings at the boundaries.

However, the study of turbulence is usually performed using a statistical decomposition (Reynolds, 1895) where each flow field is separated into a mean and a turbulent component. For instance, the velocity decomposition yields to:

$$\mathbf{u} = \overline{\mathbf{u}} + \mathbf{u}' \tag{B3}$$

where the symbol $\overline{\ }$ refers to a statistical or ensemble average obtained from a set of realizations of the same flow experiment and $'$ to the fluctuation and so the deviation from this mean. Applied to a circulation model, the mean quantities are associated to the large-scale flow explicitly *solved* while the fluctuations are *unresolved* eddying or turbulent motions.

Within this statistical framework, our low-resolution NEMO model approximates the ocean dynamics by solving the Reynolds-Averaged Navier-Stokes equations. For the momentum, this corresponds to:

$$\frac{\partial \overline{\mathbf{u}}_h}{\partial t} + (\overline{\mathbf{u}} \cdot \nabla)\,\overline{\mathbf{u}}_h = -f\mathbf{k} \times \overline{\mathbf{u}}_h - \frac{1}{\rho_0}\nabla_h \bar{p} + \overline{\mathbf{F}^u} - \nabla \cdot \overline{\mathbf{u}'\mathbf{u}'_h}, \tag{B4}$$

$$\frac{\partial \bar{p}}{\partial z} = -\bar{\rho} g, \tag{B5}$$

Equation B5 is the averaged hydrostatic equilibrium equation and shows that the mean field keeps the hydrostatic property. Subtracting from Equation B2 leads to $\partial p'/\partial z = -\rho' g$ and so the eddy field is also hydrostatic. Equation B4 is the averaged horizontal momentum balance and is very similar to Equation B1 apart from the extra right-hand side term $\overline{\mathbf{u}'\mathbf{u}'_h}$. It originates from the averaging of the non-linear advective term and requires parameterizations in order to close the system. In our low-resolution NEMO model, this term includes the parameterizations of both the vertical and the mesoscale turbulence.

The equation for the EKE, $\mathrm{EKE} = \frac{1}{2}\left(\overline{u'^2} + \overline{v'^2}\right)$ is then obtained by substracting Equation B4 from Equation B1 and then averaging the dot product of the resulting equation with the horizontal eddy velocities $\mathbf{u}'_h$:

$$\begin{aligned}\frac{\partial \mathrm{EKE}}{\partial t} + (\overline{\mathbf{u}} \cdot \nabla)\,\mathrm{EKE} = &-\frac{1}{\rho_0}\nabla \cdot \overline{\mathbf{u}'p'} + \overline{w'b'} - \overline{\mathbf{u}'u'} \cdot \nabla \overline{u} - \overline{\mathbf{u}'v'} \cdot \nabla \overline{v} \\ &-\nabla \cdot \left(\overline{\mathbf{u}'\mathrm{EKE}}\right) + \overline{\mathbf{u}'_h \cdot \mathbf{F}'^u},\end{aligned} \tag{B6}$$

where $b' = -\frac{\rho'}{\rho_0} g$ is the buoyancy fluctuation. This decomposition is standard (von Storch et al., 2012) and requires the divergence-free and hydrostatic properties of the eddy flow to reveal the eddy vertical buoyancy flux $\overline{w'b'}$ liable to the baroclinic instability.

B2. Modeling the Eddy Kinetic Energy Budget

Integrating Equation B6 over the water column yields:

$$\begin{aligned}\underbrace{\frac{\partial}{\partial t}\int \mathrm{EKE}\, dz}_{\text{time rate}} + \underbrace{\int \nabla \cdot (\overline{\mathbf{u}}\mathrm{EKE}) dz}_{\text{mean flow advection}} = &-\underbrace{\int \nabla \cdot \left(\frac{1}{\rho_0}\overline{\mathbf{u}'p'} + \overline{\mathbf{u}'\mathrm{EKE}}\right) dz}_{\text{divergence of eddy energy fluxes}} + \underbrace{\int \overline{w'b'}\, dz}_{\text{EPE}\rightarrow\text{EKE}} \\ &\underbrace{-\int \overline{\mathbf{u}'u'} \cdot \nabla \overline{u}\, dz - \int \overline{\mathbf{u}'v'} \cdot \nabla \overline{v}\, dz}_{\text{MKE}\rightarrow\text{EKE}} + \underbrace{\int \overline{\mathbf{u}'_h \cdot \mathbf{F}'^u}\, dz}_{\text{forcings}},\end{aligned} \tag{B7}$$

Equation B7 still requires closures to express new correlation terms as a function of the large-scale and resolved quantities. Modeling closures and other approximations applied to get the final parameterized two-dimensional EKE budget (Equation 1) are listed below:

- **mean flow advection**: represents the EKE changes due to the total mean flow. No specific closures are required since it is explicit. However the total advection can be further decomposed into a horizontal and vertical component. Combined with the vertical integral, the latter reduces to the vertical fluxes at the top and bottom boundaries where the vertical velocities $\overline{w}$ are generally weak. The advection is therefore simplified:

$$\int \nabla \cdot (\overline{\mathbf{u}}\mathrm{EKE})\, dz \simeq \int \nabla_h \cdot (\overline{\mathbf{u}}_h \mathrm{EKE})\, dz$$

- **divergence of eddy energy fluxes**: is the transport of EKE done by eddy pressure work and eddying flow. As for the advection, each term is separated into a horizontal and vertical part. Assuming the horizontal transport is dominated by the eddy advection the term is parameterized (Equation 5) as an isotropic horizontal diffusion (Grooms, 2017):

$$\int \nabla_h \cdot \left(\frac{1}{\rho_0} \overline{\mathbf{u}'_h p'} + \overline{\mathbf{u}'_h \mathrm{EKE}} \right) dz \simeq \int \nabla_h \cdot \overline{\mathbf{u}'_h \mathrm{EKE}} dz \simeq \int \left[\nabla_h \cdot (\kappa_E \nabla_h \mathrm{EKE}) \right] dz$$

  where κ_E is the EKE diffusion coefficient. In this study, it is assumed to be constant in time and space.
- Similar to the mean advection, the depth-integrated vertical transport reduces to the vertical boundary fluxes acting as sources and/or sinks of EKE. However, these fluxes are not trivial to parameterize and are thus neglected in our energy budget.
- **EPE → EKE**: represents the energy conversion between eddy potential and EKE due to baroclinic instability. One can find the exact same term with opposite sign when deriving the equation for the EPE (Kang & Curchitser, 2015). Analyzing the EPE equation also reveals that $\overline{w'b'}$ is well balanced by the energy conversion from APE to EPE (von Storch et al., 2012). We therefore use the latter and a flux-gradient relation to parameterize the energy flux due to the baroclinic instability (Equation 2):

$$\int \overline{w'b'}\, dz = \int -\frac{g}{\rho_0 N^2} \overline{\rho' \mathbf{u}'_h} \cdot \nabla_h \overline{b}\, dz \simeq \int \kappa_{gm} \frac{\nabla_h \overline{b} \cdot \nabla_h \overline{b}}{N^2} dz \simeq \int \kappa_{gm} \frac{M^4}{N^2} dz$$

  where we retain κ_{gm} as a relevant eddy buoyancy diffusivity.
- **MKE → EKE**: represents the energy conversion between mean and EKE and can be a proxy for the barotropic instability. Is composed of horizontal and vertical components which produce stress due to horizontal and vertical shear, respectively. However we consider only the horizontal part (Equation 3) since it is assumed to be the dominant one in WBCs (Tedesco et al., 2019) and near the equator (Marchesiello et al., 2011):

$$-\int \overline{\mathbf{u}' u'} \cdot \nabla \overline{u}\, dz - \int \overline{\mathbf{u}' v'} \cdot \nabla \overline{v}\, dz \simeq \int \kappa_u |\nabla_h \overline{\mathbf{u}}_h|^2\, dz$$

  where κ_u is the eddy diffusivity for the momentum. It is worth noting that, for positive values of κ_u, the modeled energy flux will be only a source for the EKE reservoir. While this is true at the global scale, previous studies have shown it could be positive or negative locally (von Storch et al., 2012; Tedesco et al., 2019).
- **Forcings**: they represent the EKE generation and/or dissipation mechanisms by work done from different sources and interactions (e.g., eddy-fluctuating wind interactions, internal waves). Together with the remaining vertical transport by pressure work and eddy velocity, they can be either a source or a sink for the EKE. However, our parameterized budget assumes that sources are dominated by the baroclinic and barotropic instabilities while the other processes (e.g., bottom drag, wind "eddy-killing" effect, interactions with other scales) are responsible for the dissipation of EKE.

  The Kolmogorov theory (Kolmogorov, 1941b) provides a means of describing the kinetic energy spectrum for three-dimensional isotropic turbulent flows. The theory assumes the existence of an intermediate range of scales between the large forcing scale and the smallest dissipation scale. This intermediate range is dominated by inertial terms and is therefore referred to as the *inertial range*. In order for this spectrum to achieve a steady

state, the rate of energy input at the forcing scale must be equal to the energy flux cascading to smaller scales through the inertial range, as well as equal to the dissipation rate, which occurs at the smallest scales. This "locality hypothesis" is a key assumption of the inertial range theory, whereby the dissipation rate can be determined from the energy-containing range, rather than the dissipative scales (Kolmogorov, 1941a). From dimensional arguments, the dissipation rate can be formulated as:

$$D_e \simeq \int \frac{C_\epsilon}{L_\epsilon} \mathrm{EKE}^{3/2}\, dz$$

where L_ϵ is the dissipation length scale. In the two-dimensional turbulence theory, the kinetic energy is supposed to cascade from smaller to larger scales (Fjørtoft, 1953; Vallis, 2017), L_ϵ is related to the energy-injecting scale and is thus set to the local Rossby radius R_d and so $L_\epsilon = \frac{\int N\, dz}{2f}$.

Appendix C: Sensitivity of the ACC and AMOC Transports to κ_{gm} Reduction

In Section 4, it was evident that both the ACC and the AMOC transports increased in response to κ_{gm} (and to a lesser extent to κ_n) changes induced by the new energy-constrained parameterization (Figures 7e and 7f). It is not yet clear whether the overall amplitude of κ_{gm} or its new horizontal distribution is responsible for this. In particular, the ACC and the AMOC are known to be sensitive to changes in subpolar regions. At these latitudes, the new energy-based and observationally constrained κ_{gm} is reduced overall. Here, we examine the impact of reducing the GM coefficient in the DEFAULT configuration (without the energy formulation or observational constraints) on the large-scale circulation. To this end, we conducted two sensitivity tests based on the DEFAULT simulation in which κ_{gm} has been reduced. In the first instance, we reduce the upper limit of κ_{gm} down to 150 $m^2\ s^{-1}$ (instead of 1,000 $m^2\ s^{-1}$ in DEFAULT), which therefore removes horizontal variations at mid latitudes (Figure C1b). For the second test, we scale the DEFAULT coefficient by multiplying its formula by a factor of 0.4. Figure C1 illustrates the coefficient distribution resulting from both tests.

Both configurations with the reduced GM are run from the same ocean state (using the spin-up defined in Section 2.3.2) for one OMIP2 cycle. The results in terms of ACC and AMOC transports are plotted in Figure C2. The similarity between EKE-GM and the new experiments (and the fact that κ_{gm} is similar in high latitude regions) seems to indicate that indeed these circulation metrics are mostly affected by the GM parameterization in those regions. This finding indicates that the overall amplitude of κ_{gm} at subpolar latitudes plays a more significant role than its spatial distribution. However, we would like to stress that the energy-based parameterization remains the preferred option since it naturally produces a horizontal distribution that can be constrained by indirect observations, thus avoiding the need to tune it at every ocean cell. Indeed, under a future scenario with changing forcing, the amplitude of κ_{gm} could change depending on the specification, thus impacting on the ocean circulation.

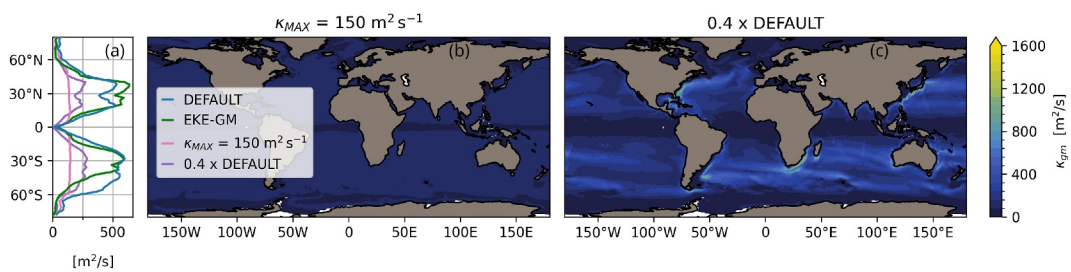

Figure C1. Spatial distribution of κ_{gm} in the two experiments with reduced GM from the DEFAULT configuration: (b) by limiting the upper value to 150 $m^2\ s^{-1}$ and (c) by rescaling the coefficient with a factor of 0.4. Zonal means are shown for comparison with DEFAULT and EKE-GM in (a). Note the similarity with EKE-GM in the high-latitude regions.

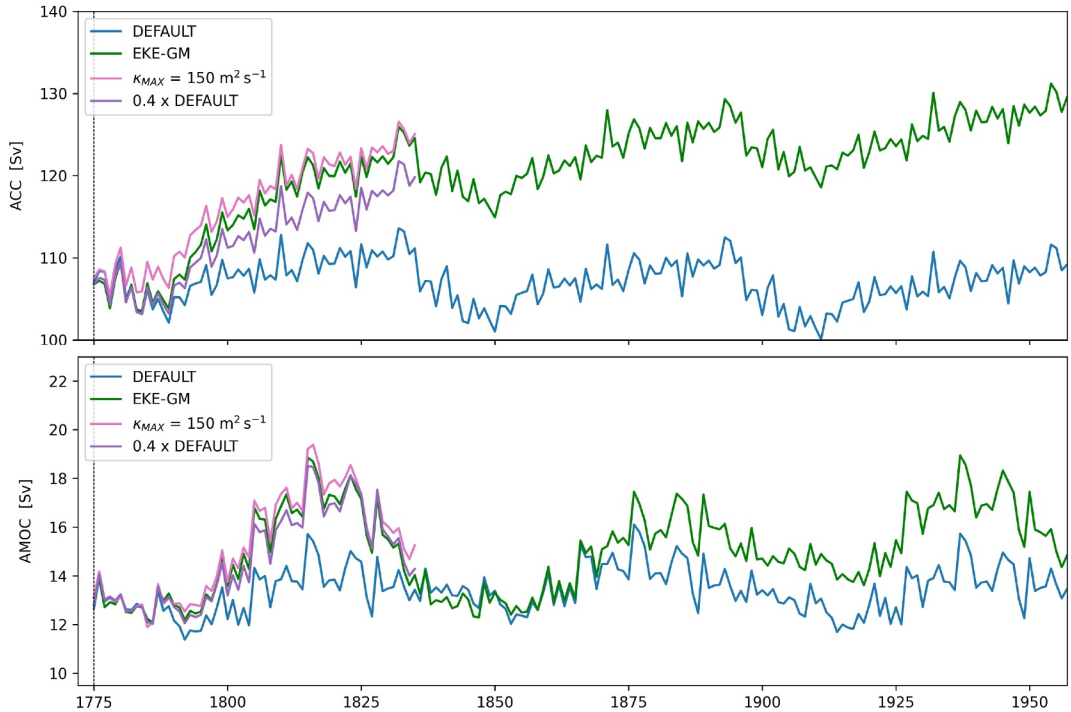

Figure C2. (top) Antarctic Circumpolar Current transport diagnosed online at the Drake Passage and (bottom) Atlantic Meridional Overturning Circulation maximum transport taken at 26^{o}N for the DEFAULT and EKE-GM configurations as well as the two new experiments with reduced κ_{gm}. Distribution of κ_{gm} for these experiments is given in Figure C1.

Appendix D: Developments of the Subgrid EKE Budget

In this work, we start with the NEMO v3.6 implementation of GEOMETRIC (Mak et al., 2018) which solves a prognostic equation for the depth-integrated eddy (potential plus kinetic) energy E and then redefines the (Gent & McWilliams, 1990) coefficient κ_{gm} accordingly:

$$\underbrace{\frac{\partial}{\partial t}\int \mathrm{E}\,dz}_{\text{temporal variation}} + \underbrace{\nabla_h \cdot \left[\left(\widetilde{\mathbf{u}}_h^z - |c|\mathbf{e}_x\right)\int \mathrm{E}\,dz\right]}_{\text{advection}} = \underbrace{\int \kappa_{gm}\frac{M^4}{N^2}\,dz}_{\text{production}} - \underbrace{\lambda\int(\mathrm{E}-\mathrm{E}_{\min})\,dz}_{\text{dissipation}} + \underbrace{\kappa_E\nabla_h^2\int \mathrm{E}\,dz}_{\text{diffusive transport}}, \tag{D1}$$

where $\widetilde{\mathbf{u}}_h^z$ is the horizontal depth-averaged flow, $|c|$ the long Rossby wave phase speed, λ the eddy energy dissipation timescale (in s^{-1}), $\mathrm{E}_{\min}$ a constant minimum background energy level, and $\kappa_{gm} = \alpha_{geom}\frac{\int \mathrm{E}\,dz}{\int (M^2/N)\,dz}$.

Implementation details regarding GEOMETRIC have been already described in Mak, Marshall, et al. (2022). New developments have been introduced to improve the representation of the eddy energy budget as well as to redefine the neutral diffusivity κ_n with the eddy energy (see our Equation 7). A portion of the code presented here has been incorporated into the version 4.2 of NEMO, while the remainder is scheduled for incorporation into subsequent releases of NEMO v5.

Main differences in the new energy budget and implementation details:

- **Eddy energy type:** the first difference arises from the choice of eddy energy type, and whether the energy budget refers to the total eddy energy E, as in GEOMETRIC, or to the EKE as in this work. This may initially appear to be misleading, due to the similarities between Equations 1 and D1. However, the only assumption related to the total eddy energy lies in the parameter α_{geom} introduced by D. P. Marshall et al. (2012), which is

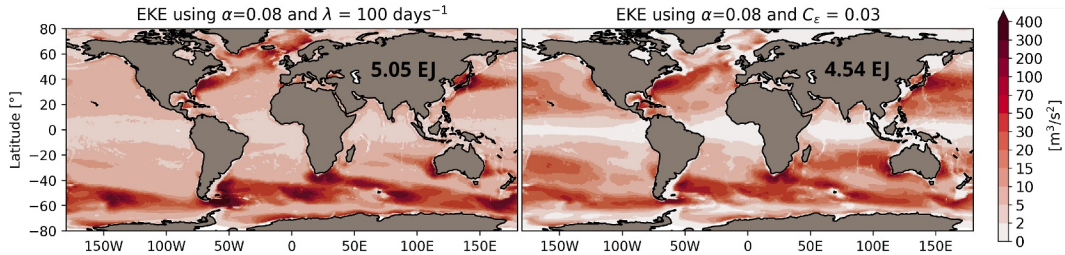

Figure D1. Global eddy kinetic energy (EKE) equilibrium using a linear damping dissipation term as in Mak, Marshall, et al. (2022) (left) and a formulation based on dimensional arguments as in this study (right). Both simulations use an eddy efficiency parameter of $\alpha = 0.08$ and have reached a similar global domain-integrated EKE.

theoretically bounded by unity. Nevertheless, switching to the EKE has been demonstrated to be an accurate model for eddy buoyancy fluxes (Bachman et al., 2017). However, we would like to emphasize that, despite the similarities, this conceptual difference have significant implications. In particular, α and α_{geom} are different parameters and subgrid eddy energy comparisons are not directly comparable. Finally, given that the EKE is better constrained by observations, and is directly related to the neutral diffusivity κ_n through the mixing length theory (Equation 7), it is a natural choice for the new parameterization.

- **The dissipation term:** a significant distinction can be attributed to the formulation of the dissipative term. GEOMETRIC employs linear eddy dissipation timescales (Cessi, 2008; D. P. Marshall & Adcroft, 2010; Mak et al., 2018), resulting in the formulation of the eddy dissipation through linear damping at a rate λ. Furthermore, the energy background $E_{\min}$ is introduced, enabling a minimum energy level across the global ocean. In this work, we have retained a formulation based on dimensional arguments:

$$\frac{C_\varepsilon}{R_d}\int \mathrm{EKE}^{3/2}\,dz, \tag{D2}$$

Figure D1 compares the two formulations and assesses the impact of the dissipation on the resulting EKE map. The new formulation (Equation D2), requires an eddy dissipation scale to be defined. Our parameterization uses the Rossby deformation radius expressed as $R_d = 0.4\frac{\int N dz}{f}$, where f is the Coriolis parameter and N is the Brunt-Väisälä frequency. Note that the vertical integral of N is already computed at each time step for the baroclinic source term B_C. The value of 0.4 has been selected in order to ensure consistency with the computed Rossby radius in other NEMO routines. However, it should be noted that this value has been replaced by 0.5 in NEMO v4. Moreover, the dissipation length scale is bounded between 2 and 40 km.

- **Two-dimensional transport:** in order to be applied to the depth-integrated eddy energy directly, both the advection and the diffusive transport terms employ mathematical approximations in GEOMETRIC. The advection trend uses a first-order upstream scheme while the diffusive trend is coded as Laplacian diffusion with a constant coefficient set by κ_E. The terms are given (in the NEMO notation) by:

$$\mathrm{adv} = \frac{1}{e_{1t}e_{2t}}\left(\delta_i\left[e_{2u}h_u u_{\mathrm{adv}}\left(\frac{\int \mathrm{EKE}dz}{h_t}\right)\right] + \delta_j\left[e_{1v}h_v v_{\mathrm{adv}}\left(\frac{\int \mathrm{EKE}dz}{h_t}\right)\right]\right), \tag{D3}$$

$$T_e = \frac{1}{e_{1t}e_{2t}}\left(\delta_i\left[\kappa_n\frac{e_{2u}}{e_{1u}}h_u\,\delta_i\left[\frac{\int \mathrm{EKE}dz}{h_t}\right]\right] + \delta_j\left[\kappa_n\frac{e_{1v}}{e_{2v}}h_v\,\delta_j\left[\frac{\int \mathrm{EKE}dz}{h_t}\right]\right]\right). \tag{D4}$$

where $\int \mathrm{EKE}dz$ is the transported quantity, e_1 and e_2 refer to the horizontal grid scale factors, h is the ocean depth, u_{adv} and v_{adv} are the horizontal depth-averaged velocities, and δ_i and δ_j stand for the numerical differencing operator in the zonal and meridional directions. The subscripts u, v and t refers to the grid points arrangement following the NEMO discretization methods (Madec et al., 2017).

In contrast, the proposed energy budget of this work (Equation 1) uses vertical integral terms accounting for the transport over the whole water column. Note that without vertical structure, both formulations gives comparable results (Figure D2).

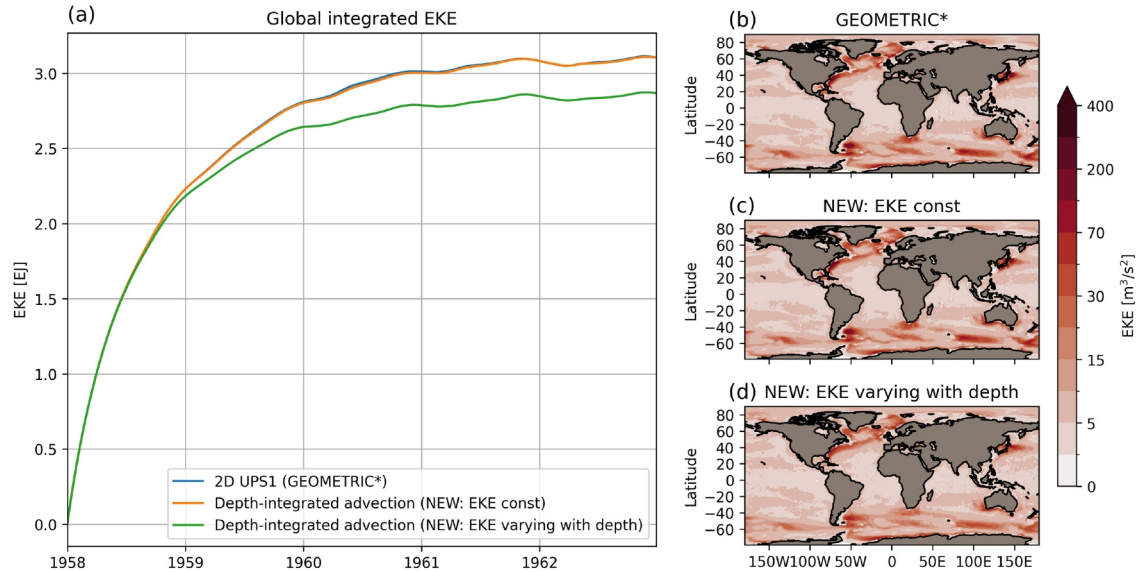

Figure D2. Impact of the advective scheme on the equilibrated eddy kinetic energy (EKE). Time series show the evolution of the globally integrated EKE during the initial years of the spin-up (a) for three distinct advection schemes: a 2D upstream scheme utilizing horizontal depth-averaged velocities and the new integrated transport with and without vertical variations of EKE. The right-hand panel maps illustrate the resulting depth-integrated EKE field, averaged over the last 2 years and for the following cases: the 2D advection (b), the new integrated transport without vertical variation of EKE (c) and the new integrated transport with vertical variation of EKE (d). Note that the 2D upstream scheme has been recently introduced and documented in the corrigendum of Mak, Marshall, et al. (2022).

- **Westward propagation:** the westward propagation of sea surface height anomalies has been observed from the merging of several operating altimeters and is ubiquitous in the world ocean (Ducet et al., 2000). Some exceptions are found, mostly in the strong eastward ACC (Hughes et al., 1998), the Gulf Stream and at the confluence of the Kuroshio and Oyashio Currents (Fu, 2009). However, the observed westward propagation speed is generally well approximated by linear Rossby wave phase speeds (Chelton et al., 2011). Consequently, GEOMETRIC includes an advection scheme which is Doppler shifted by Rossby wave phase speed predicted by the classical theory (Klocker & Marshall, 2014; Mak, Marshall, et al., 2022). Nevertheless, the additional advection term results in minimal impacts on the EKE field and tends to moderately diminish the parameterization performance in reproducing the observed EKE (Figure D3). Consequently, this propagation is not incorporated into our final budget.
- **Barotropic sources:** compared to GEOMETRIC, an additional source term has been included to account for shear or barotropic instability, as defined by Equation 2. The value for the momentum diffusivity (κ_u) can either be constant in time and space, or be set proportional to the eddy viscosity used in the momentum equation of the NEMO ocean model. In the latter case, κ_u exhibits spatial variations, decreasing in the tropics. This development was initially prompted by the lack of eddy energy in the WBC systems, as predicted by the GEOMETRIC parameterization. In addition, this flux provides a means for connecting the mesoscale EKE with the resolved MKE. Given the potential importance of eddy-mean flow interaction in the ocean circulation, it was considered important to represent this energy flux.
- **Adding a vertical structure:** the parameterization enables the use of a vertical structure for the EKE (experiment EKE-GM+N3D). In that case, a three-dimensional static map of the structure function $\phi(x,y,z)$ is read in a netCDF file. Once loaded, the vertical modes are used to add a vertical dependence to the neutral diffusivity κ_n, using Equation 7. A vertical dependence can also be added to κ_{gm}. In this case, the relation $\kappa_{gm}(x,y,z,t) = \phi(x,y,z)^2\kappa_{gm}(x,y,t)$ is used where $\kappa_{gm}(x,y,t)$ is given by Equation 6. κ_{gm} thus decreases in depth at the same rate as the EKE, while maintaining constant value in the mixed layer. However, the use of the surface modes results in a vertical structure of κ_{gm} which is reduced at depths leading to extremely weak EKE levels (Figure D4). As κ_{gm} is directly involved in the main source term of the EKE budget (i.e., the baroclinic source term B_C, as shown in Equation 2), integration over the water column reduces this. Therefore, κ_{gm} is set constant in depth in all the configurations (DEFAULT, EKE-GM, EKE-GM+N and EKE-GM+N3D) used in this work.

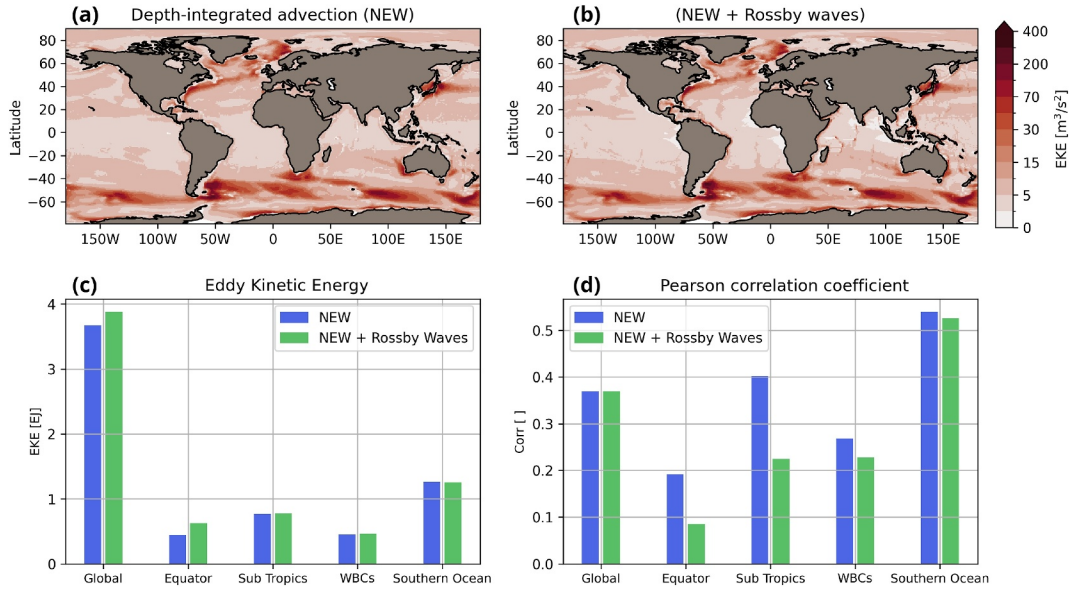

Figure D3. Impact of propagating the eddy kinetic energy (EKE) as a Rossby wave in Equation D1 on the equilibrated EKE. Top panel shows the resulting depth-integrated EKE field obtained from simulations without (a) and with the westward propagation (b). Both simulations employ the new integrated transport scheme for the advection by the mean flow. Bottom panel presents the performance of each simulation to reproduce the domain-integrated EKE (c) and spatial correlation (d) between parameterized and observation-based mesoscale eddy energy. Ocean domains are defined in Figure 3.

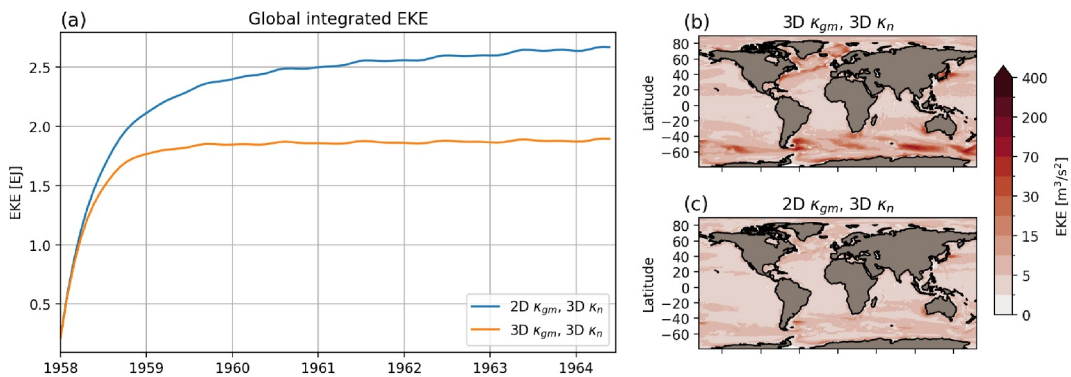

Figure D4. Impact of adding a vertical structure to κ_{gm} from prescribed surface modes. Time series show the evolution of the globally integrated eddy kinetic energy (EKE) during the initial years of the spin-up (a) for two simulations using a 2D-κ_{gm} an 3D-κ_{gm}. Both simulations employ a 3D neutral diffusion κ_n. The right-hand panel maps illustrate the resulting depth-integrated EKE field, averaged over the last 2 years and for the simulation using a 2D-κ_{gm} (b) and the one using a 3D-κ_{gm} (c).

Appendix E: Calibration of the EKE Budget

As mentioned in Section 2.3.1, we have decided to calibrate the parameterization by tuning the EKE budget (Equation 1), which includes four tunable parameters: the eddy momentum diffusivity κ_u, the dissipation coefficient C_ε, the eddy diffusion coefficient κ_E and the eddy baroclinic efficiency α through the formulation of κ_{gm}. However, the mixing efficiency Γ involved in the formulation of κ_n has been excluded since the neutral diffusion does not alter directly the equilibrated EKE.

An essential element of our calibration process is the utilization of data sets derived from global observations, which serve as our target. To do so, a global configuration with a realistic bathymetry is needed. Here, we have used the ocean and sea-ice component of the CNRM-CM6-1 climate model (Voldoire et al., 2019), in which the present eddy energy-constrained parameterization is implemented. Further details of the configuration can be

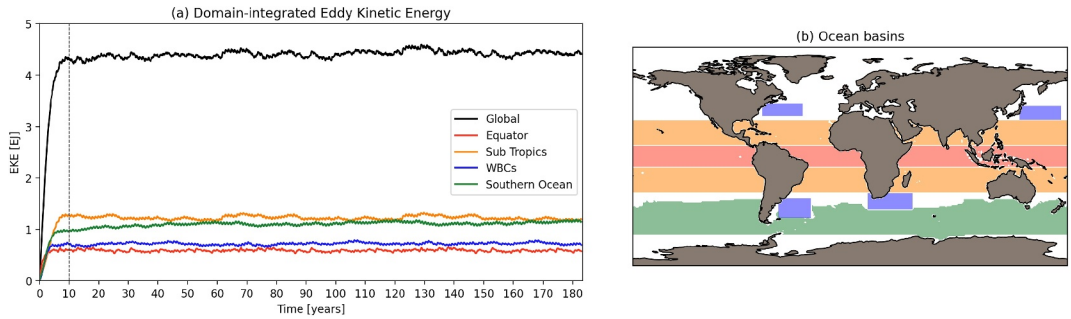

Figure E1. Spin-up of the depth-integrated eddy kinetic energy (a) in EKE-GM+N for the global ocean and four ocean domains (b). Ocean domains are the same than ones defined in Figure 3d.

found in Section 2. The depth-integrated EKE field is initialized by following the bathymetry to ensure a constant value throughout the ocean. This is done by setting the small value of $10^{-6}h$ (in $m^3\ s^{-2}$) to each cell, where h denotes for the depth of the water column. The model is then forced by the Japanese 55-year atmospheric reanalysis for driving ocean models (JRA55-do v1.5.0; Tsujino et al., 2018) and run for the first years until the EKE budget reaches a quasi-equilibrium. In most of our experiments, the equilibrium state is reached after a few years of spin-up (not shown) and, for our calibration, we have chosen to run the model for the first 15 years, from 1958 to 1973. In addition, the variations in global-integrated EKE over the entire forcing period are minor (see Figure E1). Therefore, the choice of the 15-year period is not considered crucial and does not affect the calibration.

The method consists in manually varying the four parameters (κ_u, C_ϵ, κ_E and α) and running the model for 15 years. All parameters are treated, and their values are therefore constant throughout the entire ocean (refer to Table E1 for details of the parameter space tested). Note that we have attempted to incorporate horizontal variations for κ_u. However, as this parameter is still subject to research, its spatial variations have not been included in our final configuration, in the interest of simplicity. A total of 80 simulations have been conducted, and the performance of each simulation has been assessed by comparing the simulated EKE field averaged over the last 2 years (1,971–1973), to the observation-based estimate of Torres et al. (2023). Note that this observation-based reference is derived from time-averaged surface currents plus a climatology of hydrographic measurements and therefore it had no temporal dimension.

Three distinct metrics are used to compare the mesoscale energy maps:

1. the domain integrated EKE (in J) which is computed from the depth-integrated EKE and the mesh grid of each product following:

$$I = \iint \left(\int \mathrm{EKE}\, dz \right) dx\, dy$$

2. the Wasserstein distance, which compares two probability distributions:

$$W = \int_{-\infty}^{\infty} |P_X(x) - Q_X(x)|\, dx$$

where P_X and Q_X are the cumulative distribution functions for the parameterized and the observation-based depth-integrated EKE fields, respectively. These functions represent the probability that a water column randomly selected in one of the data set, contains EKE levels less than or equal to x. In other words, $P_X(x) = p(X \leq x)$ with X the depth-integrated EKE and p the probability function (same for Q_X). Note that, since the EKE shows a quasi-lognormal distribution (see Figure 3), we have used the logarithm of the EKE for computing the distributions. The Wasserstein distance is a measure of the minimal work required to move a probability mass of one distribution (here the one given by the model) in order to retrieve the distribution of the

Table E1
List of the Parameters Involved in the Mesoscale Parameterization

Parameters	EKE sensitivity	Tested ranges	Expected ranges	References
α (–)	H	0.01–0.15	0.04–0.4	Bachman et al. (2017), Poulsen et al. (2019), Wei et al. (2022)
Γ (–)	L	0.35	0.1–0.5	Abernathey et al. (2022)
λ^{-1} (days)	H	60–150⋆	30–360	Mak, Avdis, et al. (2022)
C_ε (–)	H	0.001–0.1		
κ_E (m^2 s^{-1})	L	0–2,000		
κ_u (m^2 s^{-1})	M	500–5,000⋆	100–10,000	Q. Li et al. (2018)

Note. The sensitivity of the equilibrated eddy kinetic energy (EKE) field to each parameter is categorized as low (L), medium (M), or high (H). The minimal and maximal values tested during our calibration are given. The ⋆ symbol refers to parameters that have been tested with spatial variation (the min/max values are therefore given for the constant values). When available, the expected range set from the literature is indicated and can be used as an initial searching range. Note that the expected values for the eddy diffusivity κ_u involved in the baroclinic production term are taken from knowledge about mesoscale lateral viscosity, as this applies to horizontal momentum. Moreover, only one value for Γ has been tested, since its influence on the equilibrated EKE is negligible.

reference (the one derived from observation-based products). See the review of Panaretos and Zemel (2019) for a description of the main concepts involved in the Wasserstein distance, as well as the study of Ramdas et al. (2015) for the equivalence between the traditional Wasserstein distance and the one used here, based on cumulative distribution functions.

3. The spatial correlation coefficients of Pearson. To do this, the observation-based data set is first regridded onto the model mesh. Pointwise correlations are then computed and used to compare our simulations. Note that our observational-based reference contains some kinetic energy variability that is not due to mesoscale turbulence since it is uses sea surface height anomalies from altimetry records. This is particularly true in the equatorial band, where observed patterns reflect tropical instability waves. As our global configuration uses a grid refined in the tropics, the model is able to resolve these TIWs to some extent. In order to make a more accurate comparison with the observation-based EKE, correlation coefficients are computed on the total (parameterized + resolved) EKE. The parameterized EKE is the prognostic subgrid EKE, and the resolved EKE is computed using the fluctuating horizontal velocity (after removing the time-mean horizontal velocity). In practice, this has an impact on the metric only in the tropics.

Each of these metrics is computed both globally and in four ocean domains defined in Figure 3. In order to test the sensitivity of the EKE budget to each parameter (κ_u, C_ε, κ_E and α), their are first manually varied independently. Value ranges and sensitivity of the EKE fields evaluated with the previously described metrics are reported in Table E1.

E1. Sensitivity of the Depth-Integrated EKE

Main results from our sensitivity tests can be summarized as follow:

- The EKE diffusivity κ_E has a negligible impact on the resulting domain-integrated EKE (Figure E2). It is noteworthy that κ_E has also a negligeable effect on the EKE distribution (Figure E3), no matter the region selected for the evaluation. Consequently, we keep the GEOMETRIC value of 500 m^2 s^{-1} as in Mak, Marshall, et al. (2022)
- The momentum diffusivity κ_u, which controls the barotropic EKE production, is dominant in the equatorial band due to the high shear of the Equatorial Current system (Figure E4). However, it has a more moderate influence over the other regions, where it mostly provides energy input at the ocean western boundaries (Figure 4b). Consequently, we set $\kappa_u = 1500$ m^2 s^{-1} in order to match the reference domain-integrated energy in the equatorial region.
- The eddy efficiency α (Equation 6) and the dissipation coefficient (λ in Equation D1 or C_ε in Equation 1) have the most significant impact on the EKE budget. As expected, increasing the eddy efficiency leads to an up-tick in the diagnosed global EKE, while increasing the dissipation coefficient tends to reduce the level of EKE (Figure E5).

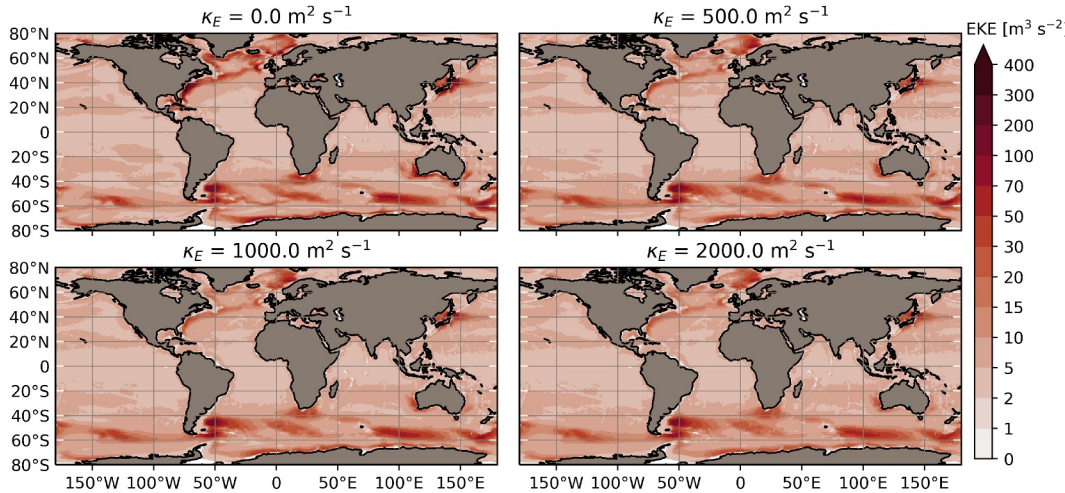

Figure E2. Impact of varying the eddy kinetic energy (EKE) diffusion coefficient κ_E on the EKE map after 10 years of spin-up. With the exception of the North Atlantic subpolar gyre and a small number of localized areas, our results indicate a negligible impact of the parameter κ_E on the eddy energy. It should be noted that these tests are run using a linear damping dissipation.

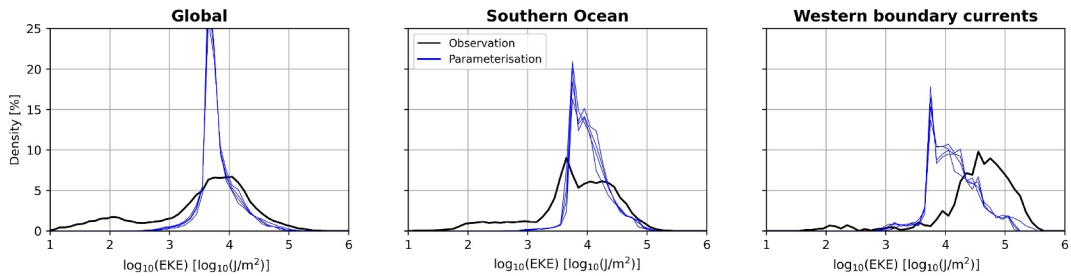

Figure E3. Impact of varying eddy kinetic energy (EKE) diffusion coefficient on the distribution of EKE after 10 years of spin-up. Distributions are computed on log-scale. The reference is plotted in black and the four simulations presented in Figure E2 are plotted in blues and show very similar distributions.

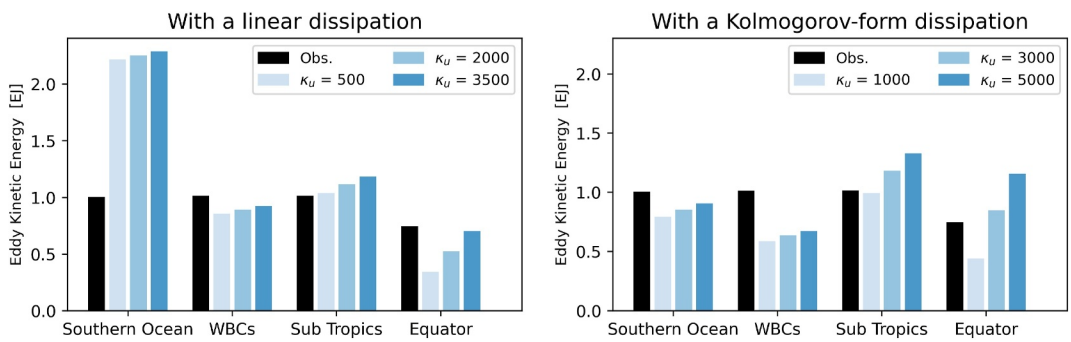

Figure E4. Impact of varying the barotropic coefficient κ_u on the domain-integrated eddy kinetic energy after 10 years of spin-up with the dissipation term defined as (left) a linear damping and (right) using the formulation based on dimensional analysis. Note the marked influence in the equatorial region.

E2. Adjusting the EKE Levels

A comparison of the domain-integrated EKE and the ratio "eddy efficiency/dissipation coefficient" (Figure E5) reveals strong similarities between the two, indicating that this ratio is indeed the primary factor for adjusting the domain-integrated EKE. This result has important implications for the representation of the mesoscale transports

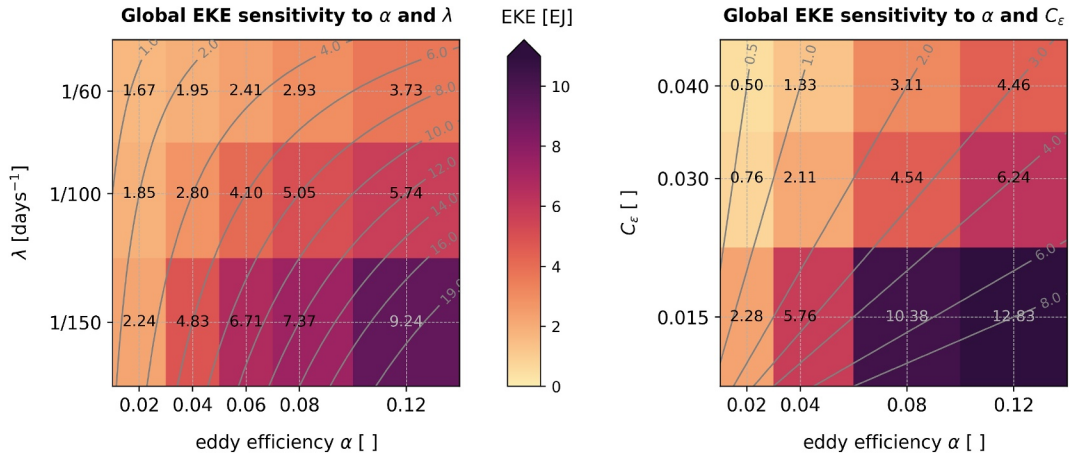

Figure E5. Global domain-integrated eddy kinetic energy (EKE) as a function of the eddy efficiency α and the dissipation coefficient (left) λ in days^{-1} or (right) C_ε. The gray lines represent the ratio "eddy efficiency/dissipation coefficient" which, to first order, drives the global equilibrated EKE. Note that the relationship between the equilibrated EKE, α and λ (or C_ε) is not linear. For instance, the sensitivity of the eddy energy to α is reduced when increasing the dissipation.

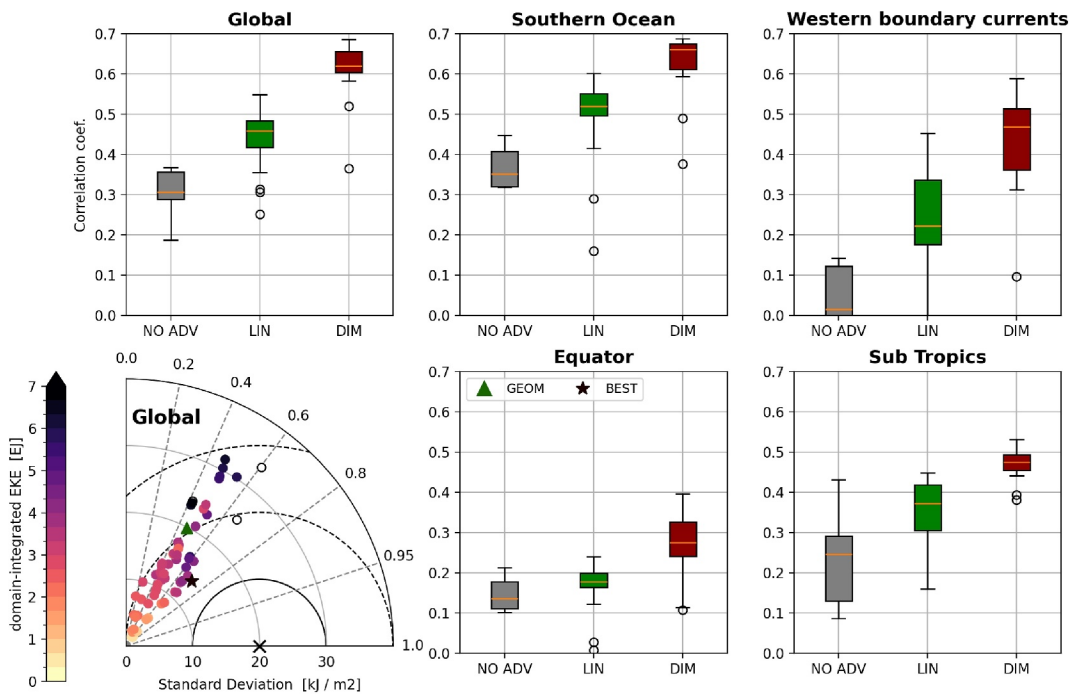

Figure E6. Box plots summarizing the spatial correlations between the simulations and the reference energy map. The Taylor diagram (lower left) includes three metrics: standard deviation, root mean squared error and Pearson correlation coefficients. Each simulation is colored as function of the global-integrated eddy kinetic energy (EKE) averaged over the last 2 years of the simulation. White empty circles indicate outliers; in the Taylor diagram, they are defined as simulations for which the domain-integrated EKE is greater than the maximum of the colorbar (7 EJ). The cross × symbol represents the observational pattern and is mapped in Figure 2. The original implementation of the advective term contains some bug in GEOMETRIC, resulting in negligible trend. Simulations employing the old implementation (gray) are therefore referred to as NO ADV. Once corrected, the EKE representation is significantly improved and are named LIN if using the linear dissipation formulation (green) or DIM if using the dimensional formulation based on dimensional analysis as in this work (red). To give a comparison, the default set of parameters of GEOMETRIC (Mak et al., 2018) with the new advective scheme and the best-estimate resulting from the calibration process of this work are shown in green triangle and star symbols, respectively.

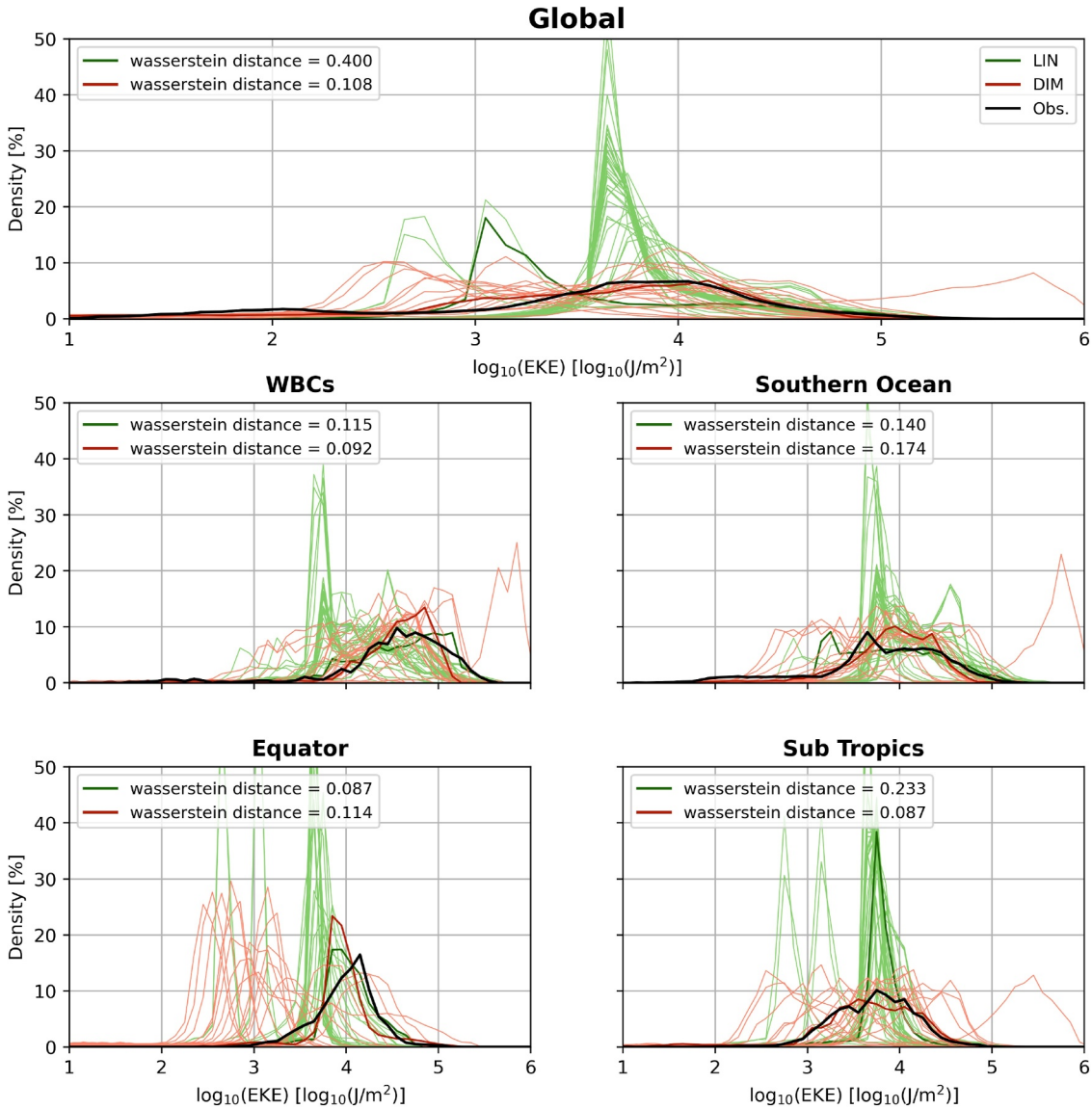

Figure E7. Probability density functions of the depth-integrated eddy kinetic energy in the global ocean and four dynamical regions: the western boundary currents, the Southern Ocean, the equatorial and the subtropical bands. The black line refers to the reference data set built from observations and displayed in Figure 2. The green and red thin lines show the simulations using the linear and dimension-based formulations, respectively. For each domain, the best distribution according to the Wasserstein distance metric is plotted in thick and its score is given in the legend. Note that the best distribution in one region does not necessary correspond to the best in other regions.

and energetics within the proposed parameterization. This suggests that the eddy efficiency and the dissipation coefficient cannot be tuned independently. However, there is currently no consensus on the optimal values for these parameters, as they are not well constrained by observations or theory (see Table E1). It is also important to remember that κ_{gm} is proportional to α, meaning that the dissipation coefficient will drive the eddy advective transport of GM for a fixed, targeted domain-integrated EKE. In this work, we have used $\alpha = 0.04$ since it has been demonstrated to provide optimal results in terms of EKE in relation to our specified criteria. However, we acknowledge that this parameter could be increased or decreased (while reducing or increasing the dissipation coefficient) while maintaining correct EKE levels. Given that κ_{gm} can significantly influence the ocean circulation, it is essential to constrain the parameter α (or the dissipation) in our parameterization, although this is beyond the scope of the present study.

Finally, our results demonstrate that both the linear dissipation formulation and the one based on dimensional analysis can achieve the targeted domain-integrated EKE. In order to achieve an accurate distribution of the EKE, it is necessary to determine which formulation to choose for the dissipation.

E3. Choosing the Dissipation Formulation

One of the key considerations is determining whether the linear damping or the formulation based on dimensional analysis is more suitable for modeling the EKE sinks in our global NEMO ocean model. Figure E6 presents a summary of the performance of the 80 simulations regarding the depth-integrated EKE field, as represented by box plots and Taylor diagrams (Taylor, 2001). When considering the global ocean, the diagrams demonstrate a net improvement in the parameterized depth-integrated EKE when using the dimension-based formulation. Indeed, the correlation coefficients range from 0.58 to 0.68 against 0.35 to 0.55 when using the linear formulation. Further analysis of the data across different domains corroborates this finding, indicating that the dimension-based dissipation (and its 3/2 power law) is an accurate representation of the EKE sinks in coarse-resolution ocean models. To gain further insight into the performance of the parameterization in representing the EKE distribution, spatial probability density functions of the depth-integrated EKE are analyzed in a logarithmic scale (Figure E7). At the global scale, the dissipation based on dimensional arguments allows a suitable energy distribution across the ocean, with the mean value adjustable by the coefficient C_e and/or the eddy efficiency α. In contrast, using a linear damping to model the dissipation generally concentrates the energy around its mean and lacks the ability to redistribute it into a log-normal distribution. This is particularly the case in subtropical regions, where only simulations using a dimensional analysis-based dissipation model can produce the desired distribution, in line with altimetric observations.

Conflict of Interest

The authors declare no conflicts of interest relevant to this study.

Data Availability Statement

This work uses modified FORTRAN routines to adapt the NEMO software version 3.6 and constrain the mesoscale coefficients with a prognostic eddy kinetic energy equation (Torres et al., 2025). Model output and processed data as well as Python scripts used to produce the results are available in Torres (2025).

Acknowledgments
We would like to thank the four anonymous reviewers, two of whom reviewed the study twice, for their numerous comments and suggestions. These have led to an improved presentation and discussion of our results. Their time and remarks are greatly appreciated. We also thank Aurore Voldoire for the constructive discussions on the model and the calibration method. This project has received support from the European Union's Horizon 2020 research and innovation programme under Grant Agreement N° 101003536 (ESM2025-Earth System Models for the Future). This study has also received funding from Agence Nationale de la Recherche - France 2030 as part of the PEPR TRACCS programme under Grant ANR-22-EXTR-0008. CdL acknowledges support from grant ANR-22-EXTR-0008. JM acknowledges support from HK RGC GRF Grant 16303625. We particularly acknowledge the support of the team in charge of the CNRM-CM climate model. Supercomputing time was provided by the Météo-France/DSI supercomputing center.

References

Abernathey, R., Gnanadesikan, A., Pradal, M.-A., & Sundermeyer, M. A. (2022). Isopycnal mixing. In *Ocean mixing* (pp. 215–256). Elsevier. https://doi.org/10.1016/b978-0-12-821512-8.00016-5

Adcroft, A., Anderson, W., Balaji, V., Blanton, C., Bushuk, M., Dufour, C. O., et al. (2019). The GFDL Global Ocean and Sea Ice Model OM4.0: Model description and simulation features. *Journal of Advances in Modeling Earth Systems*, *11*(10), 3167–3211. https://doi.org/10.1029/2019ms001726

Bachman, S. D. (2019). The GM+E closure: A framework for coupling backscatter with the Gent and McWilliams parameterization. *Ocean Modelling*, *136*, 85–106. https://doi.org/10.1016/j.ocemod.2019.02.006

Bachman, S. D., Marshall, D. P., Maddison, J. R., & Mak, J. (2017). Evaluation of a scalar eddy transport coefficient based on geometric constraints. *Ocean Modelling*, *109*, 44–54. https://doi.org/10.1016/j.ocemod.2016.12.004

Barkan, R., Winters, K. B., & Smith, S. G. L. (2015). Energy cascades and loss of balance in a reentrant channel forced by wind stress and buoyancy fluxes. *Journal of Physical Oceanography*, *45*(1), 272–293. https://doi.org/10.1175/JPO-D-14-0068.1

Beech, N., Rackow, T., Semmler, T., Danilov, S., Wang, Q., & Jung, T. (2022). Long-term evolution of ocean eddy activity in a warming world. *Nature Climate Change*, *12*(10), 910–917. https://doi.org/10.1038/s41558-022-01478-3

Borowski, D., Gerdes, R., & Olbers, D. (2002). Thermohaline and wind forcing of a circumpolar channel withblocked geostrophic contours. *Journal of Physical Oceanography*, *32*(9), 2520–2540. https://doi.org/10.1175/1520-0485(2002)032⟨2520:tawfoa⟩2.0.co;2

Bryan, K., Dukowicz, J. K., & Smith, R. D. (1999). On the mixing coefficient in the parameterization of bolus velocity. *Journal of Physical Oceanography*, *29*(9), 2442–2456. https://doi.org/10.1175/1520-0485(1999)029⟨2442:otmcit⟩2.0.co;2

Buckley, M. W., & Marshall, J. (2016). Observations, inferences, and mechanisms of the Atlantic Meridional Overturning Circulation: A review. *Reviews of Geophysics*, *54*(1), 5–63. https://doi.org/10.1002/2015rg000493

Busecke, J. J. M., & Abernathey, R. P. (2019). Ocean mesoscale mixing linked to climate variability. *Science Advances*, *5*(1), eaav5014. https://doi.org/10.1126/sciadv.aav5014

Cessi, P. (2008). An energy-constrained parameterization of eddy buoyancy flux. *Journal of Physical Oceanography*, *38*(8), 1807–1819. https://doi.org/10.1175/2007JPO3812.1

Chassignet, E. P., Smith, L. T., Halliwell, G. R., & Bleck, R. (2003). North Atlantic simulations with the Hybrid Coordinate Ocean Model (HYCOM): Impact of the vertical coordinate choice, reference pressure, and thermobaricity. *Journal of Physical Oceanography*, *33*(12), 2504–2526. https://doi.org/10.1175/1520-0485(2003)033⟨2504:naswth⟩2.0.co;2

Chelton, D. B., Schlax, M. G., & Samelson, R. M. (2011). Global observations of nonlinear mesoscale eddies. *Progress in Oceanography*, *91*(2), 167–216. https://doi.org/10.1016/j.pocean.2011.01.002

Chen, R., Flierl, G. R., & Wunsch, C. (2014). A description of local and nonlocal eddy–mean flow interaction in a global eddy-permitting state estimate. *Journal of Physical Oceanography*, *44*(9), 2336–2352. https://doi.org/10.1175/jpo-d-14-0009.1

Cherchi, A., Fogli, P. G., Lovato, T., Peano, D., Iovino, D., Gualdi, S., et al. (2019). Global mean climate and main patterns of variability in the CMCC-CM2 coupled model. *Journal of Advances in Modeling Earth Systems*, *11*(1), 185–209. https://doi.org/10.1029/2018ms001369

Chouksey, A., Griesel, A., Chouksey, M., & Eden, C. (2022). Changes in global ocean circulation due to isopycnal diffusion. *Journal of Physical Oceanography*, *52*(9), 2219–2235. https://doi.org/10.1175/jpo-d-21-0205.1

Danabasoglu, G., Bates, S. C., Briegleb, B. P., Jayne, S. R., Jochum, M., Large, W. G., et al. (2012). The CCSM4 ocean component. *Journal of Climate*, *25*(5), 1361–1389. https://doi.org/10.1175/jcli-d-11-00091.1

Danabasoglu, G., & Marshall, J. (2007). Effects of vertical variations of thickness diffusivity in an ocean general circulation model. *Ocean Modelling*, *18*(2), 122–141. https://doi.org/10.1016/j.ocemod.2007.03.006

Danabasoglu, G., Yeager, S. G., Bailey, D., Behrens, E., Bentsen, M., Bi, D., et al. (2014). North Atlantic simulations in Coordinated Ocean-ice Reference Experiments phase II (CORE-II). Part I: Mean states. *Ocean Modelling*, *73*, 76–107. https://doi.org/10.1016/j.ocemod.2013.10.005

de La Lama, M. S., LaCasce, J. H., & Fuhr, H. K. (2016). The vertical structure of ocean eddies. *Dynamics and Statistics of the Climate System*, dzw001. https://doi.org/10.1093/climsys/dzw001

Deshayes, J., & Frankignoul, C. (2008). Simulated variability of the circulation in the North Atlantic from 1953 to 2003. *Journal of Climate*, *21*(19), 4919–4933. https://doi.org/10.1175/2008jcli1882.1

Donohue, K. A., Tracey, K. L., Watts, D. R., Chidichimo, M. P., & Chereskin, T. K. (2016). Mean Antarctic Circumpolar Current transport measured in Drake Passage. *Geophysical Research Letters*, *43*(22). https://doi.org/10.1002/2016gl070319

Ducet, N., Le Traon, P. Y., & Reverdin, G. (2000). Global high-resolution mapping of ocean circulation from TOPEX/Poseidon and ERS-1 and -2. *Journal of Geophysical Research*, *105*(C8), 19477–19498. https://doi.org/10.1029/2000jc900063

Eady, E. T. (1949). Long waves and cyclone waves. *Tellus*, *1*(3), 33–52. https://doi.org/10.3402/tellusa.v1i3.8507

Eden, C., & Greatbatch, R. J. (2008). Towards a mesoscale eddy closure. *Ocean Modelling*, *20*(3), 223–239. https://doi.org/10.1016/j.ocemod.2007.09.002

Evans, D. G., Frajka-Williams, E., & Naveira Garabato, A. C. (2022). Dissipation of mesoscale eddies at a western boundary via a direct energy cascade. *Scientific Reports*, *12*(1), 887. https://doi.org/10.1038/s41598-022-05002-7

Eyring, V., Bony, S., Meehl, G. A., Senior, C. A., Stevens, B., Stouffer, R. J., & Taylor, K. E. (2016). Overview of the Coupled Model Intercomparison Project Phase 6 (CMIP6) experimental design and organization. *Geoscientific Model Development*, *9*(5), 1937–1958. https://doi.org/10.5194/gmd-9-1937-2016

Farneti, R., Delworth, T. L., Rosati, A. J., Griffies, S. M., & Zeng, F. (2010). The role of mesoscale eddies in the rectification of the Southern Ocean response to climate change. *Journal of Physical Oceanography*, *40*(7), 1539–1557. https://doi.org/10.1175/2010jpo4353.1

Ferrari, R., & Nikurashin, M. (2010). Suppression of eddy diffusivity across jets in the Southern Ocean. *Journal of Physical Oceanography*, *40*(7), 1501–1519. https://doi.org/10.1175/2010jpo4278.1

Ferrari, R., & Wunsch, C. (2009). Ocean circulation kinetic energy: Reservoirs, sources, and sinks. *Annual Review of Fluid Mechanics*, *41*(1), 253–282. https://doi.org/10.1146/annurev.fluid.40.111406.102139

Ferreira, D., Marshall, J., & Heimbach, P. (2005). Estimating eddy stresses by fitting dynamics to observations using a residual-mean ocean circulation model and its adjoint. *Journal of Physical Oceanography*, *35*(10), 1891–1910. https://doi.org/10.1175/jpo2785.1

Fjørtoft, R. (1953). On the changes in the spectral distribution of kinetic energy for two dimensional, nondivergent flow. *Tellus*, *5*(3), 225–230. https://doi.org/10.1111/j.2153-3490.1953.tb01051.x

Fox-Kemper, B., Adcroft, A., Böning, C. W., Chassignet, E. P., Curchitser, E., Danabasoglu, G., et al. (2019). Challenges and prospects in ocean circulation models. *Frontiers in Marine Science*, *6*, 65. https://doi.org/10.3389/fmars.2019.00065

Fu, L. (2009). Pattern and velocity of propagation of the global ocean eddy variability. *Journal of Geophysical Research*, *114*(C11), C11017. https://doi.org/10.1029/2009jc005349

Garcia, H. E., Boyer, T. P., Baranova, O. K., Locarnini, R. A., Mishonov, A. V., Grodsky, A., et al. (2019). *World Ocean Atlas 2018: Product documentation*. NOAA National Centers for Environmental Information. Retrieved from https://www.ncei.noaa.gov/archive/accession/NCEI-WOA18

Gent, P. R., & McWilliams, J. C. (1990). Isopycnal mixing in ocean circulation models. *Journal of Physical Oceanography*, *20*(1), 150–155. https://doi.org/10.1175/1520-0485(1990)020⟨0150:imiocm⟩2.0.co;2

Gent, P. R., Willebrand, J., McDougall, T. J., & McWilliams, J. C. (1995). Parameterizing eddy-induced tracer transports in ocean circulation models. *Journal of Physical Oceanography*, *25*(4), 463–474. https://doi.org/10.1175/1520-0485(1995)025⟨0463:peitti⟩2.0.co;2

Gnanadesikan, A., Pradal, M.-A., & Abernathey, R. (2015). Isopycnal mixing by mesoscale eddies significantly impacts oceanic anthropogenic carbon uptake. *Geophysical Research Letters*, *42*(11), 4249–4255. https://doi.org/10.1002/2015gl064100

Griffies, S. M. (1998). The Gent–McWilliams skew flux. *Journal of Physical Oceanography*, *28*(5), 831–841. https://doi.org/10.1175/1520-0485(1998)028⟨0831:tgmsf⟩2.0.co;2

Groeskamp, S., LaCasce, J. H., McDougall, T. J., & Rogé, M. (2020). Full-depth global estimates of ocean mesoscale eddy mixing from observations and theory. *Geophysical Research Letters*, *47*(18), e2020GL089425. https://doi.org/10.1029/2020gl089425

Grooms, I. (2017). Simulations of eddy kinetic energy transport in barotropic turbulence. *Physical Review Fluids*, *2*(11), 113801. https://doi.org/10.1103/physrevfluids.2.113801

Grooms, I., Agarwal, N., Marques, G., Pegion, P. J., & Yassin, H. (2025). The stochastic GM + E closure: A framework for coupling stochastic backscatter with the Gent and McWilliams parameterization. *Journal of Advances in Modeling Earth Systems*, *17*(5), e2024MS004560. https://doi.org/10.1029/2024ms004560

Guilyardi, E., Madec, G., & Terray, L. (2001). The role of lateral ocean physics in the upper ocean thermal balance of a coupled ocean-atmosphere GCM. *Climate Dynamics*, *17*(8), 589–599. https://doi.org/10.1007/pl00007930

Hallberg, R. (2013). Using a resolution function to regulate parameterizations of oceanic mesoscale eddy effects. *Ocean Modelling*, *72*, 92–103. https://doi.org/10.1016/j.ocemod.2013.08.007

Held, I. M., Guo, H., Adcroft, A., Dunne, J. P., Horowitz, L. W., Krasting, J., et al. (2019). Structure and performance of GFDL's CM4.0 climate model. *Journal of Advances in Modeling Earth Systems*, *11*(11), 3691–3727. https://doi.org/10.1029/2019ms001829

Hewitt, H. T., Roberts, M., Mathiot, P., Biastoch, A., Blockley, E., Chassignet, E. P., et al. (2020). Resolving and parameterising the ocean mesoscale in Earth System Models. *Current Climate Change Reports*, *6*(4), 137–152. https://doi.org/10.1007/s40641-020-00164-w

Hieronymus, M., & Nycander, J. (2013). The budgets of heat and salinity in NEMO. *Ocean Modelling*, *67*, 28–38. https://doi.org/10.1016/j.ocemod.2013.03.006

Holmes, R. M., Groeskamp, S., Stewart, K. D., & McDougall, T. J. (2022). Sensitivity of a coarse-resolution global ocean model to a spatially variable neutral diffusivity. *Journal of Advances in Modeling Earth Systems*, *14*(3), e2021MS002914. https://doi.org/10.1029/2021ms002914

Hourdin, F., Ferster, B., Deshayes, J., Mignot, J., Musat, I., & Williamson, D. (2023). Toward machine-assisted tuning avoiding the underestimation of uncertainty in climate change projections. *Science Advances*, *9*(29), eadf2758. https://doi.org/10.1126/sciadv.adf2758

Hughes, C. W., Jones, M. S., & Carnochan, S. (1998). Use of transient features to identify eastward currents in the Southern Ocean. *Journal of Geophysical Research*, *103*(C2), 2929–2943. https://doi.org/10.1029/97jc02442

Iudicone, D., Madec, G., & McDougall, T. J. (2008). Water-Mass Transformations in a neutral density framework and the key role of light penetration. *Journal of Physical Oceanography*, *38*(7), 1357–1376. https://doi.org/10.1175/2007jpo3464.1

Jansen, M. F., Adcroft, A., Khani, S., & Kong, H. (2019). Toward an energetically consistent, resolution aware parameterization of ocean mesoscale eddies. *Journal of Advances in Modeling Earth Systems*, *11*(8), 2844–2860. https://doi.org/10.1029/2019MS001750

Jansen, M. F., Adcroft, A. J., Hallberg, R., & Held, I. M. (2015). Parameterization of eddy fluxes based on a mesoscale energy budget. *Ocean Modelling*, *92*, 28–41. https://doi.org/10.1016/j.ocemod.2015.05.007

Jansen, M. F., & Held, I. M. (2014). Parameterizing subgrid-scale eddy effects using energetically consistent backscatter. *Ocean Modelling*, *80*, 36–48. https://doi.org/10.1016/j.ocemod.2014.06.002

Jansen, M. F., Held, I. M., Adcroft, A., & Hallberg, R. (2015). Energy budget-based backscatter in an eddy permitting primitive equation model. *Ocean Modelling*, *94*, 15–26. https://doi.org/10.1016/j.ocemod.2015.07.015

Juricke, S., Danilov, S., Koldunov, N., Oliver, M., & Sidorenko, D. (2020). Ocean kinetic energy backscatter parametrization on unstructured grids: Impact on global eddy-permitting simulations. *Journal of Advances in Modeling Earth Systems*, *12*(1), e2019MS001855. https://doi.org/10.1029/2019MS001855

Kang, D., & Curchitser, E. N. (2015). Energetics of eddy–mean flow interactions in the Gulf Stream region. *Journal of Physical Oceanography*, *45*(4), 1103–1120. https://doi.org/10.1175/jpo-d-14-0200.1

Klocker, A., Ferrari, R., & LaCasce, J. H. (2012). Estimating suppression of eddy mixing by mean flows. *Journal of Physical Oceanography*, *42*(9), 1566–1576. https://doi.org/10.1175/jpo-d-11-0205.1

Klocker, A., & Marshall, D. P. (2014). Advection of baroclinic eddies by depth mean flow. *Geophysical Research Letters*, *41*(10), 3517–3521. https://doi.org/10.1002/2014gl060001

Klocker, A., & McDougall, T. J. (2010). Influence of the nonlinear equation of state on global estimates of dianeutral advection and diffusion. *Journal of Physical Oceanography*, *40*(8), 1690–1709. https://doi.org/10.1175/2010jpo4303.1

Klymak, J. M. (2018). Nonpropagating form drag and turbulence due to stratified flow over large-scale abyssal hill topography. *Journal of Physical Oceanography*, *48*(10), 2383–2395. https://doi.org/10.1175/jpo-d-17-0225.1

Kolmogorov, A. N. (1941a). Dissipation of energy in the locally isotropic turbulence. *Doklady Akademii Nauk SSSR*, *32*, 16.

Kolmogorov, A. N. (1941b). The local structure of turbulence in incompressible viscous fluid for very large Reynolds numbers. *Doklady Akademii Nauk SSSR*, *30*, 301–305.

Kuhlbrodt, T., Smith, R., Wang, Z., & Gregory, J. (2012). The influence of eddy parameterizations on the transport of the Antarctic Circumpolar Current in coupled climate models. *Ocean Modelling*, *52–53*, 1–8. https://doi.org/10.1016/j.ocemod.2012.04.006

Kusters, N., Balwada, D., & Groeskamp, S. (2025). Global observational estimates of mesoscale eddy-driven quasi-stokes velocity and buoyancy diffusivity. *Geophysical Research Letters*, *52*(12), e2025GL115802. https://doi.org/10.1029/2025gl115802

LaCasce, J. H. (2017). The prevalence of oceanic surface modes. *Geophysical Research Letters*, *44*(21), 11097. https://doi.org/10.1002/2017gl075430

Lévy, M., Couespel, D., Haëck, C., Keerthi, M., Mangolte, I., & Prend, C. J. (2024). The impact of fine-scale currents on biogeochemical cycles in a changing ocean. *Annual Review of Marine Science*, *16*(1), 191–215. https://doi.org/10.1146/annurev-marine-020723-020531

Li, L., Ingersoll, A. P., Jiang, X., Feldman, D., & Yung, Y. L. (2007). Lorenz energy cycle of the global atmosphere based on reanalysis datasets. *Geophysical Research Letters*, *34*(16), L16813. https://doi.org/10.1029/2007gl029985

Li, Q., Sun, L., & Xu, C. (2018). The lateral eddy viscosity derived from the decay of oceanic mesoscale eddies. *Open Journal of Marine Science*, *8*(1), 152–172. https://doi.org/10.4236/ojms.2018.81008

Lin, P., Yu, Z., Liu, H., Yu, Y., Li, Y., Jiang, J., et al. (2020). LICOM model datasets for the CMIP6 Ocean Model Intercomparison Project. *Advances in Atmospheric Sciences*, *37*(3), 239–249. https://doi.org/10.1007/s00376-019-9208-5

Lorenz, E. N. (1955). Available potential energy and the maintenance of the general circulation. *Tellus*, *7*(2), 157–167. https://doi.org/10.1111/j.2153-3490.1955.tb01148.x

Lozier, M. S. (2012). Overturning in the north Atlantic. *Annual Review of Marine Science*, *4*(1), 291–315. https://doi.org/10.1146/annurev-marine-120710-100740

Lozier, M. S., Li, F., Bacon, S., Bahr, F., Bower, A. S., Cunningham, S. A., et al. (2019). A sea change in our view of overturning in the subpolar North Atlantic. *Science*, *363*(6426), 516–521. https://doi.org/10.1126/science.aau6592

Ma, Q., Lembo, V., & Franzke, C. L. (2021). The Lorenz energy cycle: Trends and the impact of modes of climate variability. *Tellus A: Dynamic Meteorology and Oceanography*, *73*(1), 1900033. https://doi.org/10.1080/16000870.2021.1900033

Macdonald, A. M., & Baringer, M. O. (2013). Ocean heat transport. In *Ocean circulation and climate - A 21st century perspective* (pp. 759–785). Elsevier. https://doi.org/10.1016/b978-0-12-391851-2.00029-5

Maddison, J. R., Marshall, D. P., Mak, J., & Maurer-Song, K. (2025). A two-dimensional model for eddy saturation and frictional control in the Southern Ocean. *Journal of Advances in Modeling Earth Systems*, *17*(4), e2024MS004682. https://doi.org/10.1029/2024ms004682

Madec, G., Bourdallé-Badie, R., Pierre-Antoine, B., Bricaud, C., Bruciaferri, D., Calvert, D., et al. (2017). NEMO ocean engine. *Zenodo*. https://doi.org/10.5281/ZENODO.1472492

Mak, J., Avdis, A., David, T., Lee, H. S., Na, Y., Wang, Y., & Yan, F. E. (2022). On constraining the mesoscale eddy energy dissipation timescale. *Journal of Advances in Modeling Earth Systems*, *14*(11), e2022MS003223. https://doi.org/10.1029/2022MS003223

Mak, J., Maddison, J. R., Marshall, D. P., & Munday, D. R. (2018). Implementation of a geometrically informed and energetically constrained mesoscale eddy parameterization in an ocean circulation model. *Journal of Physical Oceanography*, *48*(10), 2363–2382. https://doi.org/10.1175/jpo-d-18-0017.1

Mak, J., Marshall, D., Maddison, J., & Bachman, S. (2017). Emergent eddy saturation from an energy constrained eddy parameterisation. *Ocean Modelling*, *112*, 125–138. https://doi.org/10.1016/j.ocemod.2017.02.007

Mak, J., Marshall, D. P., Madec, G., & Maddison, J. R. (2022). Acute sensitivity of global ocean circulation and heat content to eddy energy dissipation timescale. *Geophysical Research Letters*, *49*(8), e2021GL097259. https://doi.org/10.1029/2021GL097259

Maltrud, M. E., & Vallis, G. K. (1991). Energy spectra and coherent structures in forced two-dimensional and beta-plane turbulence. *Journal of Fluid Mechanics Digital Archive*, *228*, 321–342. https://doi.org/10.1017/s0022112091002720

Marchesiello, P., Capet, X., Menkes, C., & Kennan, S. C. (2011). Submesoscale dynamics in tropical instability waves. *Ocean Modelling*, *39*(1–2), 31–46. https://doi.org/10.1016/j.ocemod.2011.04.011

Marshall, D. P., & Adcroft, A. J. (2010). Parameterization of ocean eddies: Potential vorticity mixing, energetics and Arnold's first stability theorem. *Ocean Modelling*, *32*(3–4), 188–204. https://doi.org/10.1016/j.ocemod.2010.02.001

Marshall, D. P., Ambaum, M. H. P., Maddison, J. R., Munday, D. R., & Novak, L. (2017). Eddy saturation and frictional control of the Antarctic Circumpolar Current. *Geophysical Research Letters*, *44*(1), 286–292. https://doi.org/10.1002/2016gl071702

Marshall, D. P., Maddison, J. R., & Berloff, P. S. (2012). A framework for parameterizing eddy potential vorticity fluxes. *Journal of Physical Oceanography*, *42*(4), 539–557. https://doi.org/10.1175/jpo-d-11-048.1

Marshall, J., & Schott, F. (1999). Open-ocean convection: Observations, theory, and models. *Reviews of Geophysics*, *37*(1), 1–64. https://doi.org/10.1029/98rg02739

Martinez-Moreno, J., Hogg, A., England, M., Constantinou, N. C., Kiss, A. E., & Morrison, A. (2020). Global changes in oceanic mesoscale currents over the satellite altimetry record. *Nature Climate Change*. https://doi.org/10.21203/rs.3.rs-88932/v1

Melet, A. V., Hallberg, R., & Marshall, D. P. (2022). The role of ocean mixing in the climate system. In *Ocean mixing* (pp. 5–34). Elsevier. https://doi.org/10.1016/b978-0-12-821512-8.00009-8

Menary, M. B., Jackson, L. C., & Lozier, M. S. (2020). Reconciling the relationship between the AMOC and Labrador Sea in OSNAP observations and climate models. *Geophysical Research Letters*, *47*(18), e2020GL089793. https://doi.org/10.1029/2020gl089793

Meunier, J., Miquel, B., & Gallet, B. (2023). Vertical structure of buoyancy transport by ocean baroclinic turbulence. *Geophysical Research Letters*, *50*(17), e2023GL103948. https://doi.org/10.1029/2023gl103948

Moat, B. I., Smeed, D., Rayner, D., Johns, W. E., Smith, R. H., Volkov, D. L., et al. (2023). Atlantic meridional overturning circulation observed by the RAPID-MOCHA-WBTS (RAPID-Meridional Overturning Circulation and Heatflux Array-Western Boundary Time Series) array at 26N from 2004 to 2022 (v2022.1). https://doi.org/10.5285/04C79ECE-3186-349A-E063-6C86ABC0158C

Molemaker, M. J., McWilliams, J. C., & Capet, X. (2010). Balanced and unbalanced routes to dissipation in an equilibrated Eady flow. *Journal of Fluid Mechanics*, *654*, 35–63. https://doi.org/10.1017/S0022112009993272

Naveira Garabato, A. C., Ferrari, R., & Polzin, K. L. (2011). Eddy stirring in the Southern Ocean. *Journal of Geophysical Research*, *116*(C9), C09019. https://doi.org/10.1029/2010jc006818

Olbers, D., Borowski, D., Völker, C., & Wölff, J.-O. (2004). The dynamical balance, transport and circulation of the Antarctic Circumpolar Current. *Antarctic Science*, *16*(4), 439–470. https://doi.org/10.1017/s0954102004002251

Panaretos, V. M., & Zemel, Y. (2019). Statistical aspects of Wasserstein distances. *Annual Review of Statistics and Its Application*, *6*(1), 405–431. https://doi.org/10.1146/annurev-statistics-030718-104938

Pearson, B., & Fox-Kemper, B. (2018). Log-normal turbulence dissipation in global ocean models. *Physical Review Letters*, *120*(9), 094501. https://doi.org/10.1103/physrevlett.120.094501

Polzin, K. L. (2010). Mesoscale eddy–internal wave coupling. part II: Energetics and results from PolyMode. *Journal of Physical Oceanography*, *40*(4), 789–801. https://doi.org/10.1175/2009jpo4039.1

Poulsen, M. B., Jochum, M., Maddison, J. R., Marshall, D. P., & Nuterman, R. (2019). A geometric interpretation of Southern Ocean eddy form stress. *Journal of Physical Oceanography*, *49*(10), 2553–2570. https://doi.org/10.1175/JPO-D-18-0220.1

Pradal, M.-A., & Gnanadesikan, A. (2014). How does the Redi parameter for mesoscale mixing impact global climate in an Earth System Model? *Journal of Advances in Modeling Earth Systems*, *6*(3), 586–601. https://doi.org/10.1002/2013MS000273

Prandtl, L. (1925). Report on investigation of developed turbulence. *National Advisory Committee for Aeronautics*, *5*, 136–139. Retrieved from https://ntrs.nasa.gov/citations/20050029454

Rai, S., Hecht, M., Maltrud, M., & Aluie, H. (2021). Scale of oceanic eddy killing by wind from global satellite observations. *Science Advances*, *7*(28), eabf4920. https://doi.org/10.1126/sciadv.abf4920

Ramdas, A., Garcia, N., & Cuturi, M. (2015). On Wasserstein two sample testing and related families of nonparametric tests. https://doi.org/10.48550/ARXIV.1509.02237

Redi, M. H. (1982). Oceanic isopycnal mixing by coordinate rotation. *Journal of Physical Oceanography*, *12*(10), 1154–1158. https://doi.org/10.1175/1520-0485(1982)012⟨1154:oimbcr⟩2.0.co;2

Reynolds, O. (1895). On the dynamical theory of incompressible viscous fluids and the determination of the criterion. *Philosophical Transactions of the Royal Society of London. (A.)*, *186*, 123–164. https://doi.org/10.1098/rsta.1895.0004

Roquet, F., Madec, G., McDougall, T. J., & Barker, P. M. (2015). Accurate polynomial expressions for the density and specific volume of seawater using the TEOS-10 standard. *Ocean Modelling*, *90*, 29–43. https://doi.org/10.1016/j.ocemod.2015.04.002

Ruan, X., Couespel, D., Lévy, M., Li, J., Mak, J., & Wang, Y. (2023). Combined physical and biogeochemical assessment of mesoscale eddy parameterisations in ocean models: Eddy induced advection at non-eddying resolutions. *Ocean Modelling*, *183*, 102204. https://doi.org/10.1016/j.ocemod.2023.102204

Salas Mélia, D. (2002). A global coupled sea ice–ocean model. *Ocean Modelling*, *4*(2), 137–172. https://doi.org/10.1016/s1463-5003(01)00015-4

Seland, Ø., Bentsen, M., Olivié, D., Toniazzo, T., Gjermundsen, A., Graff, L. S., et al. (2020). Overview of the Norwegian Earth System Model (NorESM2) and key climate response of CMIP6 DECK, historical, and scenario simulations. *Geoscientific Model Development*, *13*(12), 6165–6200. https://doi.org/10.5194/gmd-13-6165-2020

Sen, A., Scott, R. B., & Arbic, B. K. (2008). Global energy dissipation rate of deep-ocean low-frequency flows by quadratic bottom boundary layer drag: Computations from current-meter data. *Geophysical Research Letters*, *35*(9). https://doi.org/10.1029/2008GL033407

Sérazin, G., Penduff, T., Barnier, B., Molines, J.-M., Arbic, B. K., Müller, M., & Terray, L. (2018). Inverse cascades of kinetic energy as a source of intrinsic variability: A global OGCM study. *Journal of Physical Oceanography*, *48*(6), 1385–1408. https://doi.org/10.1175/jpo-d-17-0136.1

Smith, K. S., & Marshall, J. (2009). Evidence for enhanced eddy mixing at middepth in the Southern Ocean. *Journal of Physical Oceanography*, *39*(1), 50–69. https://doi.org/10.1175/2008jpo3880.1

Stanley, Z., Bachman, S. D., & Grooms, I. (2020). Vertical structure of ocean mesoscale eddies with implications for parameterizations of tracer transport. *Journal of Advances in Modeling Earth Systems*, *12*(10), e2020MS002151. https://doi.org/10.1029/2020ms002151

Steinberg, J. M., Cole, S. T., Drushka, K., & Abernathey, R. P. (2022). Seasonality of the mesoscale inverse cascade as inferred from global scale-dependent eddy energy observations. *Journal of Physical Oceanography*, *52*(8), 1677–1691. https://doi.org/10.1175/jpo-d-21-0269.1

Tatebe, H., Ogura, T., Nitta, T., Komuro, Y., Ogochi, K., Takemura, T., et al. (2019). Description and basic evaluation of simulated mean state, internal variability, and climate sensitivity in MIROC6. *Geoscientific Model Development*, *12*(7), 2727–2765. https://doi.org/10.5194/gmd-12-2727-2019

Taylor, K. E. (2001). Summarizing multiple aspects of model performance in a single diagram. *Journal of Geophysical Research*, *106*(D7), 7183–7192. https://doi.org/10.1029/2000jd900719

Tedesco, P., Gula, J., Ménesguen, C., Penven, P., & Krug, M. (2019). Generation of submesoscale frontal eddies in the Agulhas Current. *Journal of Geophysical Research: Oceans*, *124*(11), 7606–7625. https://doi.org/10.1029/2019jc015229

Torres, R. (2025). Scripts and datas for "An energetically and observationally constrained mesoscale parameterisation for ocean climate models" [Dataset]. *Zenodo*. https://doi.org/10.5281/zenodo.17535298

Torres, R., Madec, G., & Mak, J. (2025). Patch for the LDF (lateral mixing) module of the NEMO version 3.6 [Software]. *Zenodo*. https://doi.org/10.5281/ZENODO.14843614

Torres, R., Waldman, R., Mak, J., & Séférian, R. (2023). Global estimation of the eddy kinetic energy dissipation from a diagnostic energy balance. *Geophysical Research Letters*, *50*(20), e2023GL104688. https://doi.org/10.1029/2023gl104688

Treguier, A. M., Held, I. M., & Larichev, V. D. (1997). Parameterization of quasigeostrophic eddies in primitive equation ocean models. *Journal of Physical Oceanography*, *27*(4), 567–580. https://doi.org/10.1175/1520-0485(1997)027<0567:poqeip>2.0.co;2

Tsujino, H., Urakawa, L. S., Griffies, S. M., Danabasoglu, G., Adcroft, A. J., Amaral, A. E., et al. (2020). Evaluation of global ocean–sea-ice model simulations based on the experimental protocols of the Ocean Model Intercomparison Project phase 2 (OMIP-2). *Geoscientific Model Development*, *13*(8), 3643–3708. https://doi.org/10.5194/gmd-13-3643-2020

Tsujino, H., Urakawa, S., Nakano, H., Small, R. J., Kim, W. M., Yeager, S. G., et al. (2018). JRA-55 based surface dataset for driving ocean–sea-ice models (JRA55-do). *Ocean Modelling*, *130*, 79–139. https://doi.org/10.1016/j.ocemod.2018.07.002

Vallis, G. K. (2017). *Atmospheric and oceanic fluid dynamics: Fundamentals and large-scale circulation*. Cambridge University Press. https://doi.org/10.1017/9781107588417

Visbeck, M., Marshall, J., Haine, T., & Spall, M. (1997). Specification of eddy transfer coefficients in coarse-resolution ocean circulation models. *Journal of Physical Oceanography*, *27*(3), 381–402. https://doi.org/10.1175/1520-0485(1997)027⟨0381:soetci⟩2.0.co;2

Vogt, L., de Lavergne, C., Sallée, J.-B., Kwiatkowski, L., Frölicher, T. L., & Terhaar, J. (2025). Increased future ocean heat uptake constrained by Antarctic sea ice extent. https://doi.org/10.21203/rs.3.rs-3982037/v2

Voldoire, A. (2020). CNRM-CERFACS CNRM-CM6-1 model output prepared for CMIP6 OMIP omip2. *Earth System Grid Federation*. https://doi.org/10.22033/ESGF/CMIP6.10345

Voldoire, A., Saint-Martin, D., Sénési, S., Decharme, B., Alias, A., Chevallier, M., et al. (2019). Evaluation of CMIP6 DECK experiments with CNRM-CM6-1. *Journal of Advances in Modeling Earth Systems*, *11*(7), 2177–2213. https://doi.org/10.1029/2019MS001683

Vollmer, L., & Eden, C. (2013). A global map of meso-scale eddy diffusivities based on linear stability analysis. *Ocean Modelling*, *72*, 198–209. https://doi.org/10.1016/j.ocemod.2013.09.006

von Storch, J.-S., Eden, C., Fast, I., Haak, H., Hernández-Deckers, D., Maier-Reimer, E., et al. (2012). An estimate of the Lorenz energy cycle for the world ocean based on the STORM/NCEP simulation. *Journal of Physical Oceanography*, *42*(12), 2185–2205. https://doi.org/10.1175/JPO-D-12-079.1

Waldman, R., Hirschi, J., Voldoire, A., Cassou, C., & Msadek, R. (2021). Clarifying the relation between amoc and thermal wind: Application to the centennial variability in a coupled climate model. *Journal of Physical Oceanography*, *51*(2), 343–364. https://doi.org/10.1175/jpo-d-19-0284.1

Wang, Q., Danilov, S., Sidorenko, D., Timmermann, R., Wekerle, C., Wang, X., et al. (2014). The Finite Element Sea Ice-Ocean Model (FESOM) v.1.4: Formulation of an ocean general circulation model. *Geoscientific Model Development*, *7*(2), 663–693. https://doi.org/10.5194/gmd-7-663-2014

Watanabe, M., Suzuki, T., O'ishi, R., Komuro, Y., Watanabe, S., Emori, S., et al. (2010). Improved climate simulation by MIROC5: Mean states, variability, and climate sensitivity. *Journal of Climate*, *23*(23), 6312–6335. https://doi.org/10.1175/2010JCLI3679.1

Wei, H., Wang, Y., Stewart, A. L., & Mak, J. (2022). Scalings for eddy buoyancy fluxes across prograde shelf/slope fronts. *Journal of Advances in Modeling Earth Systems*, *14*(12), e2022MS003229. https://doi.org/10.1029/2022ms003229

Williamson, D. B., Blaker, A. T., & Sinha, B. (2017). Tuning without over-tuning: Parametric uncertainty quantification for the nemo ocean model. *Geoscientific Model Development*, *10*(4), 1789–1816. https://doi.org/10.5194/gmd-10-1789-2017

Yang, H., Li, Q., Wang, K., Sun, Y., & Sun, D. (2014). Decomposing the meridional heat transport in the climate system. *Climate Dynamics*, *44*(9–10), 2751–2768. https://doi.org/10.1007/s00382-014-2380-5

Yeager, S., Castruccio, F., Chang, P., Danabasoglu, G., Maroon, E., Small, J., et al. (2021). An outsized role for the Labrador Sea in the multidecadal variability of the Atlantic overturning circulation. *Science Advances*, *7*(41), eabh3592. https://doi.org/10.1126/sciadv.abh3592

Zanna, L., Porta Mana, P., Anstey, J., David, T., & Bolton, T. (2017). Scale-aware deterministic and stochastic parametrizations of eddy-mean flow interaction. *Ocean Modelling*, *111*, 66–80. https://doi.org/10.1016/j.ocemod.2017.01.004

Zhang, R., Sutton, R., Danabasoglu, G., Kwon, Y., Marsh, R., Yeager, S. G., et al. (2019). A review of the role of the Atlantic Meridional Overturning Circulation in Atlantic multidecadal variability and associated climate impacts. *Reviews of Geophysics*, *57*(2), 316–375. https://doi.org/10.1029/2019rg000644

Zhang, W., & Wolfe, C. L. P. (2022). On the vertical structure of oceanic mesoscale tracer diffusivities. *Journal of Advances in Modeling Earth Systems*, *14*(6), e2021MS002891. https://doi.org/10.1029/2021ms002891

Zweng, M. M., Reagan, J. R., Antonov, J. I., Locarnini, R. A., Mishonov, A. V., Boyer, T. P., et al. (2013). *World Ocean Atlas 2013, volume 2: Salinity* (Vol. 74, p. 39). NOAA Atlas NESDIS.